Application and Study of Water Oxidation Catalysts and Molecular Dyes for Solar-Fuel Production

by

Benjamin D. Sherman

A Dissertation Presented in Partial Fulfillment
of the Requirements for the Degree
Doctor of Philosophy

Approved July 2013 by the
Graduate Supervisory Committee:

Thomas Moore, Chair.
Ana L. Moore
Daniel Buttry

ARIZONA STATE UNIVERSITY

August 2013

ABSTRACT

Developing a system capable of using solar energy to drive the conversion of an abundant and available precursor to fuel would profoundly impact humanity's energy use and thereby the condition of the global ecosystem. Such is the goal of artificial photosynthesis: to convert water to hydrogen using solar radiation as the sole energy input and ideally do so with the use of low cost, abundant materials. Constructing photoelectrochemical cells incorporating photoanodes structurally reminiscent of those used in dye sensitized photovoltaic solar cells presents one approach to establishing an artificial photosynthetic system. The work presented herein describes the production, integration, and study of water oxidation catalysts, molecular dyes, and metal oxide based photoelectrodes carried out in the pursuit of developing solar water splitting systems.

For my family

ACKNOWLEDGMENTS

I owe gratitude to many for their help, collaboration, teachings, and assistance over the course of my study. Thank you to Science Foundation Arizona for their support through a graduate research fellowship during my first two years of study. I especially owe thanks to those I have had the good fortune to work in collaboration with: Erika Wee and Tito Scaiano at the University of Ottawa, Yixin Zhao and Tom Mallouk at The Pennsylvania State University, Robert Godin and Gonzalo Cosa at McGill University, Rodrigo Palacios at La Universidad Nacional de Rio Cuarto, and Ernesto Marino-Ochoa at Technologico de Monterrey. Thank you all for your patience, your help and assistance, and the opportunity to learn and study through our collaborative work. I would like to thank the many graduate students, undergraduates, postdocs, and visiting faculty I had the opportunity and pleasure to work with over the last five years in the Gust, Moore, Moore group. Special thanks to Smitha Pillai and Chelsea Brown for their synthetic prowess and kind demeanor; to Matthieu Koepf and Graeme Copley for their advice and friendship; to Gerdenis Kodis for his expertise with spectroscopy; to Paul Liddell for keeping the lab running smoothly and his excellent freelance machine work; and to Chris Madden, Jeff Crisman, Dustin Patterson, and Jim Bridgewater for the help along the way, your friendship, and keeping life entertaining. I thank Michael Hambourger for showing me the ropes and preparing me so I could contribute. I'm lucky to have started my graduate study alongside Jesse Bergkamp and Michael Vaughn. One could not ask for better friends and colleagues. Finally, I thank my bosses, Devens Gust, Ana Moore, and Tom Moore, for the opportunity to study, learn, and pursue my interests, and also for your support, enthusiasm, and guidance during my PhD work.

TABLE OF CONTENTS

Page

LIST OF TABLES viii

LIST OF FIGURES ix

LIST OF SCHEMES xii

CHAPTER

1 EVOLUTION OF REACTION CENTER MIMICS TO SYSTEMS CAPABLE OF GENERATING SOLAR FUEL 1

Introduction 1

Molecular Reaction Centers 8

Triad Reaction Centers 8

Antenna–Reaction Centers 13

Photoregulation 17

Charge Separation Across a Membrane 18

Mimicing Proton Control During Electron Transfer 20

Employing Reaction Centers for Water Splitting 22

Conclusion 23

2 A PORPHYRIN-STABILIZED IRIDIUM OXIDE WATER OXIDATION CATALYST 25

Introduction 25

Experimental 27

Materials 27

Porphyrin Synthesis 28

CHAPTER Page

Porphyrin 1....28

Porphyrin 1a....29

Porphyrin 2....29

Porphyrin 2a....30

Preparation of the Porphyrin–$IrO_x \cdot nH_2O$ Complex....30

Electrochemical Measurements....30

Clark Electrode Measurements....31

Time-resolved Fluorescence Measurements....31

Results and Discussion....32

Conclusion....38

3 PHOTOCHEMICAL SYNTHESIS OF A WATER OXIDATION CATALYST BASED ON COBALT NANOSTRUCTURES....40

Introduction....40

Results and Discussion....41

Conclusion....48

Experimental Detail and Supplementary Information....48

Oxygen Measurements....48

Spontaneous Air Oxidation to Form Cobalt Oxide Nanoparticles....49

Preliminary Estimation of Turnover Frequency for Co_2O_3NP....54

4 SYNTHESIS AND CHARACTERIZATION OF SILICON PHTHALOCYANINES BEARING AXIAL PHENOXYL GROUPS FOR ATTACHMENT TO SEMICONDUCTING METAL OXIDES....58

CHAPTER Page

Introduction....58

Results and Discussion....60

Conclusion....67

Experimental....68

Electrochemistry....68

Materials....69

General....70

Synthesis....70

5 DEVELOPMENT AND STUDY OF TANDEM PHOTOELECTROCHEMICAL SOLAR CELLS....75

Introduction....75

Results and Discussion....77

Dye Structures....77

Spectral Considerations....79

Semiconductor Considerations....81

Photoanode for Water Oxidation....83

Red Absorbing Junction....88

Tandem Cell with Use of a Sacrificial Donor....91

Tandem Cell for Water Splitting....94

Conclusion....98

REFERENCES....99

APPENDIX Page

I DETAILS OF COPYRIGHT PERMISSION FOR REPRODUCTION 111

LIST OF TABLES

Table Page

1. Final Charge Separated State Lifetimes, Quantum Yields for the Formation of the Final Charge Separated State, and Experimental Conditions for Selected Artificial Reaction Centers 10

2. Electrochemical Potentials for 1 and 2 38

3. Redox Values for the Compounds 1, 4, 5, and 6 67

4. Molecular Structures for Dyes Used in this Study.....78

LIST OF FIGURES

Figure Page

1. Solar Radiation and Photosynthetic Conversion 3

2. Impact of Human Society on NPP and the Biosphere 5

3. Chemical Structures for Triad Reaction Centers 1–5 11

4. Chemical Structures for Antenna–Reaction Centers 6 and 7 14

5. Antenna–Reaction Center Complex 8 16

6. Antenna–Reaction Center Complex 9 17

7. BiP Containing Triad Reaction Centers 10 and 11 21

8. Structures of Porphyrin 1, the Octasodium Salt of 1 (1a), Porphyrin 2, and the Octasodium Salt of 2 (2a) 33

9. Comparison of Cyclic Voltammograms Taken in Solutions Containing Porphyrin 1a–$IrO_x{\cdot}nH_2O$, Porphyrin 2a–$IrO_x{\cdot}nH_2O$, Malonate–$IrO_x{\cdot}nH_2O$, or Only Supporting Electrolyte 34

10. Oxygen Concentration Relative to Air-saturated Water Measured with a Clark Electrode 35

11. Porphyrin Fluorescence Lifetime Measurements 37

12. Cyclic Voltammograms of Porphyrin 1 and Porphyrin 2 38

13. XRD Pattern of Nanocrysstalline Diamond (NCD) Particles and Co_2O_3NP Decorated NCD Particles 43

14. Cyclic Voltammograms of Co_2O_3NP Particles Deposited on a Glassy Carbon Working Electrode and a Bare Polished Glassy Carbon Electrode 44

15. TEM Image and Particle Size Distribution of Co_2O_3NP on the NCD Support 46

Figure Page

16. SEM Images of Cobalt Oxide Deposits on a Carbon Felt Support.....47

17. Cyclic Voltammograms Taken with a Blank Polished Glassy Carbon Electrode, Nanocrystalline Diamond (NCD) Particles Containing No Cobalt on a Glassy Carbon Electrode, and NCD Particles Containing Photochemically Deposited Cobalt Oxide on a Glassy Carbon Electrode 50

18. Cyclic Voltammograms of a Carbon Felt Electrode without any Cobalt Oxide and a Carbon Felt Electrode Containing Nanocrystalline Diamond Particles with Photochemically Deposited Cobalt Oxide 51

19. Plot Showing a Current Trace During a Controlled Potential Experiment at 1.6 V vs. AgCl/Ag for a Glassy Carbon Electrode Containing a Surface Layer of Co_2O_3NP–NCD Particles 52

20. Zoomed View of the Current Trace Shown in Figure 19 53

21. Current Traces Under an Applied Potential of 1.5 V vs. AgCl/Ag for a Polished Glassy Carbon Electrode and a Glassy Carbon Electrode with a Deposited Film of Co_2O_3NP 53

22. Oxygen Concentration in Solution Measured by an Ocean Optics NeoFox-FOXY Oxygen Probe System During the 2 h Controlled Potential Experiments Shown in Figure 21 54

23. Comparative Voltammograms Showing the Effect of the Presence of Phosphate Buffer on the Activity of the Co_2O_3NP.....55

24. SEM Image of Co_2O_3NP–NCD and HR-TEM Image of a Co Oxide Particle 56

Figure Page

25. SEM Image and TEM Image of Co_2O_3NP–NCD after Catalytic Water Oxidation Experiments 57

26. Normalized Absorption Spectra for Phthalocyanine Derivatives 1, 2, 4, 5, and 6 ...64

27. Cyclic Voltammograms for Compounds 4, 5, and 6 66

28. Schematic Showing the Design of a Tandem Photoelectrochemical Cell for the Production of Solar Fuel from Water with Light.....77

29. Comparison of Absorption Thresholds, Excited State Energetics, Potential for Water Oxidation and Hydrogen Formation, and Coverage of the Solar Spectrum for Oxygenic Photosynthesis and an Ideal Artificial Photosynthetic System 80

30. Absorbance Overlay of Porphyrin 3 Adsorbed to an FTO–SnO_2 Electrode and Phthalocyanine 7 Adsorbed to an FTO–TiO_2 Electrode.....81

31. Comparison of the Photocurrents Produced by FTO–TiO_2 Photoanodes Prepared by Either Co-immobilization of Porphyrin 1 and $IrO_x{\cdot}nH_2O$ or the Adsorption of the Porphyrin 1–$IrO_x{\cdot}nH_2O$ Complex.....88

32. Comparative Performance of Photocells Prepared with Phthalocyanines 7 and 8 ...90

33. Current vs. Time and Current vs. Applied Potential for a Tandem Photoelectrochemical Cell and Both Component Cells Measured in Isolation.....92

34. Photocurrent Trace of a Tandem Photoelectrochemical Cell Incorporating both a TiO_2–5 | PO_4–$IrO_x{\cdot}nH_2O$ Photoanode and a TiO_2–5 Photoanode 93

35. Photocurrent Traces for Several Tandem Cells Representing Different Combinations of Bluer and Redder absorbing Dyes.....95

LIST OF SCHEMES

Scheme Page

1. Mechanism for the Formation of CoNP and Their Spontaneous Air Oxidation to form CO_2O_3NP 42

2. Synthesis of Phthalocyanines 1 and 2 61

3. Synthesis of Phthalocyanine 4 62

4. Synthesis of Phthalocyanine 5 and 6 62

Chapter 1: Evolution of Reaction Center Mimics to Systems Capable of Generating Solar Fuel

Introduction

(This chapter has been adapted from a previously published report: Sherman, B.D., Vaughn, M.D., Bergkamp, J.J., Gust, D., Moore, A.L., and Moore, T.A. Evolution of reaction center mimics to systems capable of generating solar fuel. *Photosynthesis Research*, **2013**, doi: 10.1007/s11120-013-9795-4. I contributed in the design, writing, and editing of this report. See Appendix I for reprint permission details.)

Human activity and especially our reliance on burning fossil fuels has affected planet wide systems, resulting in a precarious future for the global ecosystem.[1] The magnitude of the energy reaching the Earth from the sun makes solar energy conversion a likely part of any alternative energy future that does not rely on the use of fossil fuel yet still satisfies society's energy demand.[2] The immense scale of solar irradiance, however, means little without an efficient means of converting it to useful forms such as electricity or an energy-dense and transportable fuel. Developing a system for converting an abundant and readily available precursor into a fuel using solar radiation as the sole energy input is the primary goal of artificial photosynthesis.[3, 4]

The motivation for and possible impact of the wide scale use of artificial photosynthesis to meet human societal energy needs can be illustrated with reference to Figure 1. Taking into account reflection and absorption of light by the atmosphere, around 65,000 TW reaches the hydrosphere and 15,600 TW reaches land.[5] Photosynthesis converts a portion of this irradiance into energy stored in reduced carbon,

with the net amount of biomass produced in a year (net primary production, NPP) totaling ~112 Pg of fixed carbon.[6] Converting this amount of reduced biomass produced per year to a rate of energy conversion using the conversion factor of 41.3 KJ g^{-1} of fixed carbon[7] yields an average rate of ~156 TW, evenly distributed between terrestrial and marine production.[6, 8, 9] This biomass in turn supports nearly all life on the planet. Humans consume an increasing portion, currently ~25%.[10] An important issue we face is that human appropriation of net primary production (HANPP) comes at the expense of the remainder of biology, and continued population growth will increase the human demand on NPP for food and material. The conversion of land to support HANPP is thought to be driving several Earth systems over boundaries established by natural cycles operating on the geological time scale.[1, 11]

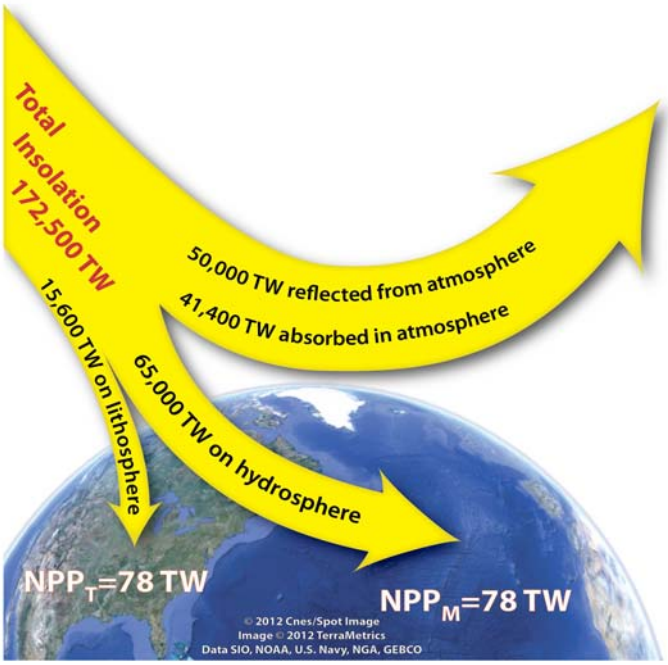

Figure 1. Solar radiation and photosynthetic conversion. Rates of solar energy reaching various portions of the Earth system.[5] While ~80,000 TW reach the surface of the Earth, only 15,600 TW fall on land. About half is within the wavelength range of the photosynthetic pigments; a small fraction of this is stored as chemical energy for the biosphere, i.e. NPP, at an average rate of ~156 TW.

Therefore, any solar-to-fuel system must be vetted against its impact on HANPP; an increase will accentuate an already tenuous ecological situation.[1, 11] Figure 2 outlines energy accounts comparing terrestrial NPP, HANPP, the remainder of NPP after human harvest, and the current non-food energy consumption of modern society. Part (a) illustrates the current state: the human requisition of NPP sums to 20 TW.[10] Driving the global gross domestic product currently consumes ~17 TW, mainly supplied by fossil fuels.[12] Fully displacing fossil fuels with crop-derived biofuel, as shown in (b), must come directly out of NPP. Though carbon neutral, such a scenario is not sustainable as HANPP would increase to nearly 50% NPP. Such a substantial consumption of the total available terrestrial biomass would likely upend the balance of life on the planet as it has

been known for the entirety of human existence. Alternatively, as shown in (c), an artificial photosynthetic system (possibly including a synthetic biological organism or photosynthetic microbe whose culture does not displace native organisms or crops) could supply human energy needs while not depleting the biomass needed to support the global ecosystem. We term this converted solar energy APP or artificial photosynthetic production. This situation would have to satisfy several caveats. For instance any such system should occupy surface area already altered by human activity and minimize the amount of additional land converted for human use. This basic argument seeks not only to focus just on the surface footprint needed to convert solar irradiance to forms of energy usable by humans, but also to consider that any system should not compete for sunlight or land currently used for food production or accessible to nature. To do so will only increase HANPP and further endanger the stability of the global ecosystem.

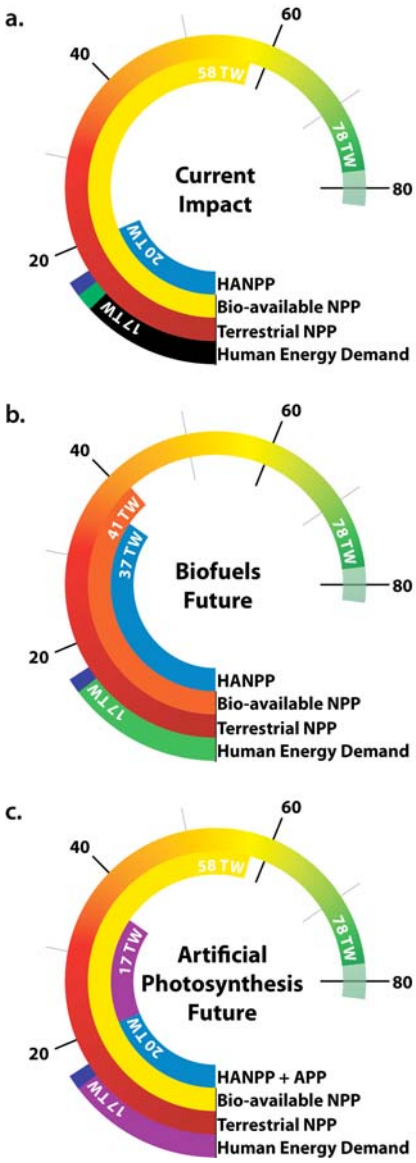

Figure 2. Impact of human society on the NPP and the biosphere. a.) Current impact of human society. NPP is estimated from a consensus of recent models[6] (NPP prior to industrialization is indicated by the shaded extension to 82 TW) and transformed into TW using a previous conversion.[10] HANPP is indicated relative to the amount remaining for all biota.[10] Human energy demands are met using primarily fossil reserves (black fill), while current renewable sources are designated as renewable biofuels (green fill) and renewable nonbiofuels (dark blue fill).[12] b.) Future scenario with complete replacement of fossil fuels by biofuels (green fill), bioavailable NPP is reduced by half, which has catastrophic effects on biodiversity. c.) Future scenario with NPP enhanced by higher efficiency APP deployed within existing footprint of human society, purple fill indicates enhancements to productivity from APP.

In order to exceed current productivity without increasing HANPP, the field of artificial photosynthesis seeks the development of solar-to-fuel systems capable of converting light energy to chemical energy stored in a dense, transportable fuel with efficiencies much greater than those of natural photosynthesis. Such a system, as opposed to that of solar-to-electricity (photovoltaic cells), allows for the storage of solar energy and separates its points of generation and utilization in both time and space. As such, artificial photosynthesis can provide a direct substitute for fossil fuels, which are ideal energy carriers with respect to their high energy densities and easy transport. Although designing and constructing such a system comes with enormous challenges, the natural process of oxygenic photosynthesis offers us a guide.

Oxygenic photosynthesis uses the energy of visible light to carry out the oxidation of water and reduction of carbon dioxide to form oxygen and reduced carbon fuel. Absorption of actinic photons by antennas and reaction center pigments of the photosynthetic machinery initiates charge separation and migration in the reaction center, generating spatially separated oxidizing and reducing equivalents. This conversion of solar energy into electrochemical energy is followed by the production of oxygen from water at the oxygen evolving complex (OEC), the generation of reduced nicotinamide adenine dinucleotide phosphate (NADPH), and creation of a proton gradient across the thylakoid membrane. Dissipation of this proton motive force across the membrane produces adenosine triphosphate (ATP) via ATP synthase, and ATP and NADPH then power the dark reactions of the Calvin-Benson cycle leading to the assimilation of CO_2.

Artificial photosynthesis does not seek to reproduce the natural process, but rather to adapt its basic science to meet the needs of humans. Akin to the process of photosynthesis, an artificial reaction center for solar fuel production needs to absorb light in the visible and near-infrared, generate a charge separated state upon photo-excitation, spatially separate and stabilize the charge separated state, and then transport the photo-generated oxidizing and reducing equivalents to catalysts to carry out the chemical reactions necessary for the production of a fuel (e.g. oxidation of H_2O and production of H_2). Additionally, efficient solar-to-fuel systems incorporating abundant materials are paramount. The study of the underlying photophysical and photochemical processes of model constructs and photoelectrochemical cells will inform the design and aid in the development of such systems.

The work presented in this dissertation covers my contributions to developing an artificial photosynthetic system such as that described above. This endeavor, of course, did not begin with my effort but stemmed from research conducted by the Gust, Moore, and Moore group over the past three decades. The challenge of developing sustainable solar-to-fuel technologies confronts the world as a whole, and, as such, no one technology nor one person shall resolve our energy future. In order to provide the context of my work and place its position in the trajectory of the Gust, Moore, and Moore group's research, the following provides a concise overview from the first triad reaction centers to the solar water splitting photochemical systems described in the final chapter.

Molecular Reaction Centers

An artificial reaction center seeks to perform the same photochemical processes as those observed in the natural system. With the ultimate goal of using light energy to form a fuel, the key functions include: absorption of light across the visible and near-infrared spectra, rapid and efficient transfer of excitation energy from antenna pigments to the reaction center, fast photoinduced charge separation with quantum yields near unity, and prevention of photodamage. Artificial constructs capable of emulating many aspects of the photosynthetic process have been studied, but developing complete systems capable of efficient conversion of light energy into a fuel remains a challenge. The work outlined below shows a research trajectory aimed at this ultimate goal.

Triad Reaction Centers

Covalently linking two molecular analogues of the cofactors involved in the photosynthetic reaction center (e.g. chlorophylls, carotenoids, pheophytins, quinones) produces some of the simplest artificial reaction centers. Study of porphyrin–quinone (P–Q) constructs in particular guided early work in the field carried out by many different researchers. While a P–Q dyad could form the $P^{\bullet+}$–$Q^{\bullet-}$ charge-separated state with proper illumination, the extremely fast decay of this state limits its usefulness.[13] In the natural system, sequential electron transfer steps following photo-induced charge separation spatially separate positive and negative charges across a substantial distance, which greatly slows recombination. Following this design principle, incorporating a third component, one thermodynamically competent for carrying out a second electron transfer after photo-induced charge transfer, proved essential for prolonging the lifetime of the

charge separated state. Synthesis and subsequent study of a carotenoid–porphyrin–quinone triad (C–P–Q)[14] marked a major improvement in stabilizing charge separation in an artificial reaction center and established a platform for engineering improved artificial reaction centers as well as studying other processes characteristic of photosynthesis.

This first triad reaction center, compound **1**, consisted of a ditoluolporphyrin covalently bonded via amide linkages to a benzoquinone electron acceptor and a carotenoid secondary electron donor. Molecule **1** and subsequent carotenoporphyrin–acceptor triads characteristically adopt a linear conformation in solution without folding of the appended groups back over the plane of the porphyrin.[14, 15] Transient spectroscopic studies of C–P–Q show that illumination with visible light (600 nm) generates the porphyrin first excited singlet state, C–^{1}P–Q, with a portion of this species then decaying to the first charge separated state, C–P$^{\bullet+}$–Q$^{\bullet-}$. Competing with recombination, a second electron transfer from the carotenoid to the porphyrin radical cation produces the final charge separated state C$^{\bullet+}$–P–Q$^{\bullet-}$. Monitoring the transient absorbance of the oxidized carotenoid moiety (in the 970 nm region) shows that the final charge separated state has a lifetime of 170 ns in dichloromethane, increasing to 2.5 μs in electrolyte-saturated solvent. Table 1 contains a summary of the results for **1** and several other reaction centers described herein. The final state preserves 1.1 eV of the 1.9 eV of the porphyrin first excited singlet state.[16] The improved stability of the final charge separated state of this complex relative to those of the preceding dyads resides in the greater spatial separation, and therefore electronic decoupling, of the separated charges and the endergonic steps hindering the overall energetically favorable charge recombination.

Table 1. Final charge separated state lifetimes, quantum yield for the formation of the final charge separated state, and experimental conditions for selected artificial reaction centers.

Compound	Solvent	τ^a	Φ^a	$\lambda_{excitation}$ (nm)	Reference
1	dichloromethane	170 ns	0.04	600	Moore *et al.* 1984
	dichloromethane[b]	2.5 μs	0.25	600	Moore *et al.* 1984
2	2-methyltetrahydrofuran	60 ns	0.96	590	Bahr *et al.* 2000
3	2-methyltetrahydrofuran	57 ns	0.95	600	Kodis *et al.* 2004
4	2-methyltetrahydrofuran	170 ns	0.14	590	Liddell *et al.* 1997
	2-methyltetrahydrofuran[c]	1.5 μs	0.10	590	Liddell *et al.* 1997
5	2-methyltetrahydrofuran	340 ns	0.88	590	Kuciauskas *et al.* 2000
6	2-methyltetrahydrofuran	1.3 ns	0.69	560	Kuciauskas *et al.* 1999
7	2-methyltetrahydrofuran	240 ns	0.86	560	Kodis *et al.* 2002
8[d]	2-methyltetrahydrofuran	8.9 ns	0.80	480	Kodis *et al.* 2006
8[e]	2-methyltetrahydrofuran	15.3 ns	0.96	480	Kodis *et al.* 2006
9	1,2-difluorobenzene	230 ps	~1	480	Terazono *et al.* 2009
11	benzonitrile	3.8 μs	0.52	740	Megiatto *et al.* 2012

[a] lifetime and quantum yield given for the final charge separated state of the respective reaction center
[b] saturated with tetra-n-butylammonium tetrafluoroborate
[c] 77 K (all other values in table at room temperature)
[d] M = 2H (freebase form, see Fig. 5)
[e] M = Zn (Zn inserted form, see Fig. 5)

The C–P–Q triad in turn provided a foundation for further elaboration and improvement in reaction center design and function. Several iterations of the triad reaction center are shown in Figure 3. Alterations of the electronic coupling, as in changing the orientation of the amide linker in **4** and **5**,[17] redox properties,[18] and type of

acceptor moiety[19, 20] in the reaction center led to triad complexes with improved lifetimes and yields of the final charge separated state. The extension of the triad design led to the creation of tetrad and pentad complexes which demonstrated the feasibility of carrying out multiple electron transfer steps across larger complexes resulting in greater spatial separation of the charges and long lifetimes for the charge separated state.[21-24]

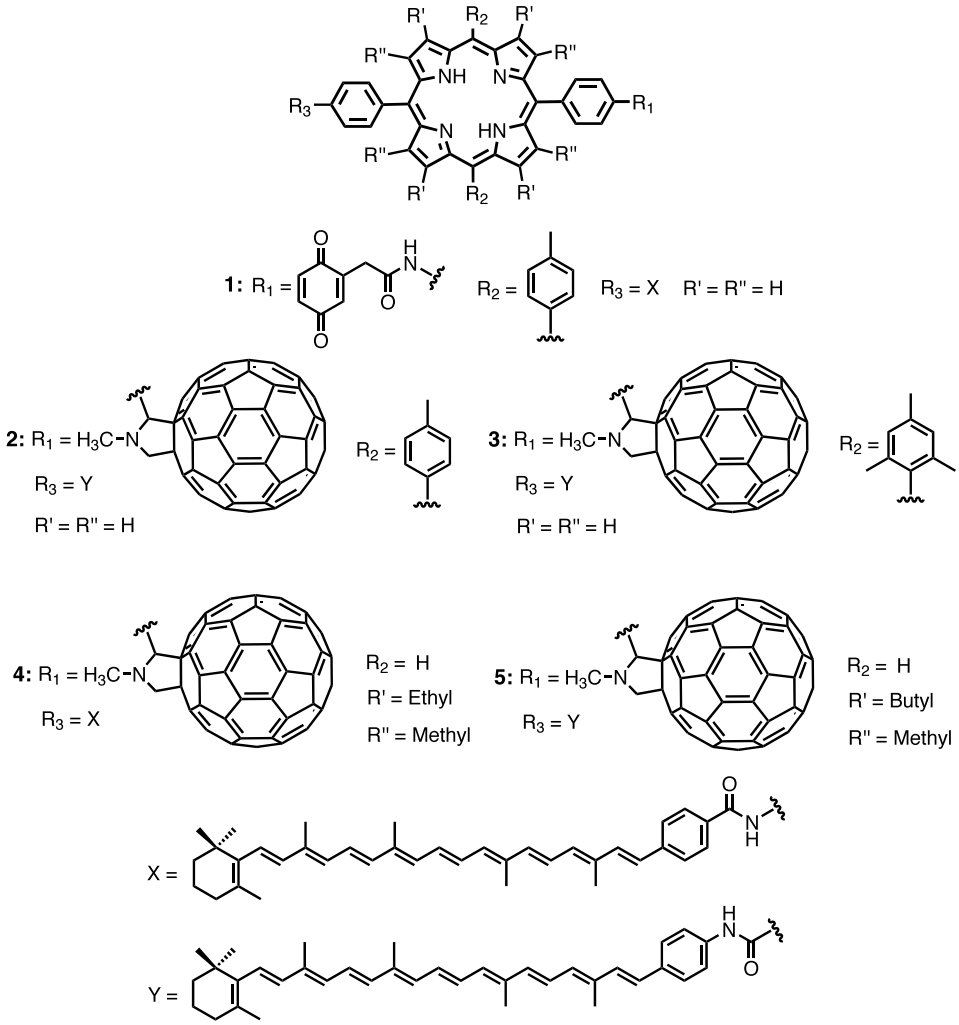

Figure 3. Chemical structures for triad reaction centers **1**-**5**.

The introduction of a fullerene electron-accepting unit in place of a quinone advanced the performance of the artificial reaction centers.[20] Although, not observed in any known biological system, the use of a fullerene acceptor moiety offers definite advantages in imitating the photochemical processes observed in natural photosynthesis. With small solvent and internal reorganizational energies upon reduction and relative insensitivity of the radical anion to the solvent dielectric constant compared to quinones, fullerenes perform remarkably well in reaction center constructs.[20, 25, 26] In comparison with triad complexes employing quinones, those with fullerene acceptor moieties in general show more rapid photo-induced charge separation and slower charge recombination, can perform charge separation in a variety of solvents and even at low temperature in glasses,[17, 20] and can recombine to triplet excited states rather than the ground state.[18, 20] Such behavior is characteristic of the natural system, making fullerenes an ideal example where compounds alien to biology can substantially aid in the development and performance of overall biomimetic artificial systems.[27]

The first iteration of the C–P–C_{60} based triad featuring a β-alkyl substituted porphyrin, **4**, formed the final $C^{\bullet+}$–P–$C_{60}^{\bullet-}$ state with a yield of 0.14 in 2-methyltetrahydrofuran.[20] Spectroscopic studies showed that the decay of this state, with a lifetime of 170 ns, led to the formation of the carotenoid triplet state, ^{3}C–P–C_{60}. Progressive molecular engineering of the complex by introduction of a lower potential carotenoid (compare **4** and **5**),[17] introduction of a ditoluolporphyrin in **2**,[28] and then dimesitylporphyrin in **3**[18] steadily improved the performance of the reaction center, producing complexes capable of obtaining quantum yields for the final charge separated state near unity. The trajectory of triad reaction centers from the first C–P–Q complexes

to the later fullerene-containing analogues demonstrated the ability of synthetic molecular constructs to efficiently transform light energy to chemical potential with charge-separated state lifetimes long enough for conversion of the conserved excitation energy to a useful form, for example by formation of chemical bonds or generation of a pH gradient across a membrane.[29, 30]

Antenna–Reaction Centers

The single chromophore in a triad reaction center limits the total usable region of the spectrum; nature, by contrast, employs several different pigment molecules such as chlorophylls, carotenoids, cyanobilins, and erythrobilins for wide coverage of the solar spectrum. In the photosynthetic process, antenna pigment–protein complexes absorb most of the actinic light and channel the resultant excitation energy to the reaction center leading to charge separation.[31]

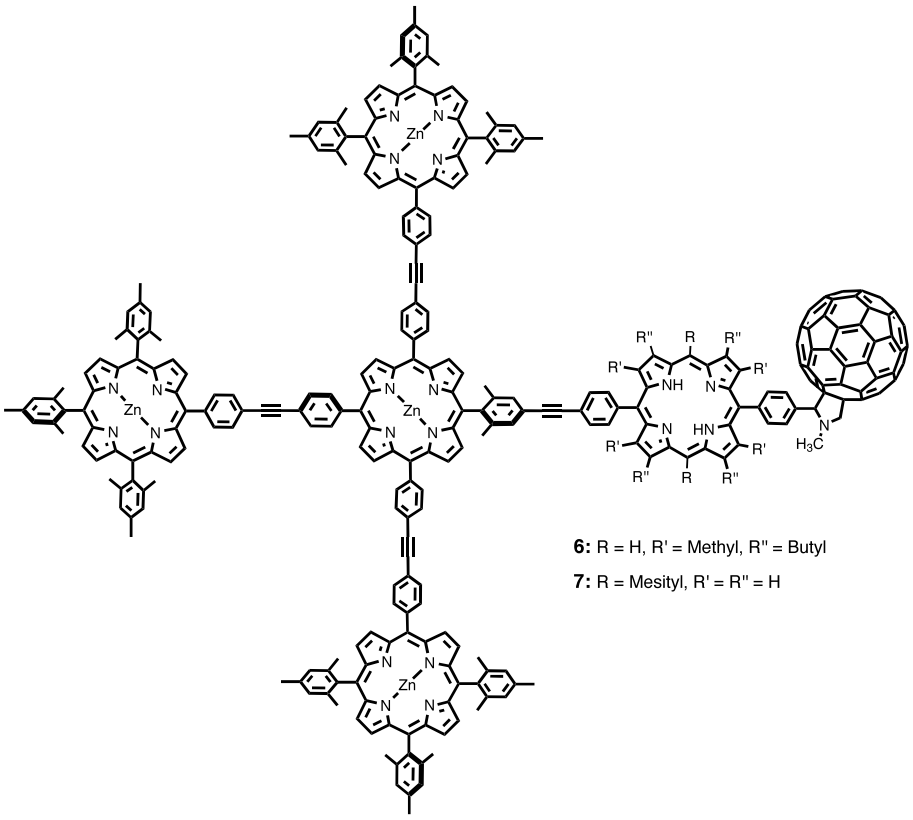

Figure 4. Chemical structures for antenna–reaction centers **6** and **7**.

In an artificial context, multiporphyrin antenna reaction center complexes provided the basis for later multichromophore arrays and also established a means of studying energy transfer to a reaction center. An antenna moiety consisting of four Zn(II)tetrarylporphyrins - a central Zn(II)porphyrin connected to the meso positions of three peripheral porphyrins - was attached to a free base porphyrin–fullerene reaction center ($(P_{ZP})_3$–P_{ZC}–P–C_{60}, **6**). This system established the feasibility of specifically exciting the antenna to induce charge separation in the attached reaction center (Figure 4).[32] Optimizing the design of the $(P_{ZP})_3$–P_{ZC}–P–C_{60} reaction center by replacing the diarylporphyrin of **6** with tetraarylporphyrin in **7**, and thereby increasing the potential of

the electron donating porphyrin, provided more thermodynamic driving force for electron transfer from the antenna porphyrins to the radical cation of the freebase porphyrin and led to a hole delocalization in the antenna and longer lifetime of the final charge separated state.[27] The structural differences between **6** and **7** also led to different HOMO orbital types in the freebase porphyrin moieties: the β-alkyl substituents of the freebase porphyrin in **6** induce an a_{1u}-type HOMO with nodes at the meso positions, whereas the freebase porphyrin of **7** without β substituents and mesityl groups at the 10,20-meso positions exhibits an a_{2u}-type HOMO with lobes at the meso positions. These differences in the HOMO orbital structure combined with the steric influence of the β-alkyl groups of **6,** which results in an increased average dihedral angle and less π-π overlap between the meso aryl group and the porphyrin macrocycle, also create a substantial increase in the rate of singlet-singlet energy transfer rates, better antenna function, and increased quantum yield of final charge separation for **7** as compared to **6**.[27] Extending the concept of this design, an antenna–reaction center complex comprised of five bis(phenylethynyl)anthracene (BPEA) antenna molecules linked to a hexaphenylbenzene core and covalently linked to a porphyrin-fullerene complex **8** (Figure 5), carried out efficient charge separation with better coverage of the spectrum from 430 to 480 nm.[33]

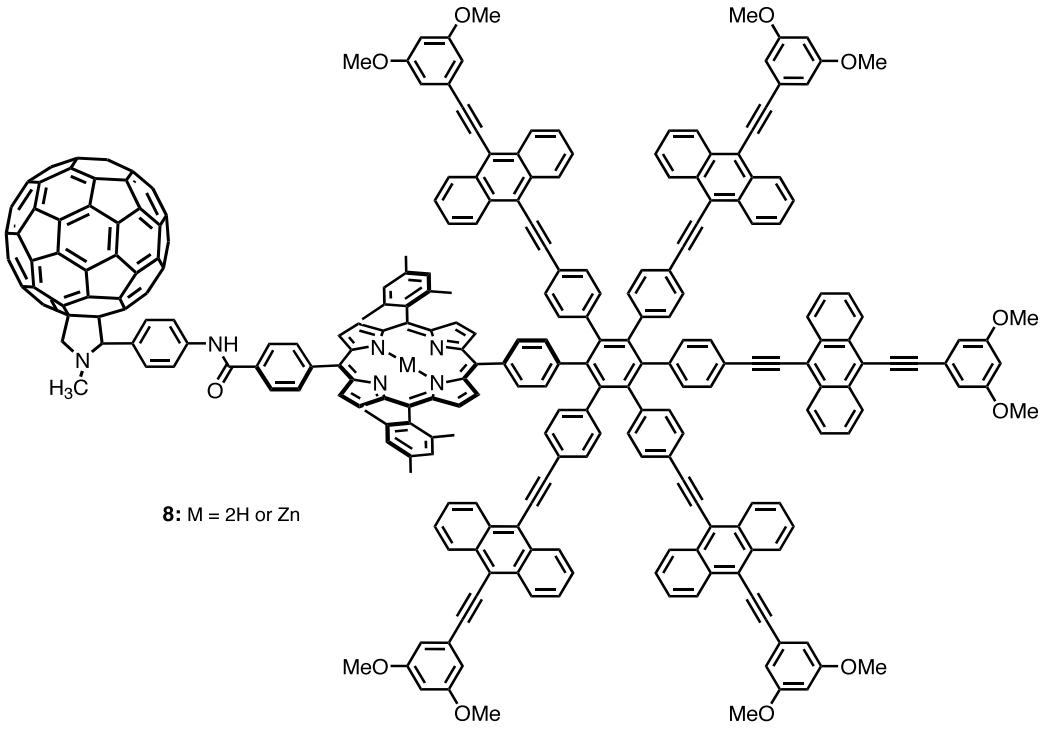

Figure 5. Antenna-reaction center complex **8**.

Further elaboration of the antenna–reaction center came with the development of complex **9** (Figure 6), consisting of several different chromophore moieties. Centered on a hexaphenylbenzene core, two bis(phenylethynyl)anthracene, two borondipyrromethene, and two Zn(II)tetraarylporphyrin dyes comprised an antenna complex with coverage across the visible spectrum.[34] Coordination of a dipyridyl functionalized fullerene to the two adjacent Zn(II)porphyrins of the antenna complex completed the formation of a multiantenna reaction center complex **9**. Excitation of any of the antenna pigments in the complex leads to rapid light induced electron transfer to the fullerene. Developing molecular design strategies for broad spectral coverage with funneling of excitation energy to charge transfer centers, such as those outlined above, plays a central role in the development of efficient solar-to-fuel systems.

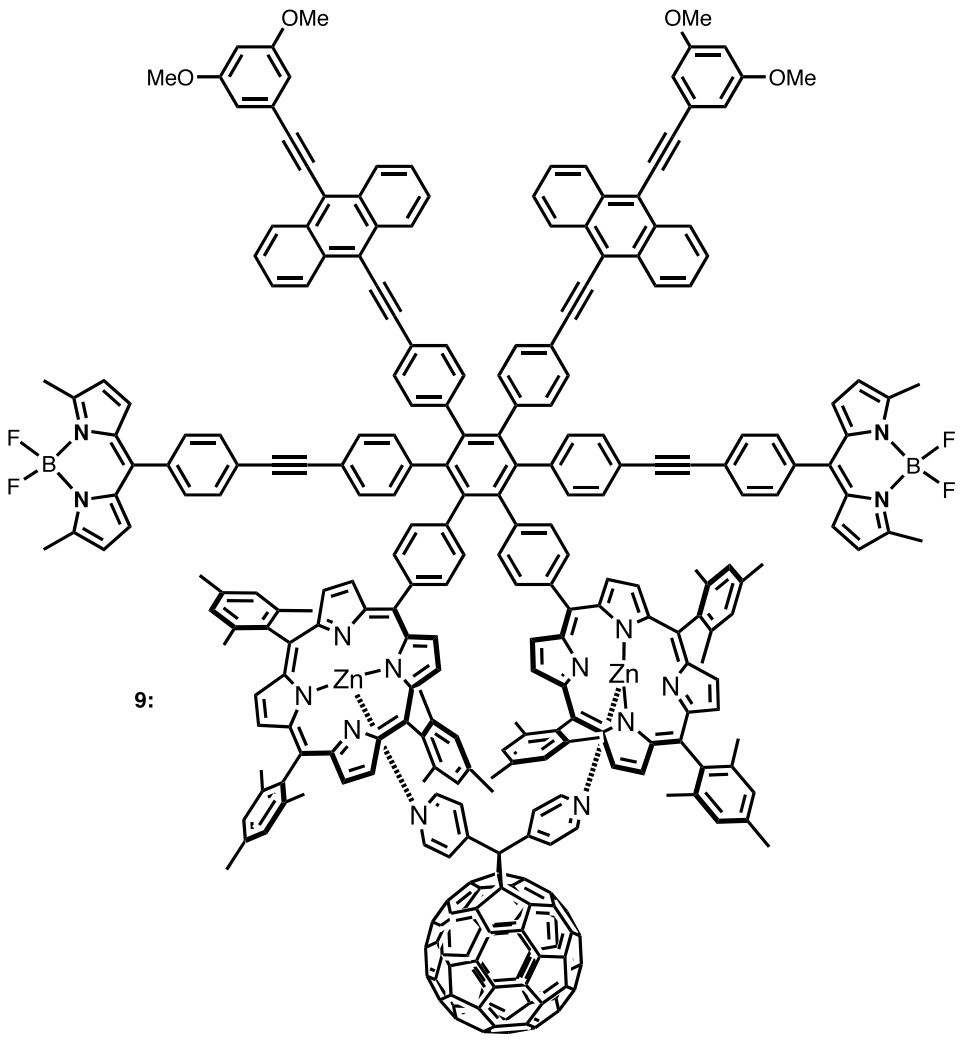

Figure 6. Antenna–reaction center complex **9**.

Photoregulation

During photosynthesis, the process of non-photochemical quenching (NPQ) enables the organism to avoid the buildup of energetic, and damaging, intermediates that would otherwise form under high light intensities.[35, 36] Avoiding destructive intermediates formed under such conditions could likely increase the longevity of artificial systems in a similar manner. A pentad reaction center, consisting of a porphyrin primary donor,

fullerene acceptor, two antenna pigments, and a dihydroindolizine (DHI) photochrome control moiety, demonstrated the ability of an artificial reaction center to reversibly change the quantum yield of charge separation based on the intensity of incident light.[37] Under low white light levels, in which the DHI exists primarily in the closed form, the reaction center carries out light induced charge separation with a quantum yield of 0.82. Under high white light intensities, the quantum yield of a solution of the pentad decreases to 0.27 as photoisomerization converts some of the photochrome to its open, betaine form (BT), a conformation competent for rapidly quenching the porphyrin excited singlet state by energy transfer. Upon forming BT at high white light intensities, the quenching of the porphyrin excited state prevents charge separation in the reaction centers of the isomerized molecules, markedly reducing the overall quantum yield for this process.

Charge Separation Across a Membrane

Along with light capture and formation of a charge-separated state, an artificial solar-to-fuel system must convert incident light energy to some other useful form. In photosynthesis, photo-induced charge transfer across the thylakoid membrane is coupled to proton shuttling across the bilayer, thereby establishing a proton gradient. Dissipation of the proton imbalance back across the membrane then drives the production of adenosine triphosphate (ATP) via a transmembrane ATP-synthase enzyme. Producing constructs capable of mimicking this process can offer insight into the design and development of artificial systems for solar energy conversion.

A study to this end demonstrated that illumination of a phospholipid bilayer impregnated with C–P–Q type reaction centers and separating a solution containing a

sacrificial electron donor from that with an acceptor species results in the passage of photocurrent in a circuit bridging the bilayer membrane.[38] Building off this work, imbedding a similar C–P–Q type reaction center in the bilayer of a liposome set the basis of a system capable of pumping protons across the lipid layer.[29] The overall amphiphilic nature of the C–P–Q complex used directs the asymmetric insertion of the reaction center into the liposome with the carotenoid moiety toward the interior and the more polar quinone to the exterior. Excitation of the complex generates an oxidizing potential inside and a reducing potential around the periphery of the liposome. A freely diffusing quinone electron/proton carrier within the membrane of the liposome with a midpoint potential between that of the oxidized carotenoid and reduced quinone moieties of the reaction center shuttles protons across the membrane, resulting in the acidification of the interior of the liposome. This results in the creation of a light induced potential gradient across the bilayer.

In order to harness the proton motive force generated in this system, a CF_0F_1-ATP synthase was incorporated into the liposome along with the reaction center and redox mediator components.[30] With proton translocation driven by the photocycle described above, dissipation of the pH gradient coupled to the catalytic conversion of ADP and P_i to ATP as carried out by the CF_0F_1-ATP synthase resulted in the net conversion of incident light energy into that of a high-energy chemical species. Quantitative analysis of the system reveals that in low light the absorption of 14 photons results in the production of 1 ATP molecule and, with illumination by 633 nm light, roughly 4% of the absorbed energy is conserved in the form of a chemical bond.[30]

In a subsequent study, the same C–P–Q reaction center was used in conjunction with a quinone-like molecule whose ability to bind Ca^{2+} is modulated by the redox status.[39] This system was capable of pumping Ca^{2+} ions against a concentration gradient by the asymmetric arrangement of the C–P–Q reaction center in liposomes. Although the quantum yield was only 1%, a significant electrical potential was measured across the membrane extending Mitchell's mechanism of accumulating membrane potential using a redox loop to divalent cations in addition to protons.

Mimicking Proton Control During Electron Transfer

The $Tyrosine_Z$–Histidine190 (Tyr_Z–His190) pair of photosystem II (PSII) is thought to undergo proton coupled electron transfer (PCET) as it serves as an electron transfer mediator between P_{680} and the oxygen evolving complex (OEC).[40, 41] The interaction between Tyr_Z and His190 likely serves to tune the potential of the tyrosine residue so that it lies between that needed for the reduction of the photo-generated P_{680}^+ and the potential for oxidizing the OEC. Serving as an intermediary between P_{680} and the OEC, Tyr_Z–His190 prevents charge recombination that would otherwise compromise the catalytic activity of the Mn_4O_5Ca cluster of the OEC. This is especially important given that four oxidizing equivalents must accrue on the OEC to carry out the oxidation of one molecule of water. To improve artificial systems, utilizing a similar design feature could also aid in preventing back electron transfer after photo-induced charge separation.

With the natural system as a template, porphyrin construct **10** (Figure 7) was designed bearing a benzimidazolphenol (BiP) moiety with the phenolic hydrogen capable of forming a hydrogen bond with the lone pair electrons of the imidazole nitrogen.[42, 43]

Chemically functionalizing the porphyrin to adsorb to the surface of a colloidal TiO_2 nanoparticle enables the assembly of **10** as shown in Figure 7. This molecule–nanoparticle complex is reminiscent of the triad reaction centers discussed earlier, consisting of a porphyrin light absorber (PF_{10}), TiO_2 primary electron acceptor, and BiP electron donor.[42] Electron paramagnetic resonance studies of this complex reveal phenoxyl radical formation in the complex upon excitation of the porphyrin as a result of light induced charge separation. Given that the potential for the oxidation of the BiP moiety lies at 1.00 V vs. SCE, the photo-formed $BiP^{\bullet+}$–PF_{10}–$TiO_2^{\bullet-}$ state is thermodynamically competent for water oxidation.

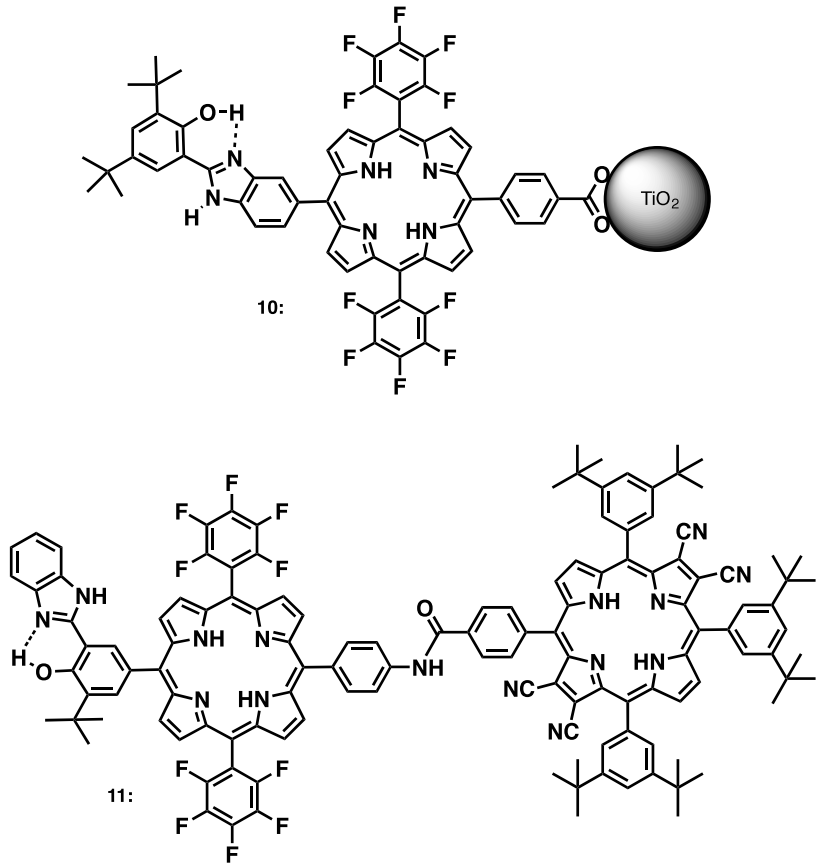

Figure 7. BiP containing triad reaction centers **10** and **11**.

A continuation of this study led to the development of **11** (Figure 7), a fully organic triad complex with a tetracyanoporphyrin (TCNP) serving as the primary acceptor in place of a TiO_2 nanoparticle.[44] This complex bears considerable similarity to the Tyr_Z–His190–P_{680}–$Phoe_{D1}$ portion of the electron transport chain in PSII. Time resolved spectroscopic investigation of this reaction center in benzonitrile reveals that with excitation of TCNP the complex undergoes an initial electron transfer between the PF_{10} and TCNP resulting in Bi–PhOH–$PF_{10}^{\bullet+}$–$TCNP^{\bullet-}$. Competing with charge recombination, a second, rapid electron transfer then occurs between the benzimidazole–phenol and oxidized PF_{10}, presumably resulting in BiH^{+}–$PhO^{\bullet}$–PF_{10}–$TCNP^{\bullet-}$. This state forms with a quantum yield of 0.52 and persists with a 4 μs lifetime, which is longer than those of many of the carotenoporphyrin–acceptor reaction centers of prior studies. Presumably, the final charge separated state reflects transfer of the phenolic proton to the nitrogen of the benzimidazole. Based on reduction potentials for model compounds,[43] the $PF_{10}^{\bullet+}$ would not generate sufficient driving force for the formation of the Bi–$PhOH^{\bullet+}$–PF_{10}–$TCNP^{\bullet-}$, implying a PCET leading to the formation of the BiH^{+}–$PhO^{\bullet}$–PF_{10}–$TCNP^{\bullet-}$ state. The long-lived charge separated state and high potential of the oxidized BiH^{+}–$PhO^{\bullet}$ (1.04 V vs. SCE), make this reaction center type an ideal candidate for incorporation into the photoanode of a photoelectrochemical device for light driven water splitting.

Employing Reaction Centers for Water Splitting

The work described to this point has illustrated artificial photosynthetic systems for light absorption and charge separation via photo-induced electron transfer. Fuel production requires “wiring” such reaction centers to catalysts. One approach to doing so

is to combine electrode architectures reminiscent of those used in dye sensitized solar cells with artificial reaction centers to produce photoelectrochemical water splitting cells. This constitutes the primary interest of my graduate study. The following chapters will cover various aspects of this solar-to-fuel platform.

Conclusion

This account shows the preceding arc of research leading to that described in the following chapters, from building simple molecular reaction center constructs to developing complete systems for the conversion of solar energy to a fuel. Efficient and economical systems which can generate a sustainable fuel from sunlight and a widely available precursor such as water are requisite to meeting future human energy demand in a way that does not endanger the diversity of life on the planet or the health and wellbeing of its inhabitants. Developing and improving the technologies for such systems represents a principal challenge of the modern world. The complications of fulfilling energy demand requires a host of sustainable technologies for varying locales. Certainly, solar energy will play a substantial role, and chemical fuels provide the greatest possible flexibility of usage.

I have pursued this challenge through the study of artificial reaction centers designed to mimic aspects of photosynthesis. As the only process capable of converting solar energy to a chemical fuel on a planet wide scale, photosynthesis provides a model for doing so by artificial means. The development and study of molecular reaction centers has culminated in the development of a first generation of dye sensitized photoelectrochemical cells for solar-to-fuel conversion. Substantial work remains in

advancing the viability of this system. Ultimately the grand challenge of supplying sustainable energy requires contributions from many researchers and several fields of science; our best hope lies in developing a range of renewable energy technologies and contributing to a well informed and well equipped global society.

Chapter 2: A Porphyrin-Stabilized Iridium Oxide Water Oxidation Catalyst

Introduction

(This chapter has been adapted from a previously published report: Sherman, B.D., Pillai, S., Kodis, G., Bergkamp, J., Mallouk, T.E., Gust, D., Moore, T.A., Moore, A.L. A porphyrin–stabilized iridium oxide water oxidation catalyst. *Canadian Journal of Chemistry,* **2011**, 89: 152. I contributed in the synthesis of iridium oxide constructs, electrochemical experiments, detection of oxygen formation, and the design, writing, and editing of this report. See Appendix I for reprint permission details.)

Work carried out by Harriman *et al.* over twenty years ago demonstrated that hydrated iridium oxide ($IrO_x \cdot nH_2O$) is an active, stable, and efficient catalyst for water oxidation.[45-47] Colloidal $IrO_x \cdot nH_2O$ in solution with either $Ru(bpy)_3^{2+}$ or porphyrin dye could carry out the photochemical generation of O_2 from water.[45, 47] These studies, however, required the presence of a strong oxidant ($S_2O_8^{2-}$) to generate the photo-oxidized dye that then would oxidize the catalyst. Subsequent electrochemical studies by other groups investigated techniques for immobilizing $IrO_x \cdot nH_2O$ on the surface of transparent glass electrodes.[48-50] Yagi *et al.* showed that adsorbed layers formed on the surface of indium doped tin oxide (ITO) and fluorine doped tin oxide (FTO) electrodes when the electrodes were allowed to soak in a solution containing citrate-stabilized colloidal $IrO_x \cdot nH_2O$.[49, 50] Electrochemical studies on prepared electrodes showed the onset of catalytic current near 1.0 V vs. SCE (1.04 V vs. Ag/AgCl) at pH 5.3 (no $IrO_x \cdot nH_2O$ in solution). Murray *et al.* have studied $IrO_x \cdot nH_2O$ particles formed at high pH, without the use of stabilizing groups, both on a surface and in solution.[51, 52] Their

work has shown the need for only 0.15 V of overpotential (potential beyond the thermodynamic requirement needed to support a certain reaction rate) for the onset of water oxidation and 100% current efficiency for the generation of O_2 from water at an overpotential of 0.29 V.[51, 52] While the catalytic activity of $IrO_x{\cdot}nH_2O$ has been well established, only recently has a system capable of driving the catalyst photoelectrochemically been demonstrated.[53]

In collaboration with the Mallouk group at The Pennsylvania State University, the Gust, Moore, and Moore group reported the development of a water splitting photoelectrochemical cell employing a $Ru(bpy)_3^{2+}$–$IrO_x{\cdot}nH_2O$ based photoanode.[53] In that work, the dye–$IrO_x{\cdot}nH_2O$ complex was formed using a heteroleptic $Ru(bpy)_3^{2+}$ complex containing phosphonate groups on one of the bipyridyl ligands and a malonate group on another. Previous work had demonstrated the preference of carboxylate groups over phosphonate groups for binding to the surface of $IrO_x{\cdot}nH_2O$.[54] This chemistry allowed for the formation of small $IrO_x{\cdot}nH_2O$ particles (1–5 nm), capped with $Ru(bpy)_3^{2+}$ dye molecules containing exposed phosphonate groups.[53, 54] The dye–$IrO_x{\cdot}nH_2O$ constructs could then be attached to metal oxide semiconductors, such as titanium dioxide (TiO_2), via the phosphonate group.

In this system, the photoanode consisted of the dye–$IrO_x{\cdot}nH_2O$ complex adsorbed to a TiO_2 layer on top of an FTO electrode. When this photoanode was combined with a platinum cathode in a photoelectrochemical cell, the cell produced a photocurrent of 12.7 $\mu A\ cm^{-2}$ upon illumination with 450 nm light at an intensity of 7.8 $mW\ cm^{-2}$, giving an internal quantum yield of 0.9%.[53] Three principal factors limited the performance of this system: slow electron transfer from the $IrO_x{\cdot}nH_2O$ catalyst to the oxidized dye, bleaching

of the dye likely due to nucleophilic attack on the oxidized dye, and the need for applied bias to achieve overall water splitting. Transient spectroscopic studies showed electron transfer from the $IrO_x \cdot nH_2O$ to the photo-oxidized dye (2.8 ms) to be almost an order of magnitude slower than the back electron transfer from TiO_2 to the oxidized dye (0.37 ms).[53] An additional issue with $Ru(bpy)_3^{2+}$ complexes as photosensitizers is that they absorb strongly in the blue but cannot effectively utilize light in the red region of the spectrum.

The work outlined herein seeks to improve the stability, electron transfer rate, and spectral properties of the dye–$IrO_x \cdot nH_2O$ complex by incorporating a porphyrin rather than the $Ru(bpy)_3^{2+}$ dye. I report the synthesis of a porphyrin–$IrO_x \cdot nH_2O$ complex which shows electrochemical catalytic response similar to other $IrO_x \cdot nH_2O$ complexes.[49] Finally, fluorescence lifetime measurements indicate quenching of the porphyrin fluorescence in the porphyrin–$IrO_x \cdot nH_2O$ complex.

Experimental

Materials

Sephadex with a 5,000 molecular weight cutoff, Na_2HPO_4, NaH_2PO_4, tetrabutylammonium hexafluorophosphate and benzonitrile were obtained from Sigma Aldrich. Benzonitrile was distilled prior to use. K_2IrCl_6 was used as received from Alfa Aesar. KNO_3 was obtained from Fluka. Tetrahydrofuran for synthesis was distilled from sodium/benzophenone. Dimethylformamide was dried over activated 4 Å molecular sieves. Dichloromethane used for chromatography was distilled from calcium hydride.

Porphyrin Synthesis

General Methods: 5,10,15,20-Tetrakis(4-bromomethylphenyl)porphyrin was synthesized by a published method.[55] The malonate substitution and cleavage of the esters were performed by literature procedures used for related compounds.[56-58] Palladium insertion was achieved by adapting Durantini's procedure.[57]

*Porphyrin **1***

Sodium hydride (387 mg, 16 mmol) was suspended in 10 mL of dry THF under nitrogen atmosphere. Diethyl malonate (0.61 ml, 4 mmol) in 20 mL THF was added dropwise under ice cooling. After being stirred for 1 h at room temperature, a solution of 5,10,15,20-tetrakis(4-bromomethylphenyl)porphyrin (200 mg, 0.20 mmol) in 20 mL of dry THF was added dropwise to the mixture and stirred for 1 h. The reaction mixture was then poured into an ice-cold saturated NH_4Cl solution. The aqueous layer was extracted with CH_2Cl_2. The organic solution was washed thoroughly with water and dried over Na_2SO_4. The crude material was purified by column chromatography on silica gel (solvent CH_2Cl_2/EtOAc 20/1). Yield: 120 mg (45%). ^{1}H NMR: (400 MHz, $CDCl_3$, RT): δ -2.82 (s, 2H, NH), 1.34 (t, 24H, *J* = 7.2 Hz, ethyl CH_3), 3.56 (d, 8H, *J* = 7.7 Hz, CH_2), 3.96 (t, 4H, *J* = 7.7 Hz, CH), 4.3(m, 16H, *J* = 7.2 Hz, ethyl CH_2), 7.58 (d, 8H, *J* = 8.0 Hz, phenyl–CH_2), 8.10 (d, 8H, *J* = 8.0 Hz, phenyl–CH_2), 8.77 (s, 8H pyrrolic H). MALDI-TOF-MS m/z: calcd. for $C_{76}H_{78}N_4O_{16}$ 1302.54, obsd. 1302.67. UV-vis (CH_2Cl_2): λ_{max} 419, 516, 551, 591, 647 nm.

*Porphyrin **1a***

A 50 mg (0.038 mmol) portion of **1** and finely ground sodium hydroxide (292 mg, 7.5 mmol) were suspended in 40 mL of ethanol. The mixture was refluxed for 15 h and a precipitate was formed. The mixture was cooled to room temperature and filtered. The residue was washed with a little ice-cold ethanol and dried in high vacuum. Yield: 43 mg (89.5%). ^{1}H NMR: (400 MHz, D_2O, RT): δ 3.3 (d, 8H, *J* = 7.9 Hz, CH_2), 3.59 (t, 4H, *J* = 7.9 Hz, CH), 7.58 (d, 8H, *J* = 7.8 Hz, phenyl–CH_2), 7.9 (d, 8H, *J* = 7.8 Hz, phenyl–CH_2), 8.47 (s, 4H, pyrrolic H), 8.98 (s, 4H, pyrrolic H). MALDI-TOF-MS m/z: calcd. for $C_{76}H_{78}N_4O_{16}$ 1079.02, obsd. 1079.41. UV-vis (H_2O): λ_{max} 415, 519, 557, 582, 635 nm.

*Porphyrin **2***

To a solution of **1** (24 mg, 0.018 mmol) in 10 mL DMF was added palladium(II) chloride (32.6 mg 0.18 mmol). The mixture was stirred for 1 h at 55^0C under nitrogen. The solvent was removed under reduced pressure and the compound was purified by column chromatography on silica gel (solvent CH_2Cl_2/EtOAc 20/1). Yield: 21 mg (81%). ^{1}H NMR: (400 MHz, $CDCl_3$, RT): δ 1.35 (t, 24H, *J* = 7.2 Hz, ethyl CH_3), 3.56 (d, 8H, *J* = 7.7 Hz, CH_2), 3.96 (t, 4H, *J* = 7.7 Hz, CH), 4.3 (m, 16H, *J* = 7.2 Hz, ethyl CH_2), 7.58 (d, 8H, *J* = 8.0 Hz, phenyl–CH_2), 8.06 (d, 8H, *J* = 8.0 Hz, phenyl–CH_2), 8.75 (s, 8H pyrrolic H). MALDI-TOF-MS m/z: calcd. for $C_{76}H_{78}N_4O_{16}$ 1302.54, obsd. 1302.67. UV-vis (CH_2Cl_2): λ_{max} 416, 523 nm.

*Porphyrin **2a***

Porphyrin **2** (20 mg, 0.014 mmol) and finely ground sodium hydroxide (107 mg, 2.7 mmol) were suspended in 20 mL of ethanol. The mixture was refluxed for 15 h and a precipitate was formed. The mixture was cooled to room temperature and filtered. The residue was washed with a little ice-cold ethanol and dried in high vacuum. Yield: 17 mg (88%). ^{1}H NMR: (400 MHz, D_2O, RT): δ 3.28 (d, 8H, *J* = 7.9 Hz, CH_2), 3.59 (t, 4H, *J* = 7.9 Hz, CH), 7.58 (d, 8H, *J* = 7.8 Hz, phenyl–CH_2), 7.96 (s, 8H phenyl–CH_2), 8.47 (s, 8H, pyrrolic H). UV-vis (H_2O): λ_{max} 413, 522 nm.

Preparation of the Porphyrin–$IrO_x{\cdot}nH_2O$ Complex

The complex was formed in a solution containing 50 μM of the porphyrin sodium salt, either **1a** or **2a**, and 1 mM of K_2IrCl_6. The solution was adjusted to pH 8 with 0.25 M NaOH and heated to 35 °C, and the reaction was allowed to proceed (~2–3 days) until the starting red-brown solution became pale yellow. The pH of the solution was monitored throughout the reaction period and NaOH was added as necessary to maintain mildly basic pH. The resulting colloids were either used as such or purified by size exclusion chromatography using a Sephadex gel filtration medium. The malonate–$IrO_x{\cdot}nH_2O$ was prepared as previously described.[54]

Electrochemical Measurements

All electrochemical measurements were done using a CH Instruments 760D potentiostat along with software provided by the manufacturer. A glassy carbon or platinum working electrode was used as indicated along with a Ag/Ag^+ quasi-reference or

Ag/AgCl (in saturated KCl) reference and a Pt wire mesh counter electrode. Ferrocene was used to calibrate the potential of the Ag/Ag^+ quasi reference with Fc^+/Fc taken as 0.45 V vs. SCE. Cyclic voltammetric (CV) measurements of **1** and **2** were done in benzonitrile with 0.1 M tetrabutylammonium hexafluorophosphate. Porphyrin–$IrO_x \cdot nH_2O$ measurements were done in 0.1 M KNO_3 aqueous solution at the scan rates and potentials indicated. Some measurements were taken in 0.1 M phosphate buffer with pH near 7 as indicated.

Clark Electrode Measurements

A Yellow Springs Instrument Co. 5300 Biological Oxygen Monitor was used to measure the $\%O_2$ in solution with air saturated solution set as 100% O_2. Solutions were purged of O_2 by bubbling Ar until reaching a level of 30-50% O_2. Argon was then flowed into the headspace of the cell to keep atmospheric O_2 from entering. After reading a stable $\%O_2$ level for 2-5 min, the amperometry experiment was initiated. A line was fitted to the stable $\%O_2$ reading for the 60 s before applying potential in the experiment and was subtracted from the trace to give $\Delta\%O_2$ (change in $\%O_2$ during the experiment) as show in Figure 3.

Time-resolved Fluorescence Measurements

Fluorescence decay measurements were performed by the time-correlated single-photon-counting method. The excitation source for the system was a mode-locked Ti:Sapphire laser (Spectra Physics, Millennia-pumped Tsunami) with a 130 fs pulse duration operating at 80 MHz. The laser output was sent through a frequency doubler and

pulse selector (Spectra Physics Model 3980) to obtain 370-450 nm pulses at 4 MHz. Fluorescence emission was detected at the magic angle using a double grating monochromator (Jobin Yvon Gemini-180) and a microchannel plate photomultiplier tube (Hamamatsu R3809U-50). The instrument response function was 35–55 ps. The spectrometer was controlled by software based on the LabView programming language and data acquisition was done using a single photon counting card (Becker-Hickl, SPC-830).

Data analysis was carried out using locally written software (ASUFIT) developed in a MATLAB environment (Mathworks Inc.). Random errors associated with the reported lifetimes obtained from fluorescence were typically ≤ 5%.

Results and Discussion

This work centers on the use of tetrakis(methylphenylmalonate)porphyrins as stabilizers for the formation of $IrO_x \cdot nH_2O$ colloidal solutions. It builds on the previous finding that bidentate carboxylic acid groups act as effective stabilizers for the formation of small $IrO_x \cdot nH_2O$ colloidal particles.[54] The porphyrins used in this study contain methylphenylmalonate groups at each of the para positions of the four *meso* phenyl groups; it is expected that the colloidal particles formed with these stabilizers will be similar in structure to those reported by Hoertz *et al.*[54]

Colloidal $IrO_x \cdot nH_2O$ particles were successfully formed using porphyrin **1a** and its Pd analogue, **2a**, shown in Figure 8 along with their protected ester forms (**1** and **2**). Synthesis of the $IrO_x \cdot nH_2O$ colloids entailed heating a solution containing K_2IrCl_6 and the porphyrin at 35°C for ~2–3 days. The initial pH of the solution was adjusted to near pH 8

with NaOH and monitored and adjusted throughout the synthesis to maintain moderately basic conditions. The resulting colloidal solution was a pale yellow color. In some cases the resulting preparation was purified over a size exclusion column to remove salts and unused starting material. Solutions prepared in this way were stored under mildly basic conditions and remained stable on the bench top for several months.

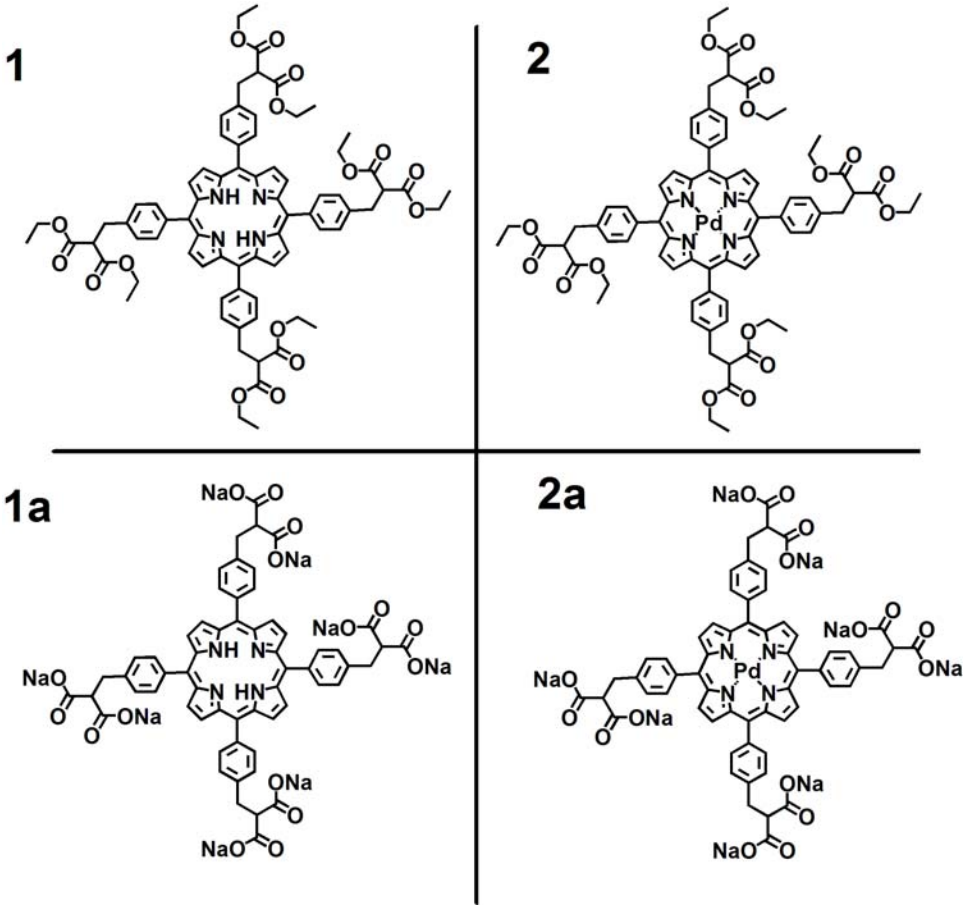

Figure 8. Structures of porphyrin **1**, the octasodium salt of **1** (**1a**), porphyrin **2**, and the octasodium salt of **2** (**2a**).

Cyclic voltammetry (CV) experiments were carried out to elucidate the electrochemical characteristics of the colloids. A typical voltammogram reveals the onset of strong anodic current near 1.1 V vs. Ag/AgCl, indicative of water oxidation. Poising of

the working electrode at sufficiently positive potentials causes the generation of bubbles at the electrode surface in solutions containing the porphyrin–$IrO_x \cdot nH_2O$. Figure 9 shows an overlay of several voltammograms performed in the presence of $IrO_x \cdot nH_2O$ catalysts. The various $IrO_x \cdot nH_2O$ complexes give comparable voltammograms, with strong anodic signals indicative of water oxidation. Comparison with the scan in the absence of any $IrO_x \cdot nH_2O$ clearly shows the signal originates from the presence of the catalyst. It should be emphasized that Figure 9 is not intended as a quantitative comparison between the various $IrO_x \cdot nH_2O$ complexes as the concentration and likely the size of the colloid was different in each case, but rather as a means of demonstrating that the behavior of the porphyrin–$IrO_x \cdot nH_2O$ complexes is similar to that of the carboxylic acid (malonate or citrate) stabilized $IrO_x \cdot nH_2O$ complexes described in the literature.[49, 50]

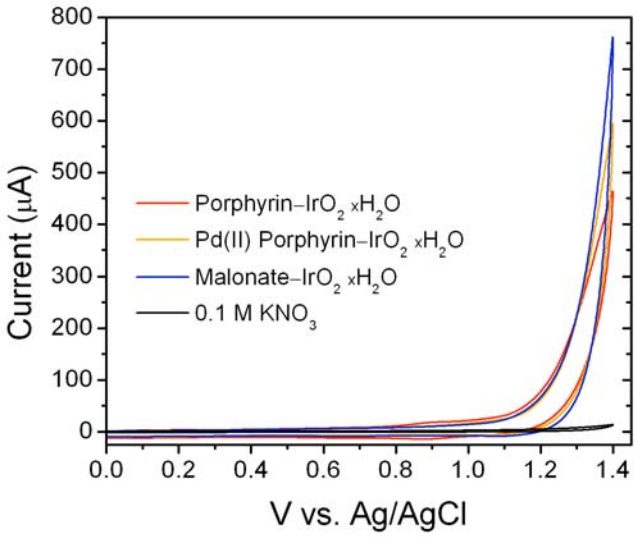

Figure 9. Comparison of cyclic voltammograms taken in solutions containing (red) porphyrin **1a**–$IrO_x \cdot nH_2O$, (orange) porphyrin **2a**–$IrO_x \cdot nH_2O$, (blue) malonate–$IrO_x \cdot nH_2O$ or (black) only supporting electrolyte. All scans taken with a glassy carbon working electrode, at a scan rate of 100 mV/s, with voltages referenced to a Ag/AgCl electrode. The solutions contained $IrO_x \cdot nH_2O$ colloidal catalyst at different concentrations and the currents observed should not be taken as a quantitative comparison of catalytic activity.

In order to demonstrate that the observed catalytic signal corresponds to the oxidation of water to O_2, a Clark electrode was employed to monitor the O_2 concentration in the solution during electrochemical measurements. After purging the cell of O_2 by bubbling with argon, the cell was sealed and the O_2 concentration was monitored while poising the glassy carbon working electrode at various potentials vs. Ag/AgCl (Figure 10). With porphyrin **2a**–$IrO_x{\cdot}nH_2O$ in solution, the O_2 concentration does not increase with time at 0.6 V vs. Ag/AgCl, but does increase at 1.4 V. When the same working electrode is used in a solution containing only supporting electrolyte and no catalyst, no increase in O_2 occurs at either 0.6 or 1.4 V vs. Ag/AgCl. Thus, oxygen is produced only in the presence of the catalyst at a suitable potential.

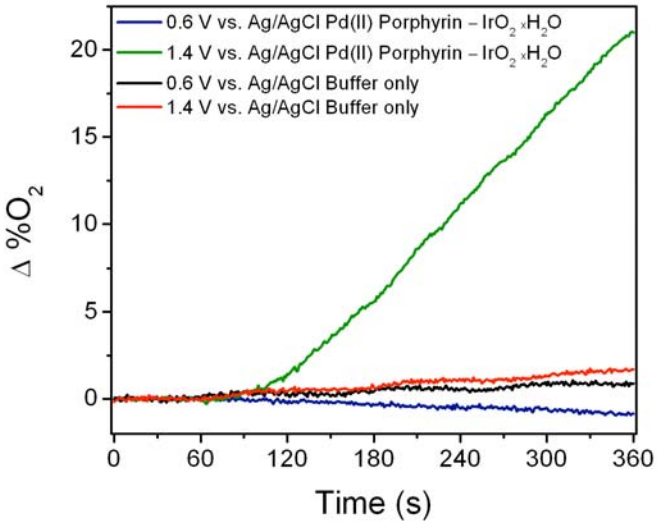

Figure 10. Oxygen concentration relative to air-saturated water measured with a Clark electrode. Green line: porphyrin **2a**–$IrO_x{\cdot}nH_2O$, glassy carbon working electrode poised at 1.4 V vs. Ag/AgCl. Blue line: porphyrin **2a**–$IrO_x{\cdot}nH_2O$, glassy carbon working electrode poised at 0.6 V vs. Ag/AgCl. Black line: buffer only, glassy carbon working

electrode poised at 0.6 V vs. Ag/AgCl. Red line: buffer only, glassy carbon working electrode poised at 1.4 V vs. Ag/AgCl. All measurements taken in H_2O at pH 6.95 with 0.1 M KNO_3 and 0.1 M phosphate buffer. Potential applied starting at t = 60 sec.

As one means of assessing the interaction of the porphyrin dye with the $IrO_x{\cdot}nH_2O$, the porphyrin fluorescence lifetimes in the porphyrin–$IrO_x{\cdot}nH_2O$ complex and with the porphyrin dissolved in a solution containing malonate–$IrO_x{\cdot}nH_2O$ were determined. As shown in Figure 11, the fluorescence lifetime of the free porphyrin **1a** in the presence of malonate–$IrO_x{\cdot}nH_2O$ was 8.79 ns. This lifetime is typical for a free base porphyrin of this general type. The fluorescence lifetime of the same porphyrin complexed with $IrO_x{\cdot}nH_2O$ was quenched, with the major lifetime component of 46.7 ps (70.4%), and minor components with lifetimes of 316.9 ps (18.6 %), 1.81 ns (9.1%), and 7.09 ns (1.9 %). These results suggest that different populations of porphyrin molecules in the material experience different interactions with the $IrO_x{\cdot}nH_2O$. The dominant short fluorescence lifetime component implies a significant interaction between the porphyrin and the $IrO_x{\cdot}nH_2O$ particle. Quenching by energy transfer, electron transfer, enhanced intersystem crossing or some combination of these is possible; the exact mechanism has not been assigned. Fortunately, the porphyrin excited state is not quenched to the point that the quantum yield of electron injection into a nanostructured Ti- or Sn- oxide would be expected to be limited.

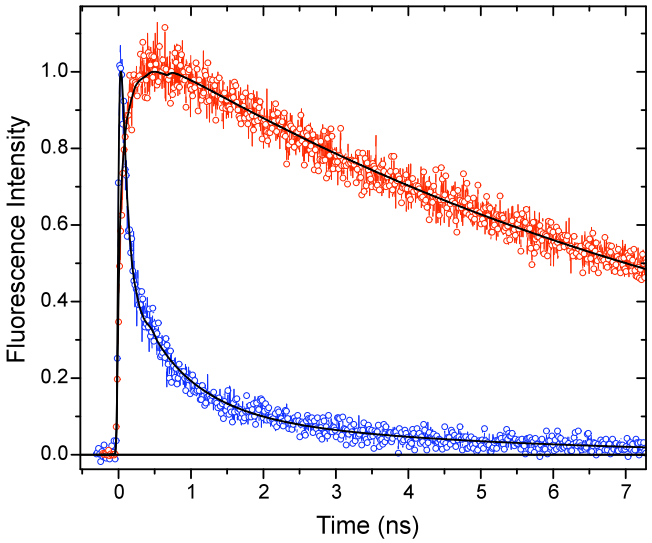

Figure 11. Porphyrin fluorescence lifetime measurements. (Red) porphyrin **1a** in solution with malonate-stabilized $IrO_x{\cdot}nH_2O$, lifetime 8.79 ns. (Blue) porphyrin **1a**–$IrO_x{\cdot}nH_2O$ colloidal particles, major component lifetime 46.7 ps (see text).

In these photoanodes, the driving force for electron transfer from the $IrO_x{\cdot}nH_2O$ catalyst to the sensitizer is provided by the electrochemical potential for the reduction of the porphyrin radical cation. Figure 12 shows cyclic voltammograms of free base porphyrin **1** and its Pd analog **2**. As seen in Table 2, the addition of Pd increases the potential by ~160 mV. Having these two sensitizers available will facilitate mechanistic studies designed to determine the yield-limiting steps in the photo-oxidation of water.

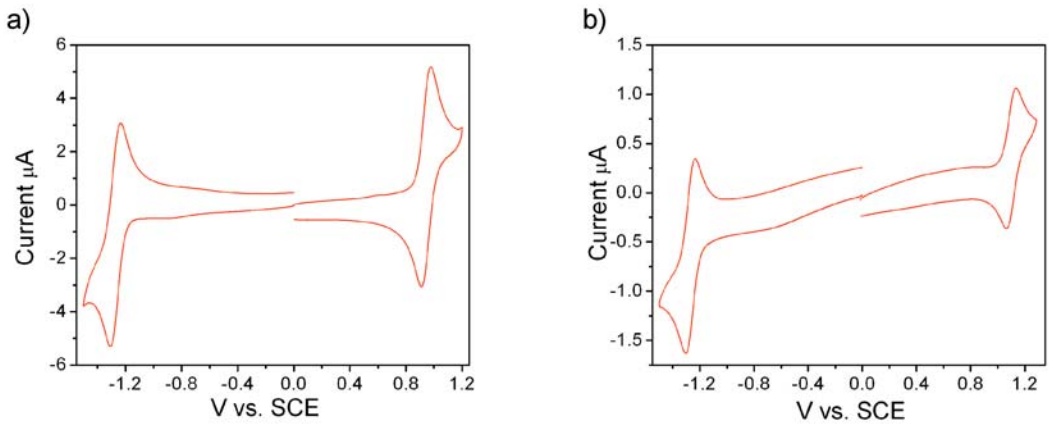

Figure 12. Cyclic Voltammograms of (a) porphyrin **1** and (b) porphyrin **2**. Voltammograms were taken with a platinum working electrode in benzonitrile with 0.1 M tetrabutylammonium hexafluorophosphate, at a scan rate of 100 mV/s.

Table 2. Electrochemical potentials for **1** and **2**.

Porphyrin	1^{st} ox V vs. SCE	ΔE_p 1^{st} ox mV	1^{st} red V vs. SCE	ΔE_p 1^{st} red mV
(**1**)	0.94	67	-1.28	75
(**2**)	1.10	72	-1.28	71

ΔE_p: difference between anodic and cathodic peak potentials of the CV. Scan rate: 100 mV/s.

Conclusion

This chapter reports the use of a high potential, porphyrin-based stabilizer in the formation of $IrO_x{\cdot}nH_2O$ colloidal particles, which have demonstrated catalytic electrochemical water oxidation. The porphyrin was designed to incorporate dicarboxylic acid groups at each of the four *meso* positions as such groups are known to interact favorably with the $IrO_x{\cdot}nH_2O$ surface.[54] This work is a step towards the synthesis of a high potential porphyrin carrying the proper moieties, namely *para*-malonate and phosphonate groups on the porphyrin ring, to allow formation of the catalytic complex and then its subsequent adsorption to a transparent conductive electrode. This construct is

intended for use in the formation of a photoanode of a porphyrin–based analogue of the $Ru(II)(bpy)_3^{2+}$–based water splitting photoelectrochemical (PEC) cells reported previously[53, 59] and work on such a PEC is described in Chapter 5.

Chapter 3: Photochemical Synthesis of a Water Oxidation Catalyst Based on Cobalt Nanostructures

Introduction

(This chapter has been adapted from a previously published report: Wee, T-L., Sherman, B.D., Gust, D., Moore, A.L., Moore, T.A., Liu, Y., Scaiano, J.C. Photochemical synthesis of a water oxidation catalyst based on cobalt nanostructures. *Journal of the American Chemical Society*, **2011**, 133: 16742. I contributed in carrying out electrochemical experiments, detection of oxygen formation, determining turnover estimate, and the design, writing, and editing of this report. See Appendix I for reprint permission details.)

A challenge in the pursuit of a viable artificial photosynthetic system for the storage of solar energy in a useful fuel lies in the discovery of a cost and energy efficient water oxidation catalyst. Many commonly investigated catalysts rely on expensive and scarce elements such as iridium and ruthenium.[45, 60] Recent work has drawn much attention to the use of cobalt, a much more abundant and affordable material, for water oxidation.[61-63] Herein presents a photochemical procedure for the synthesis of nanometric Co_2O_3 with demonstration of its catalytic properties for the oxidation of water to O_2 when in the presence of phosphate ions. Photochemical nanostructure synthesis has the advantage of providing spatial and temporal control; in particular the spectral properties, time dependence, and intensity of the exciting light can be used to control the size and morphology of the metal nanostructures.[64]

Previous work by the Scaiano group at the University of Ottawa demonstrated the photo-induced formation of gold, silver, and copper nanoparticles from the corresponding ions in solution by use of benzoin photoinitiators.[64-68] Ketones are good photosensitizers for nanoparticle synthesis, not because of the energy they can absorb or deliver, but rather because of the reducing free radicals they can generate. Thus, efficient nanoparticle generation requires careful selection of substrates and experimental conditions such that free radical generation occurs with high quantum efficiency and metal ion precursors do not inhibit radical formation. Since many transition metal ions are excellent excited state quenchers, a key consideration for achieving nanoparticle synthesis with short exposure times is minimization of excited state quenching by metal ions.[68] Benzoin-based methods take advantage of the short triplet lifetimes of the radical precursor,[69] and thus allow for fast, one-pot synthesis of metal or metal oxide nanostructures with only mild, non-covalent stabilizers. The resulting weak surface interactions allow easy exchange of surface groups for additional derivatization and/or catalytic applications.

Results and Discussion

Given the recent interest in the use of cobalt as a water oxidation catalyst, I worked in collaboration with Scaiano group to explore the application of a similar aromatic-ketone-based photochemical method for the generation of cobalt oxide nanoparticles and then probed their catalytic viability. The photochemical synthesis of Co_2O_3 nanoparticles (Co_2O_3NP) employed the photoreduction of $CoCl_2$ in dry acetonitrile with Irgacure I-907 (Scheme 1). Upon photoexcitation with UVA light, Irgacure I-907 generates a strongly reducing[70] α-aminoalkyl radical capable of reducing Co^{2+} ions to the

metal in solution. During irradiation, the clear light-blue solution of $CoCl_2$ turns dark green, and black, insoluble paramagnetic particles begin to precipitate. These are presumably clusters of cobalt nanoparticles (CoNP),[71] that later undergo spontaneous oxidation in air to form the desired catalyst, Co_2O_3NP, as black particles.

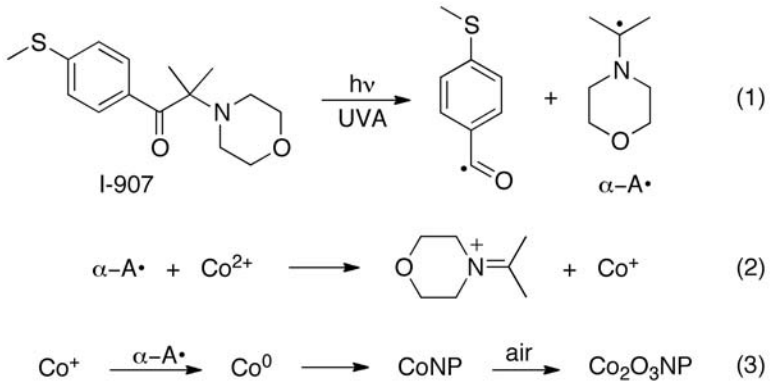

Scheme 1. Mechanism for the formation of CoNP and their spontaneous air oxidation to form Co_2O_3NP.

Characterization of the cobalt oxide material was performed by X-ray diffraction (XRD, Rigaku Ultima IV) and high resolution transmission electron microscopy (HRTEM) for colloidal suspensions and for particles deposited on nanodiamonds, Co_2O_3NP–NCD (*vide infra*). The XRD analysis, as seen in the pattern for Co_2O_3NP–NCD in Figure 13, reveals primarily the presence of Co_2O_3, although less intense bands at $2\Theta=36.3^{o}$ and 42.45^{o} indicate the existence of a small amount of CoO. The lattice spacing of 2.38 Å obtained by HRTEM (JEM-2100F, JEOL) also indicates that the resulting cobalt oxide is primarily Co_2O_3.

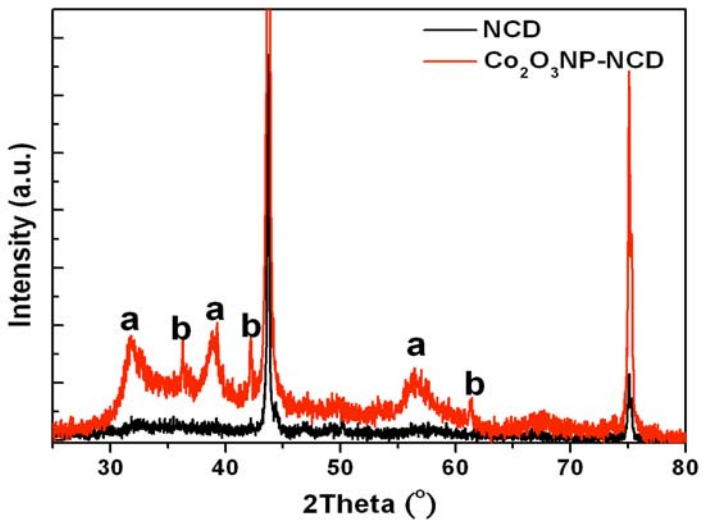

Figure 13. XRD pattern of (black) nanocrystalline diamond (NCD) particles and (red) Co_2O_3NP decorated NCD particles. For the Co_2O_3NP–NCD spectra, peaks marked (a) show the presence of Co_2O_3 while peaks marked (b) indicate the presence of CoO.

To ascertain the catalytic properties of the photochemically prepared Co_2O_3NP for electrochemical oxidation of water to oxygen, films of Co_2O_3NP were prepared on a glassy carbon electrode. To prepare the film a solution containing Co_2O_3NP was sonicated to suspend the particles, a 50 μL aliquot of the solution was pipetted onto the face of the electrode, and the solution was allowed to dry to a film in air. After preparation, the electrode was placed in an aqueous solution containing supporting electrolyte and 0.1 M phosphate buffer at pH 7. Analysis by cyclic voltammetry of these films revealed the onset of large anodic currents upon reaching potentials near 1.1 V vs. AgCl/Ag (Figure 14). The currents obtained from the films greatly exceed those from a glassy carbon electrode lacking any Co_2O_3NP and indicate catalytic water oxidation by the cobalt oxide.

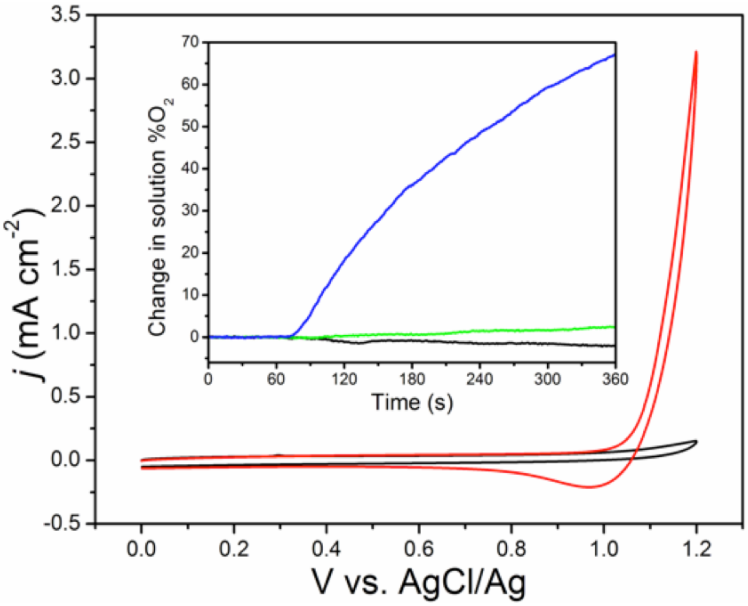

Figure 14. Cyclic voltammogram of (red) Co_2O_3NP particles deposited on a glassy carbon working electrode and (black) a bare polished glassy carbon electrode. All scans taken at 100 mV/s in aqueous solution with 0.1 M KNO_3 and 0.1 M phosphate buffer pH 7. *Inset*: percent dissolved oxygen relative to air-saturated water as measured with a Clark electrode. A carbon felt electrode with photo-deposited Co_2O_3NP was poised at (blue) 1.2 V, (green) 1.0 V, and (black) 0 V with all voltages referenced to AgCl/Ag. Potential was applied at t = 60 s.

Because our interest in forming cobalt nanoparticles centered on the production of a catalytic material for use in photochemical water oxidation, controlling the deposition of the material on a surface is an important aspect for its future utilization. In order to probe the possibility of depositing the material on a surface simultaneously with its synthesis, we included nanocrystalline diamonds (NCD) (MICRO MDA+, Element Six) in the reaction mixture prior to illumination in the hope that they would provide a suitable support for CoNP and Co_2O_3NP growth. Nanocrystalline diamond has drawn much attention in various areas of modern technology due to its unique physical properties such as thermal conductivity and chemical inertness, and its surface affinity for carboxyl and amino groups.[71-74] It has been reported that the surface of the diamond nanoparticles

contains 104 mmol/g surface –COO– groups, which translates to a molecular density of 1.4×10^{14} molecules/cm^2, suggesting that approximately 7% of the total surface carbon atoms exist as carboxyl groups, indicating an exceptionally high affinity for metal nanoparticle nucleation.[20, 72, 74]

The supported cobalt oxide on nanocrystalline diamond was produced in a manner similar to that outlined for Co_2O_3NP.[71] For the preparation of Co_2O_3NP–NCD, a suspension of 350 nm diameter diamond particles was sonicated for 20 min and then added to the deaerated reaction mixture of 1 mM $CoCl_2$ and 2 mM I-907 prior to illumination. During UVA irradiation, it is likely the positive metal ions first randomly adsorb to defect sites on the diamond surface, then interact with the carboxylate groups, which serve as nucleation sites for the growth of CoNP and eventually Co_2O_3 clusters. The TEM images in Figure 15 illustrate the distribution of cobalt oxide nanocrystals on the diamond surface. The surface cobalt oxide particles average in size ~20 nm. After formation, excess cobalt particles, salts, and I-907 were removed by performing centrifugation-redispersion with acetonitrile. The total cobalt content loading of the final diamond-supported cobalt-based catalyst was about 2.5 weight percent. Electrochemical measurements of the Co_2O_3NP–NCD material showed the onset of catalytic current after reaching 1.1 V vs. AgCl/Ag in phosphate-buffered solution.

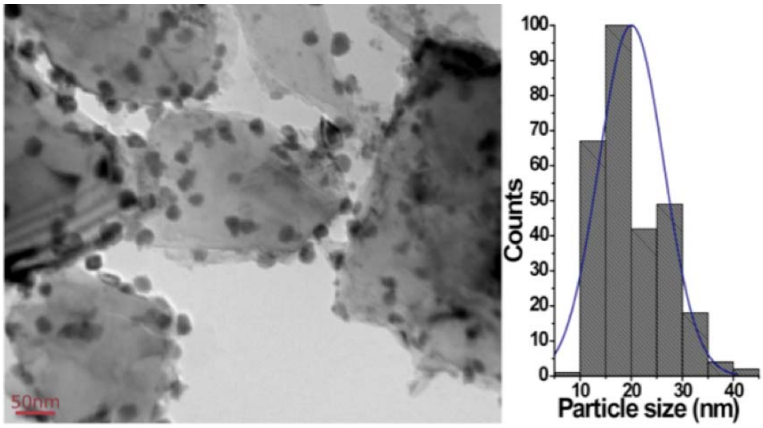

Figure 15. TEM image and particle size distribution of Co_2O_3NP on the NCD support. The smaller, darker clusters of the Co_2O_3NP can be seen on the diamond support. The average cluster size is ~20 nm.

In order to explore the deposition of Co_2O_3 on other materials, we also tested its formation on the surface of conductive carbon felt. It has been reported that the oxidation of the carbon felt by thermal treatment allows for better surface interactions.[75] For this reason, samples of carbon felt were first heated at 400 °C for four hours under air before undergoing the synthesis of the oxide as outlined earlier.

As with the functionalized nanocrystalline diamond particles, regions of cobalt oxide nanoparticles were observed on the surface of the carbon felt after the photochemical synthesis. The difference in the density of Co_2O_3NP deposits on the carbon felt with and without thermal treatment is illustrated by the SEM pictures in Figure 16. The increase in the number of micro-pores and attached cobalt oxide nanoparticles in the case of the heat-treated felt samples is in good accord with an increase in the surface area and the number of C–O and C=O functional groups formed after heating.[20, 72] The attachment of cobalt oxide to the surface may occur via interaction with one or both (chelation) of the oxygen atoms of the carboxylate ion.[20, 76]

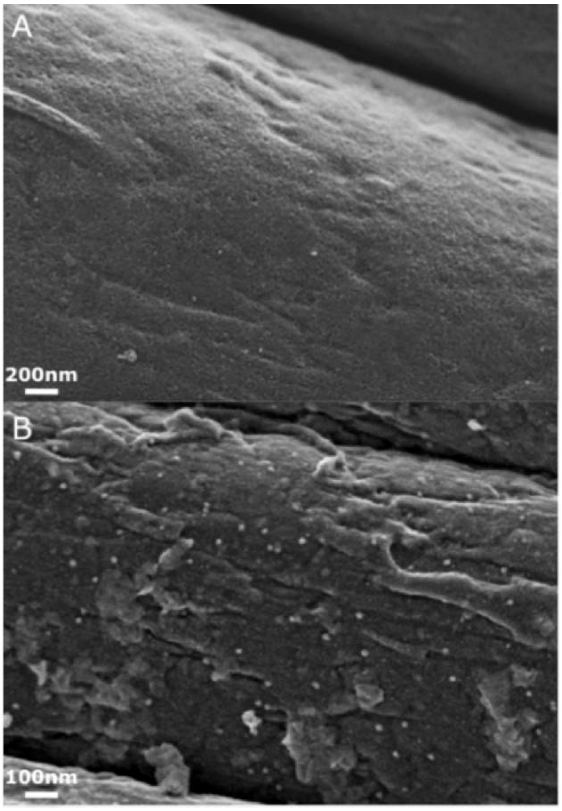

Figure 16. SEM images of cobalt oxide deposits on a carbon felt support: (A) carbon felt not heated prior to cobalt deposition and (B) carbon felt heated to 400 °C for 4 hr and then cooled to room temperature prior to cobalt deposition. The small white dots are the cobalt oxide particles.

Electrochemical analysis of the carbon felt samples in phosphate-containing electrolyte showed strong anodic currents as well as the generation of bubbles at the surface of the felt (Figure 18). A Clark electrode was used to monitor oxygen levels in solution during controlled potential experiments shown in Figure 14 (inset). High currents obtained at potentials positive of 1.1 V vs. AgCl/Ag with the carbon felt electrodes correlated with substantial increases in solution oxygen levels. This demonstrates that Co_2O_3NPs are capable of water oxidation, a key property in terms of the future applications of these materials.

Conclusion

This work reports a new method for preparing Co_2O_3NP photochemically from solutions containing a readily available Co^{2+} precursor and demonstrates that the nanoparticles can be deposited on electrodes. Electrochemical studies establish that electrodes prepared with these nanoparticles behave qualitatively like other recently reported systems involving cobalt[61-63] and indicate that the Faradaic current and corresponding increase in solution oxygen levels results from the four-electron oxidation of water to oxygen upon the application of sufficient overpotential. Experiments to determine the exact mechanism are being pursued. The unique photochemical process for synthesizing these particles provides a well-controlled method for depositing the material on a surface, and we are currently pursuing the development of photoelectrodes using this approach of catalyst deposition. Developing new ways of preparing metal oxide catalysts are important because methods could be found that lead to materials having lower overpotential requirements, or even that perform reversibly - the ultimate Holy Grail of catalysis of the O_2/H_2O half reaction which remains elusive to all efforts.[77]

Experimental Detail and Supplementary Information

Oxygen Measurements

The oxygen measurements shown in Figure 14 were taken with a YSI model 5300 oxygen monitor (Clark electrode). In order to maintain a constant temperature, a temperature jacketed cell was used with 25 ºC water from a temperature bath flowed through the cell during the duration of the experiment. To calibrate the oxygen monitor,

the current measured in air saturated water at 25 ºC was set as 100% O_2; the $\%O_2$ measured during the experiment was then relative to air saturated water. For the measurements, the working solution of the cell contained a carbon felt working electrode, a AgCl/Ag reference electrode (Ag/AgCl/sat. KCl, in a glass tube with vycor tip), a platinum wire counter electrode (in a glass tube, separated by vycor to prevent oxygen reduction in the working solution), and the oxygen monitoring electrode. The working solution consisted of 0.1 M phosphate buffer at pH 7 and 0.1 M KNO_3 supporting electrolyte. The total volume of working solution was ~5 mL and the solution was stirred at a constant rate during the experiment. The cell was sealed with a modified rubber stopper and parafilm to prevent diffusion in or out of the cell. Argon gas was bubbled through the cell to purge oxygen prior to sealing the cell and carrying out the experiments.

Spontaneous Air Oxidation to Form Cobalt Oxide Nanoclusters

The spontaneous oxidation to form the Co oxide happened in solution and occurred rapidly. The metallic cobalt particles formed immediately after the photochemical synthesis were not surface protected and showed extreme sensitivity to O_2, such that any minor exposure to O_2 led to the generation of the Co oxide nanoclusters. Based on the HRTEM d-spacing analysis carried out, only a very small portion of the particles show crystalline structure in the deep center indicating metallic cobalt.

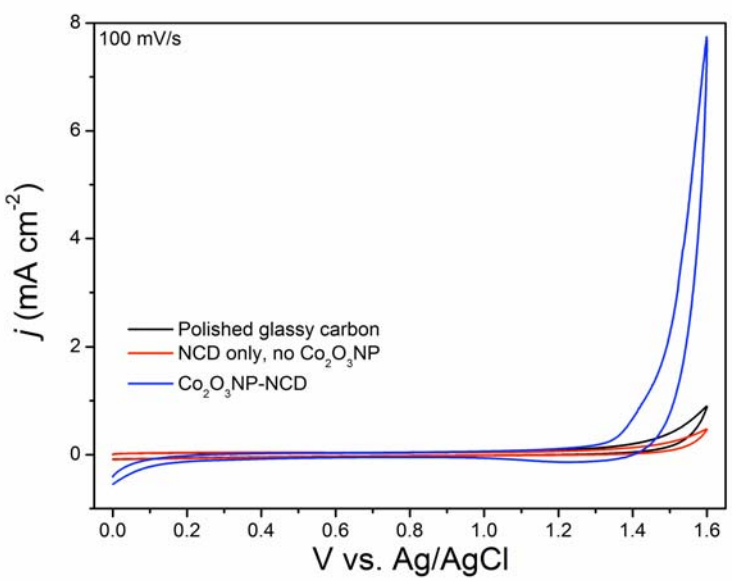

Figure 17. Cyclic voltammograms taken with (black) a blank polished glassy carbon electrode, (red) nanocrystalline diamond (NCD) particles containing no cobalt on a glassy carbon electrode, and (blue) NCD particles containing photochemically deposited cobalt oxide on a glassy carbon electrode. Voltammograms were taken at a scan rate of 100 mV/s in aqueous solution containing 0.1 M phosphate buffer at pH 7 and 0.1 M KNO_3 as supporting electrolyte.

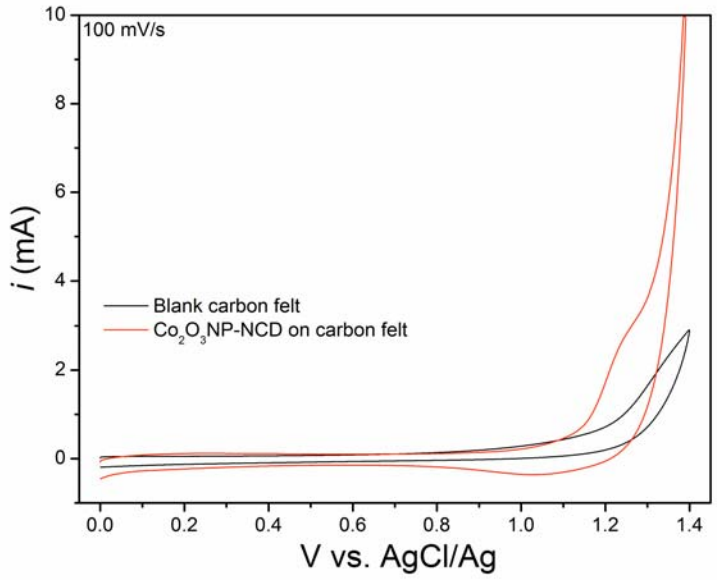

Figure 18. Cyclic voltammograms of (black) a carbon felt electrode without any cobalt oxide and (red) a carbon felt electrode containing nanocrystalline diamond particles with photochemically deposited cobalt oxide. Voltammograms were taken at a scan rate of 100 mV/s in aqueous solution with 0.1 M phosphate buffer at pH 7 and 0.1 M KNO_3 as supporting electrolyte.

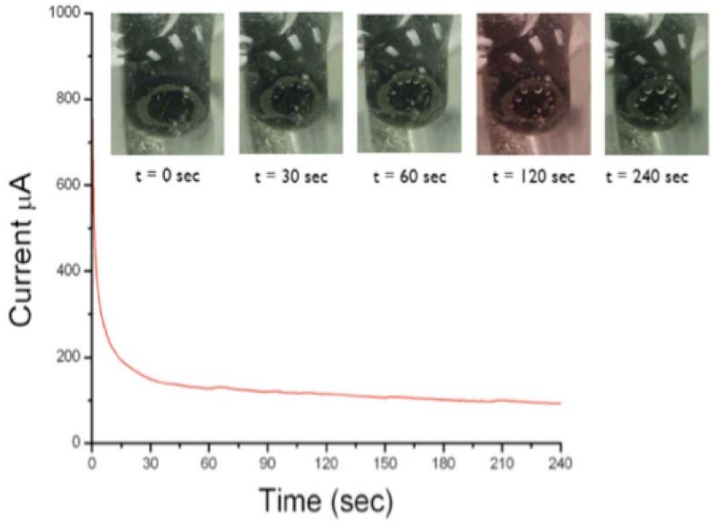

Figure 19. Plot showing a current trace during a controlled potential experiment at 1.6 V vs. AgCl/Ag for a glassy carbon electrode containing a surface layer of Co_2O_3NP–NCD particles. The experiment was carried out in an aqueous solution containing 0.1 M phosphate buffer at pH 7 and 0.1 M KNO_3 as supporting electrolyte. The inset picture sequence shows the state of the glassy carbon electrode at the indicated time points during the experiment. No bubbles are present initially on the electrode surface but begin to form within 30 seconds of applying potential to the electrode. The generation of bubbles on the electrode surface was assumed to be the result of O_2 production by the catalytic oxidation of water by the Co_2O_3NP–NCD particles and this was verified by later experiments using a Clark electrode.

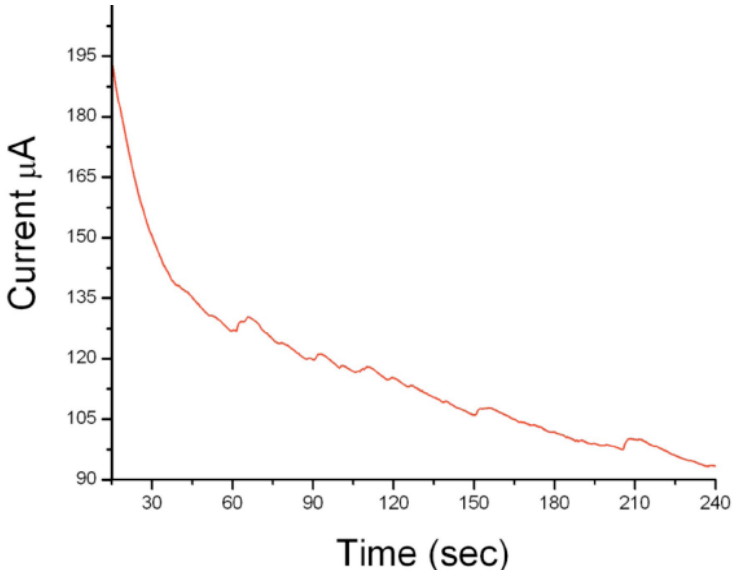

Figure 20. Zoomed view of the current trace shown in Figure 19. The jaggedness of the current trace likely arises from the formation and movement of bubbles on the electrode surface.

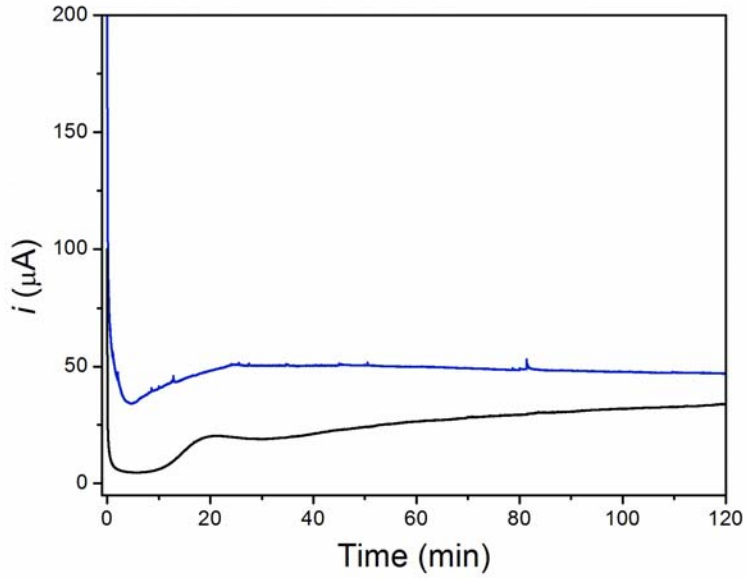

Figure 21. Current traces under an applied potential of 1.5 V vs. AgCl/Ag for (black) a polished glassy carbon electrode and (blue) a glassy carbon electrode with a deposited film of Co_2O_3NP. The surface area of the electrode was the same for both traces. The solution contained 0.1 phosphate buffer at pH 7 and 0.1 M KNO_3. The presence of Co_2O_3NP leads to sustained higher currents over the 2 h duration of the experiment. Consistent with Figure 20, the spikes in the blue trace coincided with bubble activity on the electrode surface.

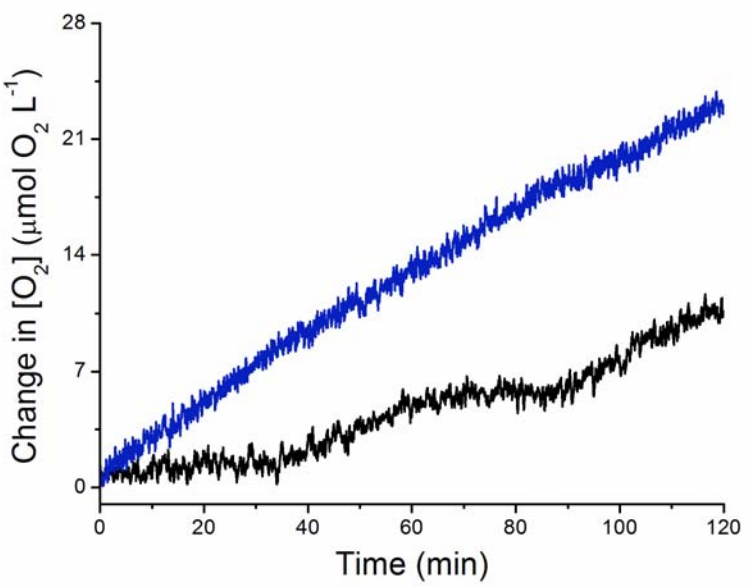

Figure 22. Oxygen concentration in solution measured by an Ocean Optics NeoFox-FOXY oxygen probe system during the 2 h controlled potential experiments shown in Figure 21. The black trace shows the change in oxygen concentration during application of 1.5 V vs. Ag/AgCl applied to a polished glassy carbon electrode and the blue trace shows that for 1.5 V vs. Ag/AgCl applied a glassy carbon electrode with a coating of Co_2O_3NP.

The sustained higher currents seen in Figure 21 in the presence of Co_2O_3NP corresponded with a greater increase in solution O_2 during the course of the experiment. These results are consistent with Co_2O_3NP catalyzing the oxidation of water to O_2 for ≥ 2 h.

Preliminary Estimation of Turnover Frequency for Co_2O_3NP

To provide a preliminary estimate for the lower limit of the turnover frequency, a linear best-fit equation was fitted to the 2 h O_2 trace in the presence of Co_2O_3NP shown in Figure 22 which indicated an O_2 production rate of 0.00298 μmol O_2 L^{-1} s^{-1} during the experiment. In addition, we used a CH Instruments 460 electrochemical quartz crystal

microbalance to measure the mass of a film of Co_2O_3NP deposited in the same manner as that used in Figure 22, finding 0.72 μg Co_2O_3 (4.2 nmol Co_2O_3) in the film. Taking into account the volume of water in the cell used in Figure 22 (30 mL), the amount of Co_2O_3NP deposited on the glassy carbon electrode (4.2 nmol), and the observed rate of O_2 generation, gives a turnover frequency of 0.021 mol O_2 per mol Co_2O_3 per second. The net increase in O_2 observed during the course of the experiment (~750 nmol O_2) exceeds by 100 fold the amount of O_2 contained in the mass of catalyst loaded (6.3 nmol O_2).

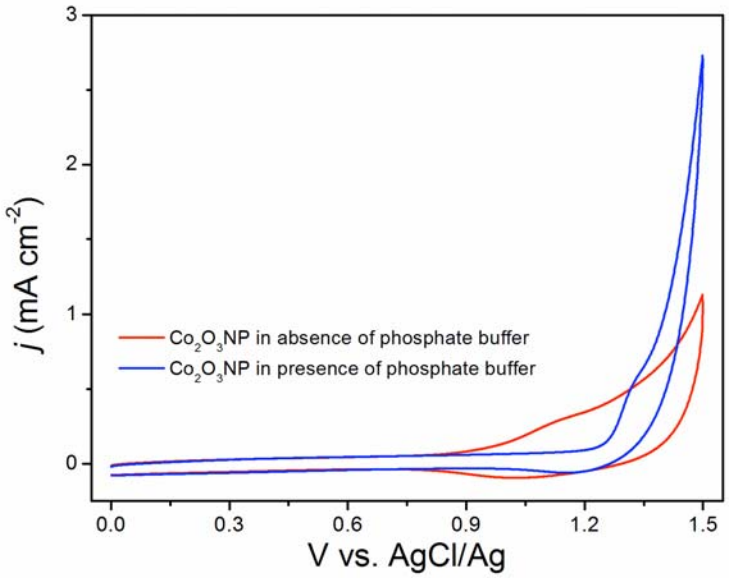

Figure 23. Comparative voltammograms showing the effect of the presence of phosphate buffer on the activity of the Co_2O_3NP. A sharp catalytic signal results in presence of phosphate buffer (blue) whereas in the absence of phosphate (red) a more broad anodic wave results. The voltammograms shown were run using a deposited film of Co_2O_3NP on a glassy carbon working electrode in water with (red) 0.1 M KNO_3 or (blue) 0.1 M KNO_3 and 0.1 M phosphate buffer at pH 7.

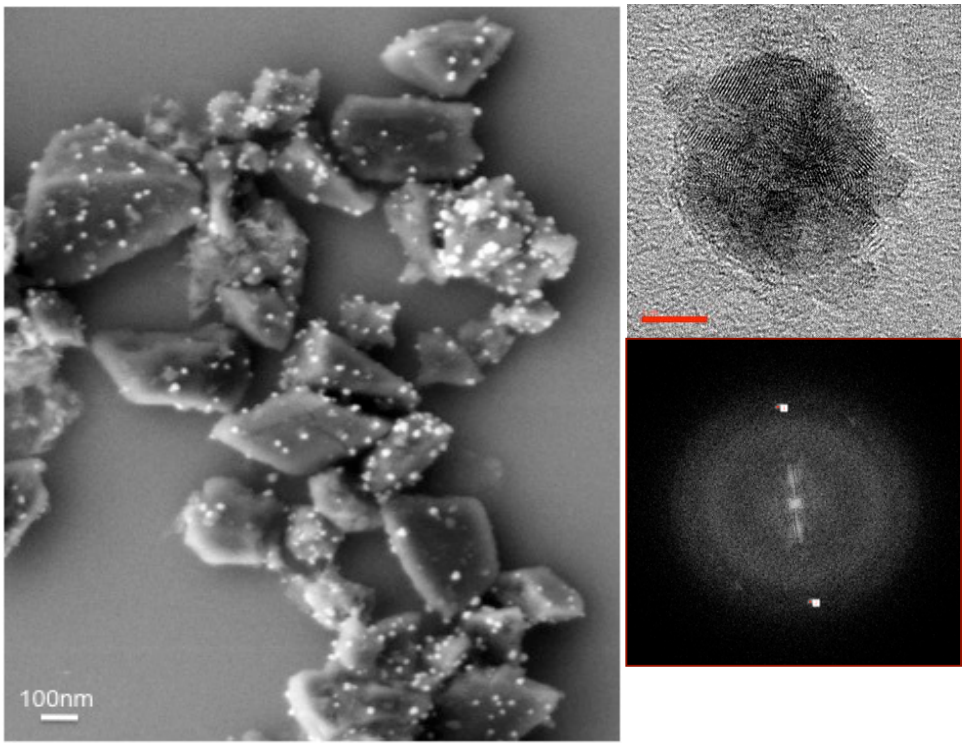

Figure 24. (left) SEM image of Co_2O_3NP-NCD and (right, top) HR-TEM image of a Co oxide nanoparticle (scale bar is 5 nm). Together these show that the Co oxide nanoparticle consists of domains of different orientations and large number of defects along the domain boundaries, possibly as a result of merging of smaller nanocrystal seeds during the particle growth. The bottom right image is the fast Fourier transform of one crystalline domain of the HR-TEM image shown top right.

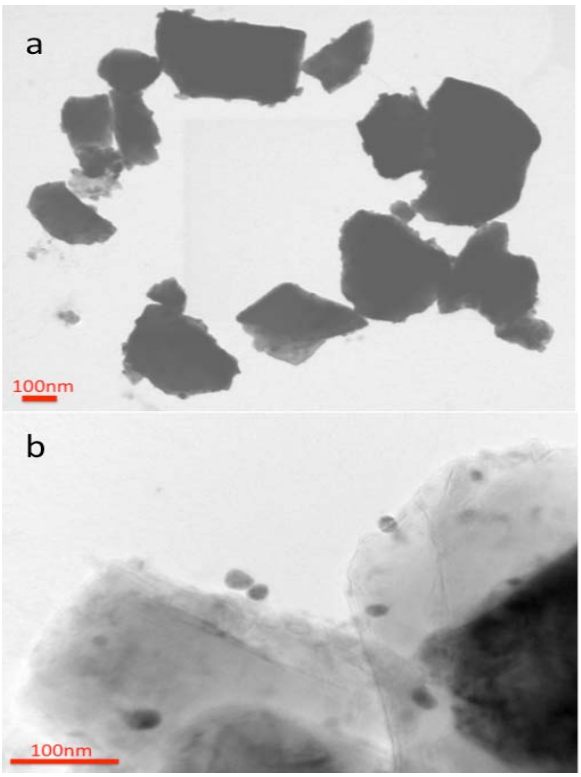

Figure 25. SEM image (a) and TEM image (b) of Co_2O_3NP–NCDs after catalytic water oxidation experiments. Together these images show that there are Co_2O_3NPs on the NCD surface after the water oxidation process.

Chapter 4: Synthesis and Characterization of Silicon Phthalocyanines Bearing Axial Phenoxyl Groups for Attachment to Semiconducting Metal Oxides

Introduction

(This chapter has been adapted from a previously published report: Bergkamp, J.J., Sherman, B.D., Marino-Ochoa, E., Palacios, R.E., Cosa, G., Moore, T.A., Gust, D., Moore, A.L. Synthesis and characterization of silicon phthalocyanines bearing axial phenoxyl groups for attachment to semiconducting metal oxides. *Journal of Porphyrins and Phthalocyanines*, **2011**, 15: 943. I contributed electrochemical experiments and in the design, writing, and editing of this report. See Appendix I for reprint permission details.)

Developing artificial photosynthetic technologies for converting solar energy to transportable, energy-dense fuels would be a major step towards meeting future human energy demands while also mitigating our impact on the environment.[78] Using the energy of sunlight to drive the conversion of water to oxygen and hydrogen offers an attractive means of converting and storing solar energy. A device capable of splitting water with light requires several key components including catalysts for the oxidation of water and production of hydrogen and photochemical systems capable of generating and stabilizing charge separated states. The latter are of interest in this work and require light absorbing materials judiciously chosen for their absorbance and redox properties.

To date, artificial photosynthetic systems have suffered from high cost, a need for rare materials, and/or low overall efficiencies for generating hydrogen.[53, 79] An appealing route for incorporating potentially lower cost materials that enable fine-tuning of light absorption and the generation of long-lived, stable charged separated states lies in the use

of organic dyes. Organic chromophores such as porphyrins, chlorins, perylenes, and phthalocyanines that bear carboxylic acid or phosphonate groups share many properties with natural dyes involved in photosynthesis and have demonstrated their viability in capturing and converting solar energy to electricity in dye sensitized solar cells as shown in recent reviews (ref 80 and 83).[80-83]

Producing an efficient device for the generation of hydrogen from water with the only energy input coming from light will likely require a design utilizing two light absorbing photosystems, each of which harvests distinct regions of the solar spectrum.[84, 85] When considering organic dyes for use in such a system, careful balance of the absorption and redox properties of the dyes plays an integral role in the design; in a dual-threshold cell, the dyes must interact with separate parts of the spectrum while still accessing similar solar flux, and the excited state energies and redox properties of each must provide sufficient driving force for its electrochemical reaction of interest.

Phthalocyanines are good candidates for use in dual-threshold photoelectrochemical cells because of their high extinction coefficients, good chemical stability, and, most importantly, excited state potentials that provide sufficient driving force for the cathodic reduction of protons to hydrogen. Octabutoxy silicon phthalocyanines are of particular interest because of their absorbance in the visible and near-IR and the opportunity to functionalize them by covalent attachment to the axial position of the central silicon atom.

Herein we explore axially modifying silicon phthalocyanines to introduce desirable functional groups for integrating these dyes into photoelectrochemical cells. Axial substitution is an attractive feature for multiple synthetic reasons: (i) having

substituents above and below the macrocycle prevents aggregation and increases the solubility of these compounds,[86] (ii) the ligands can be highly functionalized, and (iii) silicon phthalocyanines are robust under harsh chemical treatments. Axially coordinated ruthenium phthalocyanines have been shown to photo-inject electrons into TiO_2,[87] demonstrating that the electronic coupling of axially linked phthalocyanines is suitable for electron injection into semiconducting metal oxides. It is also worth noting that the use of non-peripheral octabutoxy groups helps to reduce aggregation,[88] bathochromically shifts the absorbance considerably relative to peripherally substituted analogues,[89] and shifts the redox values to more negative potentials.[90]

This chapter reports synthetic strategies for functionalizing far red absorbing octabutoxy silicon phthalocyanines for adsorption to metal oxide semiconductors. This methodology introduces phenyl or biphenyl axial substituents with ethyl carboxylic ester or diethyl phosphonate functional groups via a phenoxy linkage. Upon deprotection, the resulting carboxylate or phosphonate moieties would serve as anchoring groups to metal oxide semiconductors.

Results and Discussion

Joyner *et al.*[91] first reported a protocol for displacing axial hydroxy ligands on silicon phthalocyanines using molten phenol and a few drops of pyridine. Herein reports an adaption of this method that yields mono-phenoxy silicon phthalocyanines. Silicon insertion into the free-base octabutoxy phthalocyanine involved first using trichlorosilane in a mixture of dichloromethane and tributylamine to yield the dichloride silicon phthalocyanine in situ (Scheme 2). Displacement of the chloride ligands in a mixture of

water and triethylamine produced the dihydroxy silicon phthalocyanine **1** with a 53% yield (Scheme 2). Monosilation of **1** took place in refluxing toluene with one equivalent of chlorotriethylsilane to yield **2** with a 76% yield (Scheme 2). The reaction was monitored via thin layer chromatography and quenched upon formation of traces of the disilylated silicon phthalocyanine. Diethyl 4'-hydroxybiphenyl-4-ylphosphonate **3** was prepared by an adaptation of the Hirao palladium-catalyzed cross-coupling reaction[92] in dry dimethylformamide using tris(dibenzylideneacetone)-dipalladium(0) as the catalyst, diisopropylethylamine as the base, and 1,1'-bis(diphenylphosphino)ferrocene as the ligand (Scheme 3). The linkage of the corresponding phenols in compounds **4**, **5**, and **6** (Scheme 3 and 4) was done in pyridine at 55°C for 48–60 hours. In all cases, two column-chromatography steps were necessary for purification of **4**, **5**, and **6** due to the tendency for streaking on silica gel.

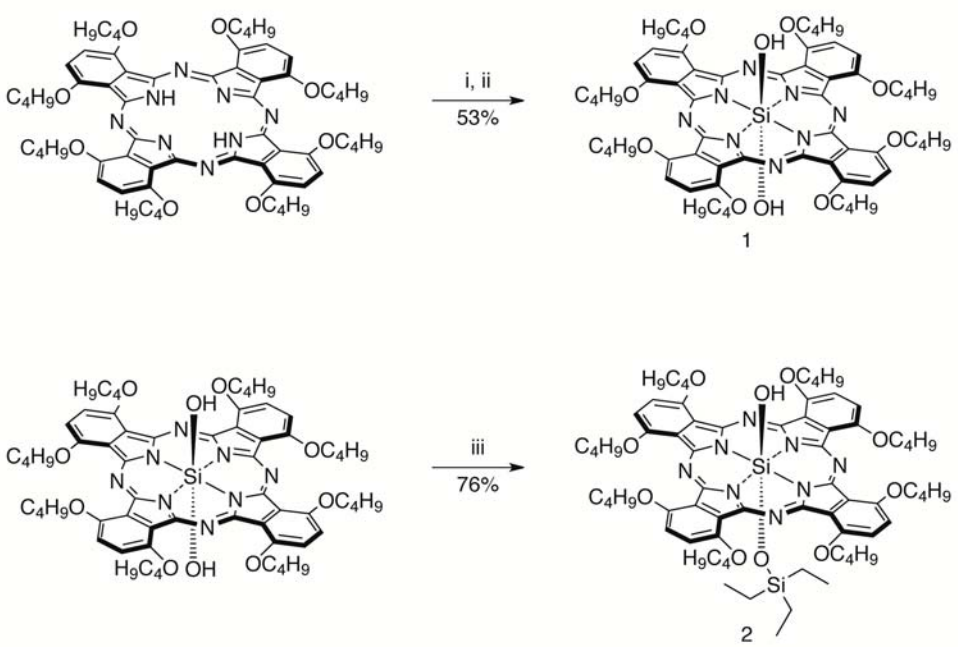

Scheme 2. Synthesis of Phthalocyanine **1** and **2**. Reaction conditions: i) $HSiCl_3$, TBA, CH_2Cl_2, rt, 18 h; ii) TEA, H_2O, rt, 3 h; iii) $HSiEt_3$, toluene, pyridine, reflux, 45 min.

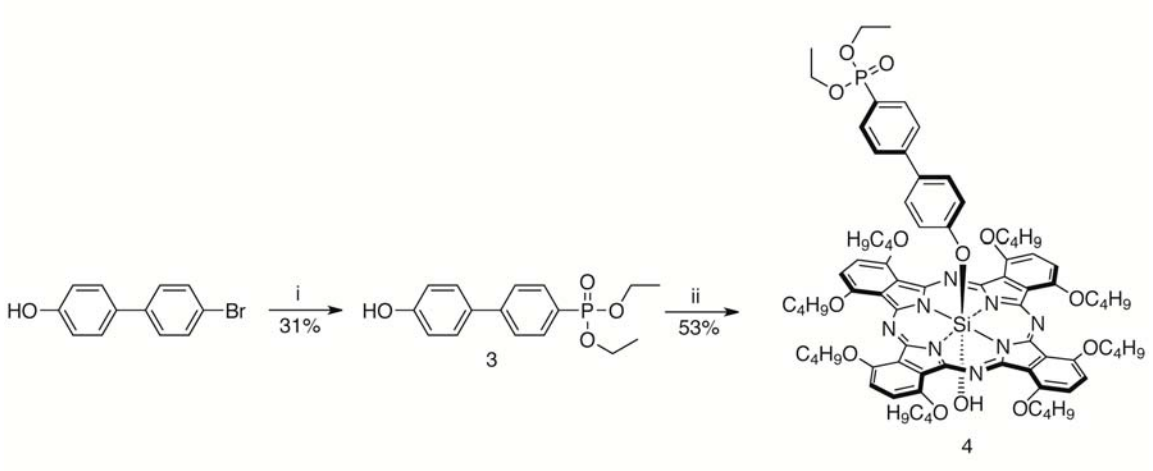

Scheme 3. Synthesis of Phthalocyanine **4**. Reaction conditions: i) dimethylformamide, diethylphosphite, N,N-diisopropylethylamine, 1,1'-bis(diphenylphosphino)ferrocene, tris(dibenzylidene-acetone)dipalladium(0), 110 ^{o}C, 24 h; ii) **1,** pyridine, 55 ^{o}C, 48 h.

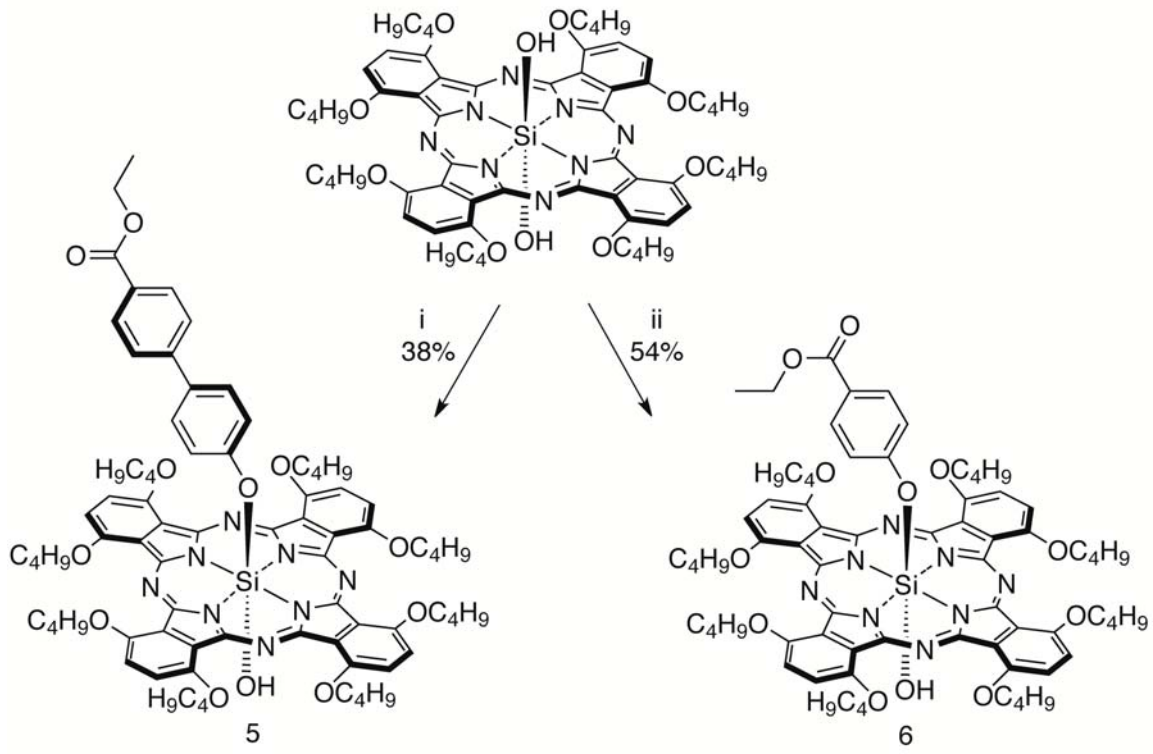

Scheme 4. Synthesis of Phthalocyanines **5** and **6**. Reaction conditions: i) ethyl 4'-hydroxybiphenyl-4-carboxylate, pyridine, 55 ^{o}C, 48 h; ii) ethyl 4-hydroxybenzoate, pyridine, 55 ^{o}C, 60 h.

We started with a non-peripheral octaalkoxy substituted phthalocyanine for several reasons. Most importantly, alkoxy substituents aid in increasing the solubility of the phthalocyanine in organic solvents while inhibiting the tendency for aggregation.[86, 88, 93] Octabutoxy groups have been chosen located at the non-peripheral positions (1,4,8,11,15,18,22,25) because substitution at these sites has been shown to induce a greater shift on the absorption spectrum to longer wavelengths than octabutoxy groups on the peripheral positions.[89]

We have inserted silicon into the macrocycle of the phthalocyanine as this allows for axial covalent modification. Typically, axial modification of silicon phthalocyanines proceeds from the dichloride silicon phthalocyanine. However, we found the dichloride species to be unstable, possibly due to greater lability of the chloride ligands resulting from electron donating effects and increased solubility from the presence of the octabutoxy groups at the non-peripheral positions of the phthalocyanine macrocycle. Others have achieved the phenoxy linkage,[90, 94-96] but started from the non-substituted dichloride silicon phthalocyanine and allowed it to react with a strong base such as sodium hydride. This method starts from the dihydroxy species, as demonstrated by Joyner and others,[91, 97] but requires only mild reaction conditions (such as lower temperatures), limited amounts of starting phenol, and allows use of phenols with chemically sensitive functional groups. Furthermore, it allows for the synthetic control necessary to produce the mono axial phenoxy substituted silicon phthalocyanine.

Initially the goal was to synthesize mono-phenoxy phthalocyanine with the opposite face protected with a triethylsiloxyl group. This strategy resulted in two issues of concern: (i) the longest wavelength Q band was blue shifted in **2** with respect to **1** by 5

nm (Figure 26), and, (ii) after the phenoxy group is coupled, the stability of the triethylsiloxyl group decreases as evidenced by difficulties in isolation. Therefore we decided to leave the second axial hydroxyl group unprotected.

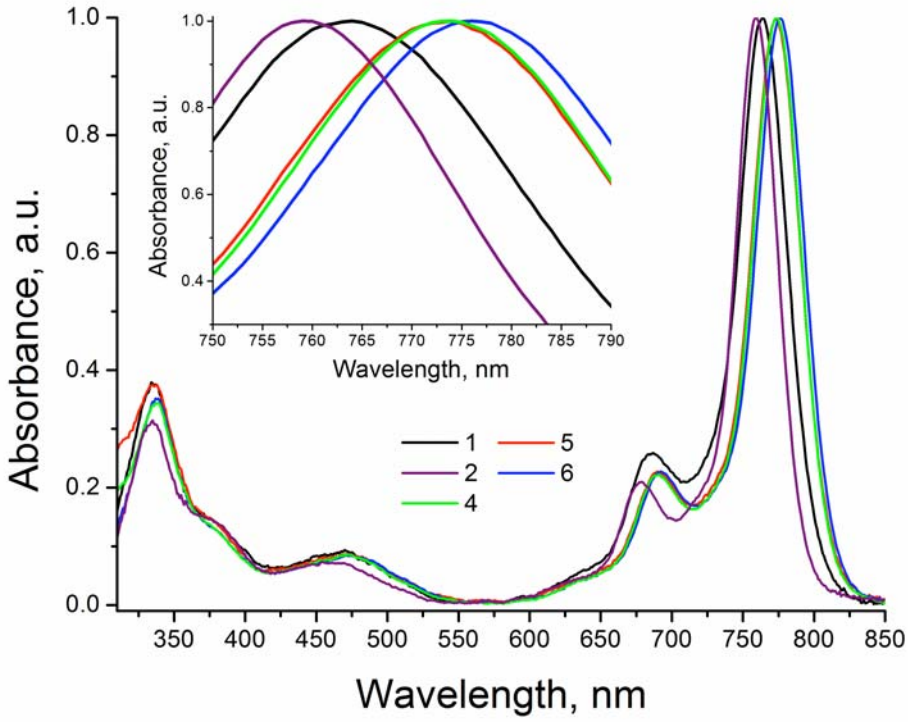

Figure 26. Normalized absorption spectra for phthalocyanine derivatives **1**, **2**, **4**, **5**, and **6**. Inset shows a zoomed expanded view of the longest wavelength Q band of each derivative. Spectra were taken in distilled dichloromethane.

Ultraviolet-visible spectral analysis reveals a shift to longer wavelengths of the lowest energy Q band upon phenoxy displacement of the hydroxide. Compound **6** shows a bathochromic shift of 12 nm with respect to **1** (Figure 26) with the reddest Q band occurring at 776 nm. Both **4** and **5** have the biphenyl linker and, although they bear different functional groups at the para position, their absorption properties are similar in that the reddest Q band is slightly shifted to shorter wavelengths in comparison with **6** but longer wavelengths with respect to **1** (Figure 26). The absorbance of the lowest energy Q

bands of **4** and **5** indicates that the ethyl carboxylic ester or diethyl phosphonate groups do not have as strong an influence on the absorbance presumably due to decoupling caused by the biphenyl linker.

The 1H NMR spectra of **4**, **5**, and **6** show an upfield shift of the aromatic protons that are axial to the plane of the phthalocyanine. Aromatic protons ortho to the phenoxy linkage show signals at ~2.9 ppm, consistent with results from other studies.[98] The magnitude of the up field shift decreases as the location of the proton moves further away from the center of the phthalocyanine macrocycle which is in accordance with the literature.[95, 96, 99, 100] The OH signal in the 1H NMR of **2**, **4**, **5**, and **6** could not be detected; Cook *et al.* have observed similar effects.[101] Each target compound was characterized by matrix assisted laser desorption/ionization-time of flight (MALDI-TOF) mass spectroscopy. Trans-2-[3-(4-tert-butylphenyl)-2-methyl-2-propenylidene]-malononitrile was found to be the best matrix and free-base 1,4,8,11,15,18,22,25-octabutoxyphthalocyanine was used as an internal reference.

An important aspect of evaluating dyes for photoelectrochemical applications lies in the determination of their redox properties in order to ensure that they can carry out the photo-initiated electrochemical processes of interest. This work targets silicon phthalocyanines to drive the cathodic reduction of protons to hydrogen; their excited state redox potentials must be sufficiently negative to carry out this process, which at pH 7 occurs at -0.65 V vs. SCE. Determining the potentials for the oxidation and reduction of a dye, coupled with its absorption characteristics, allows approximation of its excited state redox potentials. Cyclic voltammetry experiments on the silicon phthalocyanine dyes synthesized for this work showed them to be good candidates for driving proton

reduction. Figure 27 features cyclic voltammograms for compounds **4**, **5**, and **6**; the redox potentials for these compounds and dye **1** are listed in Table 3. Overall, the identity of the axial ligand to the silicon had minimal influence on the redox potentials of the phthalocyanines. For example, the potentials for the first oxidation differed by only 10 mV across the series. These molecules showed reversible first and second oxidations with anodic and cathodic peak separations (ΔEp) near 60 mV, while the first reductions gave greater peak separations, implying more quasi-reversible character.

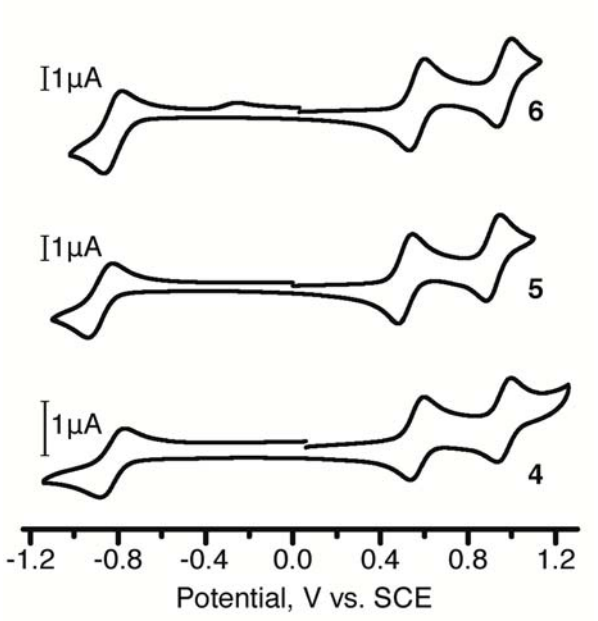

Figure 27. Cyclic voltammograms for compounds **4**, **5**, and **6**. All scans shown were taken at 100 mV/s in dichloromethane with 0.1 M tetrabutylammonium hexafluorophosphate. The identity of the phenoxy ligand had only subtle influence on the redox potentials as evidenced by the similarity of each scan.

Table 3. Redox values for the compounds **1**, **4**, **5**, and **6**. Potentials given are in reference to a saturated calomel electrode (SCE). Peak separation (ΔE_p) of the anodic and cathodic scans is given for each process.

Compound	Ox(1), (ΔE_p)	Ox(2), (ΔE_p)	Red(1), (ΔE_p)
1	0.55 V, (64 mV)	0.95 V, (67 mV)	-0.84 V, (80 mV)
4	0.55 V, (63 mV)	0.96 V, (64 mV)	-0.90 V, (98 mV)
5	0.54 V, (64 mV)	0.96 V, (64 mV)	-0.83 V, (98 mV)
6	0.54 V, (68 mV)	0.93 V, (67 mV)	-0.82 V, (80 mV)

With an eye toward the eventual testing of these dyes in a dual-threshold photoelectrochemical water splitting cell, the potential of the first oxidation takes greater importance. With midpoint potentials near 0.55 V vs. SCE and longest-wavelength photon absorption of ~1.6 eV, these dyes will have adequate excited state energies to sensitize TiO_2 or other semiconducting metal oxides with a more negative conduction band.[102] Future work will aim at investigating the efficiency of electron injection into metal oxide semiconductors by these axial functionalized phthalocyanines, and their ability to drive the formation of hydrogen in a photoelectrochemical cell.

Conclusion

The synthesis of silicon octabutoxy phthalocyanines bearing axial ethyl carboxylic esters and diethylphosphonate groups via a phenoxy linkage can be accomplished in a few synthetic steps, from a variety of phenols, and under mild conditions. Additionally, this approach allows for isolation of the mono axial functionalized phenoxy phthalocyanines. Strongly red absorbing phthalocyanines are

good candidates for dual-threshold solar cells and the use of non-peripheral octabutoxy groups as well as the substitution of phenols on the axial position of silicon phthalocyanines, as demonstrated with **4**, **5**, and **6**, helps to further shift their absorption to the near infrared. Furthermore, the phenoxy substituted phthalocyanines prepared in this study demonstrated potentials for the first oxidation near 0.55 V vs. SCE, making them good candidates for photosensitizing low-potential conduction band metal oxide semiconductors. The ability to use low-potential conduction band materials will provide more driving force for the generation of hydrogen from water. By incorporating phenoxy ligands with functional groups that can anchor to metal oxide semiconductors, this work shows progress toward the use of these dyes in dual-threshold photoelectrochemical cells designed to carry out overall water splitting with sunlight. Moreover the ability to bind a variety of phenoxy derivatives in the axial position can be exploited to control the macrocycle to metal-oxide electronic coupling and consequently the efficiency of the sensitization process. The synthetic strategy presented offers a route to obtaining phthalocyanines with axial groups for anchoring to semiconducting metal oxides from the readily obtainable bis-hydroxy octabutoxy silicon phthalocyanines.

Experimental

Electrochemistry

All electrochemical experiments were carried out with a CH Instruments 760D potentiostat. All samples were analyzed in a closed glass cell under an argon atmosphere with a three electrode setup. A working platinum disc electrode was used in concert with

a platinum mesh counter electrode and a silver quasi-reference electrode. The potential of the silver quasi-reference electrode was calibrated versus the ferrocenium/ferrocene (Fc^+/Fc) couple at the conclusion of each series of experiments with the Fc^+/Fc couple taken as 0.45 V vs. SCE. Distilled dichloromethane was used as the working solvent along with 0.1 M tetrabutylammonium hexafluorophosphate as supporting electrolyte, which was doubly recrystallized from ethanol and dried under reduced pressure with heat prior to use.

Materials

Dichloromethane used for synthesis and electrochemistry was refluxed over calcium hydride followed by distillation and storage over activated 4 Å molecular sieves. Pyridine and dimethylformamide were dried over activated 4 Å molecular sieves. Tributylamine was passed though activated alumina and stored overnight over activated 4 Å molecular sieves. Toluene for synthesis was distilled from phosphorus pentoxide and stored over activated 4 Å molecular sieves. Toluene, ethyl acetate and hexane used for column chromatography were distilled. Triethylamine was purchased from Alfa Aesar and used without further purification. Trichlorosilane, 1,4,8,11,15,18,22,25-octabutoxy-29H,31H-phthalocyanine, chlorotriethylsilane, diethylphosphite, diisopropylethylamine (Hünig's base), 1,1’-bis(diphenylphosphino)ferrocene, 4'-bromo-(1,1'-biphenyl)-4-ol, ethyl 4'-hydroxybiphenyl-4-carboxylate, ethyl 4-hydroxybenzoate, and tris(dibenzylideneacetone)dipalladium(0) were purchased from Sigma-Aldrich and used without further purification. Tetrabutylammonium hexafluorophosphate was also purchased from Sigma-Aldrich. Thin layer chromatography plates (250 micron), both

fluorescent and non-fluorescent, were purchased from Analtech, Inc. Silica gel (SiliaFlash F60 40-63 μm) used for column chromatography was purchased from SILICYCLE.

General

1H NMR spectra were recorded on a 400 MHz Varian Liquid-State spectrometer. NMR samples were dissolved in deuteriochloroform with 0.03% tetramethylsilane as an internal reference. Mass spectra were obtained on an Applied Biosystems Voyager-DE STR matrix-assisted laser desorption/ionization time-of-flight spectrometer (MALDI-TOF). The matrix used for all mass spectra samples was trans-2-[3-(4-tert-butylphenyl)-2-methyl-2-propenylidene]malononitrile. Ultraviolet-visible ground state absorption spectra were measured using a Shimadzu UV2100U spectrophotometer. All ultraviolet-visible samples were dissolved in distilled dichloromethane.

Synthesis

Dihydroxy-1,4,8,11,15,18,22,25-octabutoxyphthalocyaninatosilicon(IV) (**1**). A portion of 1,4,8,11,15,18,22,25-octabutoxy-29H,31H-phthalocyanine (1.1 g, 1.0 mmol) was dissolved in dry dichloromethane (240 mL) and dry tributylamine (24 mL). The solution was degassed with argon for 10 min, followed by addition of trichlorosilane (2.4 mL, 23.8 mmol) and allowed to stir at room temperature for 18 h under argon. Triethylamine (80 mL) was added carefully, followed by H_2O (40 mL) and the mixture was allowed to stir at room temperature for an additional 3 h. To neutralize the amines, aqueous HCl (12 M, 58 mL) was added until the solution was acidic, and the solution was

allowed to stir for an additional 1 h. The mixture was filtered and the solid was washed with dichloromethane (500 mL). The mother liquor was separated and the organic layer was washed twice with HCl (1 M, 100 mL) followed by 3 washes with H_2O. The organic layer was dried over sodium sulfate and the solvent was removed under reduced pressure. Column chromatography was done using silica gel with ethyl acetate/toluene (50:50) as eluent, which afforded a green solid. Yield 615 mg (53%), 1H NMR (400 MHz; $CDCl_3$; 0.03% Me_4Si): δH, ppm -2.54 (2H, bs, –OH), 1.08 (24H, t, $–CH_2–CH_2–CH_2–CH_3$, J = 7.2 Hz), 1.66 (16H, sex., $–CH_2–CH_2–CH_2–CH_3$, J = 7.6 Hz), 2.20 (16H, p, $–CH_2–CH_2–CH_2–CH_3$, J = 7.6 Hz), 4.87 (16H, t, $–CH_2–CH_2–CH_2–CH_3$, J = 7.2 Hz), 7.64 (8H, s, PcH). UV-vis (CH_2Cl_2): λmax, nm 334, 470, 687, 764. MS (MALDI-TOF): m/z calcd. for $C_{64}H_{82}N_8O_{10}Si$ 1150.59, obsd. 1150.59.

Triethylsilylhydroxy-1,4,8,11,15,18,22,25-octabutoxyphthalocyaninatosilicon(IV) (**2**). A portion of (**1**) (70 mg, 0.06 mmol) was dissolved in dry toluene (30 mL) and dry pyridine (4 mL) and degassed for 15 min. Chlorotriethylsilane (10.2 μL, 0.06 mmol) was added and the solution was allowed to reflux for 45 min. Once formation of bis-triethylsilyl phthalocyanine was observed (monitored by TLC), the solvent was removed under reduced pressure and column chromatography was done using silica gel with toluene/ethyl acetate (65:35) as eluent, which afforded a green solid. Yield 59 mg (76%), 1H NMR (400 MHz; $CDCl_3$; 0.03% Me_4Si): δH, ppm -2.14 (6H, q, $–CH_2–CH_3$, J = 8 Hz), -0.98 (9H, t, $–CH_2–CH_3$, J = 8 Hz), 1.04 (24H, t, $–CH_2–CH_2–CH_2–CH_3$, J = 7.6 Hz), 1.63 (16H, sex., $–CH_2–CH_2–CH_2–CH_3$, J = 7.6 Hz), 2.15 (16H, p, $–CH_2–CH_2–CH_2–CH_3$,

J = 7.2 Hz), 4.88 (16H, m, $–CH_2–CH_2–CH_2–CH_3$), 7.65 (8H, s, PcH). UV-vis (CH_2Cl_2): λmax, nm 335, 465, 679, 759. MS (MALDI-TOF): m/z calcd. for $C_{70}H_{96}N_8O_{10}Si_2$ 1264.68, obsd. 1264.68.

Diethyl (4'-hydroxy-[1,1'-biphenyl]-4-yl)phosphonate (**3**). A portion of 4'-bromo-(1,1'-biphenyl)-4-ol (996 mg, 4.0 mmol) was dissolved in dimethylformamide (15 mL) and the solution was degassed with argon for 15 min. To that solution was added diethylphosphite (662 mg, 4.8 mmol), diisopropylethylamine (Hünig's base) (0.9 mL), 1,1'-bis(diphenylphosphino)ferrocene (24.3 mg, 0.044 mmol) and tris(dibenzylideneacetone)dipalladium(0) (26.9 mg, 0.040 mmol, 1 mol%). The solution was allowed to stir at 110 ^oC for 24 h under argon. The solvent was removed under reduced pressure and the red-yellow oil dissolved in ethyl acetate, H_2O was added (50 mL) and the aqueous layer was washed 4 times with ethyl acetate followed by 1 wash with brine, dried over magnesium sulfate, and concentrated. Column chromatography was done using silica gel with ethyl acetate/hexane (70:30) as eluent, which afforded a yellow solid. Yield 378 mg (31%), 1H NMR (400 MHz; $CDCl_3$; 0.03% Me_4Si): δH, ppm 1.35 (6H, t, $–CH_2–CH_3$, J = 7.2 Hz), 4.15 (4H, m, $–CH_2–CH_3$), 6.87 (2H, d, Ar–phenoxy, J = 8.8 Hz), 7.47 (2H, d, Ar–phenoxy, J = 8.8 Hz), 7.63 (2H, m, Ar–phosphonate), 7.84 (2H, m, Ar–phosphonate). MS (MALDI-TOF): m/z calcd. for $C_{16}H_{19}O_4P$ 306.10, obsd. 307.11.

4'-(Diethoxyphosphoryl)biphenyl-4-olatehydroxy-1,4,8,11,15,18,22,25-octabutoxyphthalocyaninatosilicon(IV) (**4**). A portion of (**1**) (31 mg, 0.027 mmol) was dissolved in dry pyridine (10 mL), to this solution was added diethyl 4'-hydroxybiphenyl-4-ylphosphonate (**3**) (82 mg, 0.27 mmol) and the solution was degassed with argon for 10

min. The solution was allowed to stir at 55 ^{o}C for 48 h under argon. The solvent was removed under reduced pressure and two column chromatography steps were needed to purify the desired product using silica gel. The first chromatography step was with toluene/ethyl acetate (60:40) and the second with toluene/ethyl acetate (75:25) to afford a green solid. Yield 20 mg (53%), 1H NMR (400 MHz; $CDCl_3$; 0.03% Me_4Si): δH, ppm 1.04, (24H, t, $–CH_2–CH_2–CH_2–CH_3$, J = 7.6 Hz), 1.22 (6H, t, $–CH_2–CH_3$, J = 6.8 Hz), 1.62 (16H, sex., $–CH_2–CH_2–CH_2–CH–$, J = 7.6 Hz), 2.14 (16H, p, $–CH_2–CH_2–CH_2–CH_3$, J = 8 Hz), 2.94 (2H, d, Ar–phenoxy, J = 8.8 Hz), 3.98 (4H, m, $–CH_2–CH_3$), 4.82 (16H, m, $–CH_2–CH_2–CH_2–CH_3$), 5.96 (2H, d, Ar–phenoxy, J = 8.8 Hz), 6.87 (2H, m, Ar–phosphonate), 7.49 (2H, m, Ar–phosphonate) 7.65 (8H, s, PcH). UV-vis (CH_2Cl_2): λmax, nm 339, 472, 691, 774. MS (MALDI-TOF): m/z calcd. for $C_{80}H_{99}N_8O_{13}PSi$ 1438.68, obsd. 1438.69 and 1133.59 (M-phenoxy).

4'-(Ethoxycarbonyl)biphenyl-4-olatehydroxy-1,4,8,11,15,18,22,25-octabutoxyphthalocyaninatosilicon(IV) (**5**). A portion of (**1**) (48 mg, 0.042 mmol) was dissolved in dry pyridine (10 mL) and the solution degassed for 10 min. To this solution was added ethyl 4'-hydroxybiphenyl-4-carboxylate (51 mg, 0.21 mmol) and allowed to stir at 55 ^{o}C for 48 h under argon. The solvent was removed under reduced pressure and column chromatography was done using silica gel with toluene/ethyl acetate (65:35) and then a second column chromatography step using toluene/ethyl acetate (75:25) as eluent, which afforded a green solid. Yield 22 mg (38%), 1H NMR (400 MHz; CDCl3; 0.03% Me4Si): δH, ppm 1.04, (24H, t, $–CH_2–CH_2–CH_2–CH_3$, J = 7.6 Hz), 1.31 (3H, t, $–CH_2–CH_3$, J = 7.2 Hz), 1.62 (16H, sex., $–CH_2–CH_2–CH_2–CH_3$, J = 7.6 Hz), 2.14 (16H, p, $–CH_2–CH_2–CH_2–CH_3$, J = 8 Hz), 2.93 (2H, d, Ar–phenoxy, J = 8.8 Hz), 4.27 (2H, q, –

CH_2–CH_3, J = 7.2 Hz), 4.81 (16H, m, –CH_2–CH_2–CH_2–CH_3), 5.98 (2H, d, Ar–phenoxy, J = 8.4 Hz), 6.83 (2H, d, Ar–benzoate, J = 8.8 Hz), 7.64 (8H, s, PcH), 7.72 (2H, d, Ar–benzoate, J = 8.4 Hz). UV-vis (CH_2Cl_2): λmax, nm 338, 471, 690, 774. MS (MALDI-TOF): m/z calcd. for $C_{79}H_{94}N_8O_{12}Si$ 1374.68, obsd. 1374.68.

4-(Ethoxycarbonyl)phenolatehydroxy-1,4,8,11,15,18,22,25-octabutoxyphthalocyaninatosilicon(IV) (**6**). A portion of (**1**) (48 mg, 0.042 mmol) was dissolved in dry pyridine (12 mL) and the solution degassed for 10 min. To this solution was added ethyl 4-hydroxybenzoate (35 mg, 0.21 mmol) and was allowed to stir at 55 ^oC for 60 h under argon. The solvent was removed under reduced pressure and column chromatography was done using silica gel with toluene/ethyl acetate (70:30) as solvent. A second column chromatography step using toluene/ethyl acetate (80:20) as eluent, afforded a green solid. Yield 29 mg (54%), 1H NMR (400 MHz; $CDCl_3$; 0.03% Me_4Si): δH, ppm 1.07, (24H, t, –CH_2–CH_2–CH_2–CH_3, J = 7.2 Hz), 1.34 (3H, t, –CH_2–CH_3, J = 7.2 Hz), 1.64 (16H, sex., –CH_2–CH_2–CH_2–CH_3, J = 7.2 Hz), 2.16 (16H, p, –CH_2–CH_2–CH_2–CH_3, J = 8 Hz), 2.87 (2H, d, Ar–phenoxy, J = 8.8 Hz), 3.91 (2H, q, –CH_2–CH_3, J = 6.8 Hz), 4.80 (16H, m, –CH_2–CH_2–CH_2–CH_3), 6.41 (2H, d, Ar–phenoxy, J = 8.8 Hz), 7.65 (8H, s, PcH). UV-vis (CH_2Cl_2): λmax, nm 337, 471, 692, 776. MS (MALDI-TOF): m/z calcd. for $C_{73}H_{90}N_8O_{12}Si$ 1298.64, obsd. 1298.65 and 1133.58 (M-phenoxy).

Chapter 5: Development and Study of Tandem Photoelectrochemical Solar Cells

Introduction

The oxidation of water to O_2 and H^+, the half reaction shown in Equation 1, presents both a thermodynamic (requiring 1.23 V vs. NHE) and kinetic (4 electron process) challenge. Carrying out light driven water splitting, with water oxidation occurring at the anode and hydrogen formation at the cathode, with a single light absorbing junction hampers the efficiency of the system due to limited availability of energetically competent photons in the solar spectrum.[103] A more advantageous design incorporates two light absorbing junctions, similar to oxygenic photosynthesis, whereby the energy of two photons per electron serves to drive the overall process. As such, a tandem photoelectrochemical cell provides a greater theoretical maximum efficiency[84, 103] and presents a more viable platform for developing artificial photosynthetic systems than those utilizing a single light absorbing junction.

Equation 1:

$$O_2 + 4H^+ + 4e^- \rightleftharpoons 2H_2O$$

Figure 28 provides a basic cartoon of the tandem photocell design I have pursued during my graduate study. This scheme incorporates two photoactive and two dark electrodes. This design consists of a photoelectrochemical cell (PEC) (i.e., capable of using light energy to break/form chemical bonds) linked in series with a dye sensitized photovoltaic cell (PV) (i.e., capable of converting solar energy to electricity). Photoanode

electrode 1 adsorbs bluer light and serves as the site of water oxidation (conversion of H_2O to O_2 and H^+ with the liberation of 4 electrons per oxygen molecule formed). The second photoanode in the system, electrode 3, adsorbs redder light and carries out the oxidation of the mediator. This design situates the photoelectrodes in parallel and perpendicular to the path of illumination; as such, the bluer absorbing junction must be positioned in front of the redder absorbing junction. If reversed, the red absorbing junction would obscure the blue junction (as any wavelength shorter than the red absorbing threshold would be absorbed) and compromise the generation of photocurrent. In this configuration, the photovoltaic cell serves to provide added voltage to drive the formation of the fuel, H_2 as shown here, produced at the dark cathode, electrode 4. Electrode 2 serves as the cathode of the photovoltaic cell and facilitates the regeneration of the mediator from its oxidized form by electrons originating at electrode 1. This design isolates the electrolyte solutions of either photocell, the two only connected by electric contacts. As shown, a proton permeable membrane allows proton flux between the photoanode and cathode of the PEC and prevents the product of either electrode from migrating across the cell and short circuiting the system. I would like to note, this describes one possible organization of this design, the one I have worked on; there is no inherent reason more red photons could not drive water oxidation and more blue photons drive the production of fuel or a semiconductor based PV cell be used in place of a dye sensitized solar cell (DSSC).

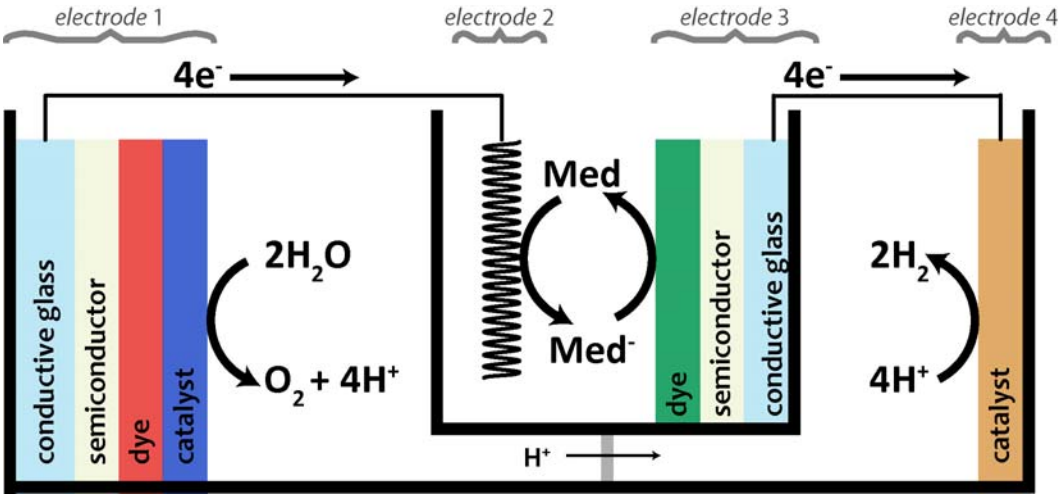

Figure 28. Schematic showing the design of a tandem photoelectrochemical cell for the production of solar-fuel from water with light.

Results and discussion

Dye Structures

An integral effort on this project has centered on the design and synthesis of several chromophore molecules with tailored chemical, spectroscopic, and electrochemical properties. Table 4 provides an overview of several dyes used in this study. As detailed in chapter three, non-peripheral octaalkoxy phthalocyanines have been targeted for use at the red adsorbing junction based on their low potential (sufficiently reducing) excited states and absorption in the far-red to near-infrared portion of the spectrum. Ruthenium(II) tris(bipyridyl) ($Ru(bpy)_3^{2+}$) complexes and porphyrins have been selected for use at the water oxidizing junction both for their high redox potentials (sufficiently oxidizing) and absorption in the solar spectrum from the near-UV to red portion of the visible region.

Table 4. Molecular structures for dyes used in this study.

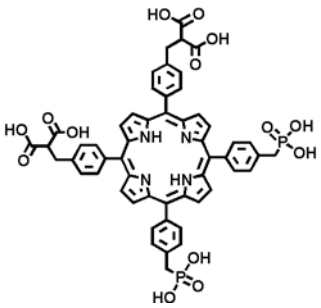	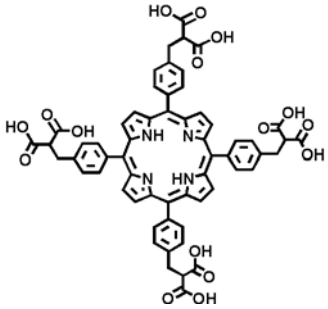	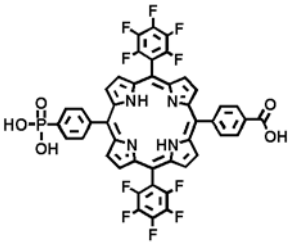
Porphyrin **1**	Porphyrin **2**	Porphyrin **3**
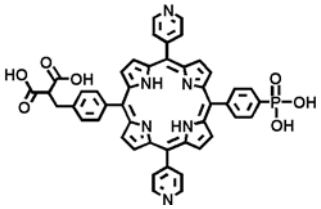	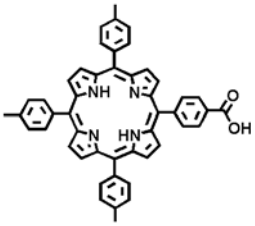	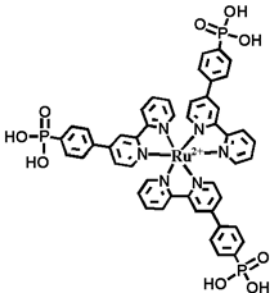
Porphyrin **4**	Porphyrin **5**	Tris-(bipyridyl)Ru(II) complex **6**
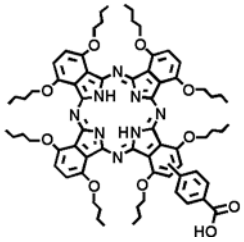	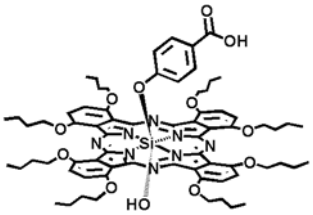	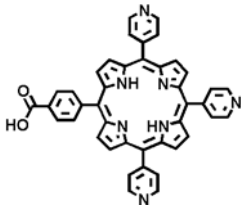
Phthalocyanine **7**	Phthalocyanine **8**	Porphyrin **9**

Both the $Ru(bpy)_3^{2+}$ and porphyrin structures share specific structural characteristics. Phosphonate or carboxyl functional groups have been selected for

anchoring the dyes to the metal oxide semiconductor surface. Phosphonate groups have been shown to provide robust attachment to TiO_2 and SnO_2 in water, important to preventing desorption of the dye from the surface.[104] Carboxyl groups more readily hydrolyze from the metal oxide surface in aqueous electrolyte, however have still proven effective, particularly in conjunction with hydrophobic dyes.[105] The presence of a malonic functional group allows for attachment of the dye to the $IrO_x \cdot nH_2O$ surface.[54] The incorporation of electron withdrawing groups, such as pentafluorophenyl and pyridyl groups, raises the potential of the dyes, making them more powerful oxidants and therefore providing more overpotential to drive water oxidation.[42]

Spectral Considerations

Balancing spectral coverage is of fundamental importance to maximizing the efficiency of a tandem junction device. Since the traverse of an electron through the system involves the absorption of both a bluer and a redder photon, partition of the solar spectrum allowing for equal photon flux at either junction will allow for the greatest possible efficiency for solar water splitting. Considering oxygenic photosynthesis, the absorption of nearly isoenergetic photons at each photosystem imparts a major limitation on the overall efficiency when considering the conversion of available sunlight to chemical fuel.[85] Figure 29 provides a graphical portrayal of this limitation; if considering an inverted Z-scheme superimposed on the solar spectrum as plotted in photon flux, one finds that nearly half the energetically useful spectrum (from 700 to 1100 nm)[84] untapped by natural photosynthesis. The design of an artificial system should bifurcate the spectrum with different absorption thresholds at each junction to both balance photon

flux and maximize the collection of energetically useful photons to thereby allow for improved efficiency in the system, as shown in the rightmost pane of Figure 29.

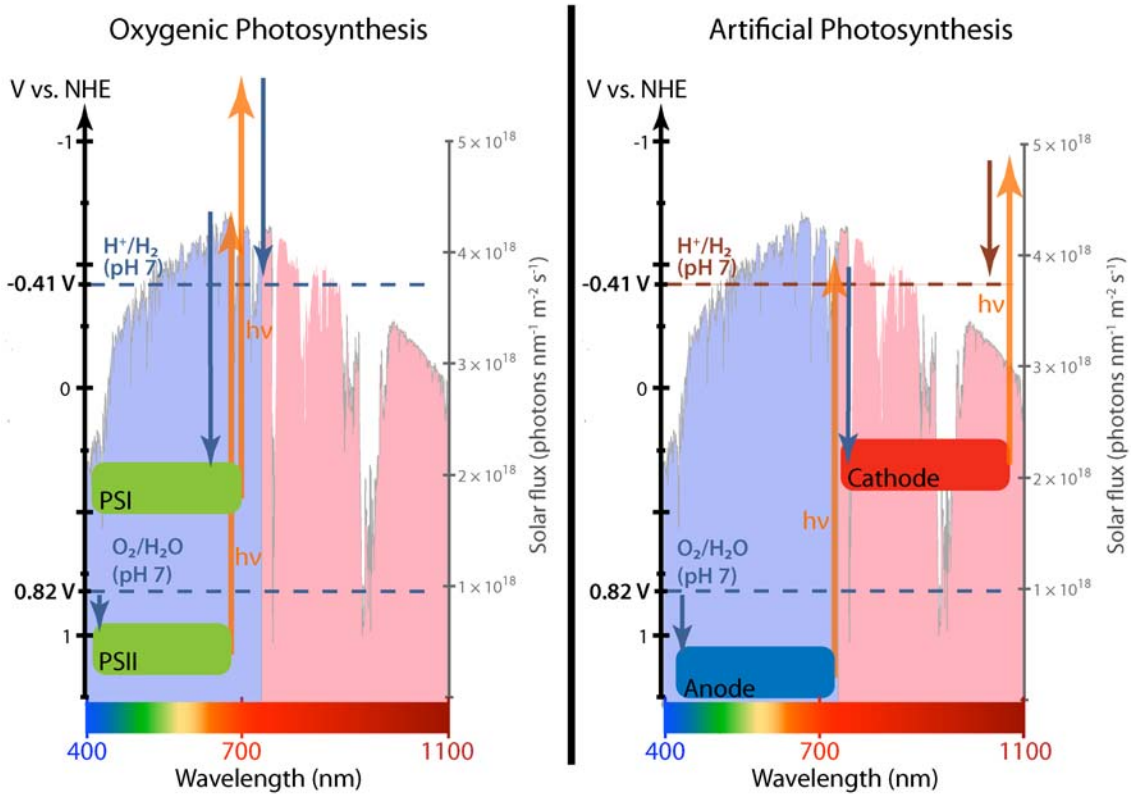

Figure 29. Comparison of absorption thresholds, excited state energetics, potential for water oxidation and hydrogen formation, and coverage of the solar spectrum for oxygenic photosynthesis and an ideal artificial photosynthetic system. Downward pointed arrows indicate electron transfer and upward pointed arrows reflect the energy increase of an electron by photoexcitation (length of upward arrows correspond to the energy of the absorbed photon).

In thermodynamic terms, conversion of water to O_2 and H_2 requires 1.23 V, however, additional potential must be supplied to satisfy overpotential requirements of the catalysts and drive the net formation of products at a desired rate. Assuming the need for ~ 0.8 V of overpotential, and taking into account other losses that limit solar energy

conversion, results in ideal thresholds of ~ 1.7 eV (~ 750 nm) for the bluer absorbing junction and ~ 1.1 eV (~ 1100 nm) for the redder junction.[84] Unfortunately the dyes currently under study do not allow for such spectral division, however, the concert of porphyrin and phthalocyanine dyes does allow for coverage from 400 to 900 nm as seen in Figure 30.

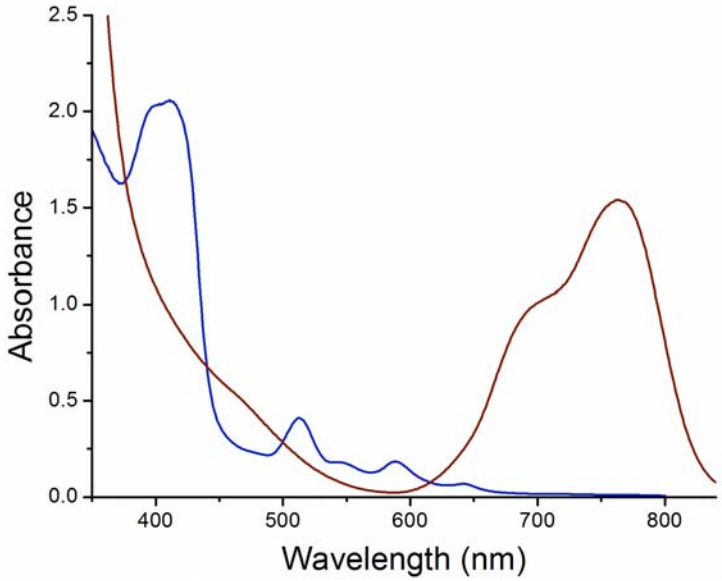

Figure 30. Absorbance overlay of (blue) Porphyrin **3** adsorbed to an FTO–SnO_2 electrode and (red) Phthalocyanine **7** adsorbed to an FTO–TiO_2 electrode.

Semiconductor Considerations

In addition to balancing the spectral division between the two junctions, the choice of semiconductor employed at each photoelectrode plays an important role in positioning the energy levels in the system. As mentioned earlier, the oxidation of water requires substantial overpotential and therefore necessitates the use of high potential

dyes. Chemical modification of a porphyrin with electron withdrawing groups makes the dye a more powerful oxidant but, concomitantly, makes it a weaker reductant. This affects the ability of the dye to sensitize the metal oxide semiconductor, depending on the type of semiconductor used. For instance, the conduction band of TiO_2, the most commonly used metal oxide in dye sensitized type photoelectrodes, begins at around -0.5 V vs. NHE at pH 7.[106] In order to sensitize TiO_2, the dye excited state must possess a more negative potential than the conduction band. Due to this, high potential porphyrins typically perform poorly in systems utilizing TiO_2 and therefore a more positive conduction band material is better suited for the water oxidizing photoanode. Cassiterite tin oxide (SnO_2) has a conduction band 400 mV more positive than anatase TiO_2 making it an ideal candidate for use at the O_2 forming junction.[107] A key design feature of the tandem cell as pursued in this work resides in the use of different metal oxide semiconductors at either photojunction with the intent of positioning the energy levels in the system to best drive overall water splitting to form O_2 and H_2.

The utilization of SnO_2 in the system comes with some complication as studies exploring the use of SnO_2 in DSSCs have shown such cells typically perform poorly.[107-109] Principal reasons for this likely lie in differences in the rate of electron injection[110] and increased rates of recombination with SnO_2 compared to TiO_2, resulting from the faster charge transport of SnO_2.[111] Forming a surface coating of a different metal oxide, one with a lower potential conduction band, though has proven effective in ameliorating the performance shortcomings of solar cells using only SnO_2.[112-114] I have used this same strategy, treating FTO–SnO_2 electrodes such to form a TiO_2 overcoat on the mesoporous SnO_2 layer. This treatment involves soaking of the FTO–SnO_2 electrode in an aqueous

solution of $TiCl_4$ (40 mM) at room temperature overnight, followed by heating the electrode at 450 °C for 30 minutes.[112] In addition to the TiO_2 overcoat, SnO_2 electrodes used also contain a non-porous layer of SnO_2 between the FTO surface and the mesoporous SnO_2 layer. Establishing the compact layer follows from spin coating a solution of 15 wt% SnO_2 in water on the conductive face of the FTO (2000 rpm, 1 min) and then heating at 450 °C for 45 min. In principle, this layer should serve to hinder charge recombination from the back contact (FTO surface) to species in the electrolyte that could, in the absence of this blocking layer, access the FTO.[115] Electrodes based on SnO_2 that contain both the TiO_2 overcoat and compact SnO_2 layer out perform those lacking such treatments or possessing only one or the other treatment. Analogously, TiO_2 electrodes used here also contain a compact layer on the FTO face formed by spray pyrolysis of 0.1 M titanium diisopropoxide bis(acytylacetate) and undergo treatment with $TiCl_4$ prior to use.[116, 117] Details on preparing the TiO_2 or SnO_2 gels for forming the mesoporous electrodes can be found in Kang *et al.*[118] and Chappel *et al.*[107] respectively.

Photoanode for Water Oxidation

A collaboration with the Mallouk lab at The Pennsylvania State University led to the development of a photoanode composed of a transparent fluorine doped tin oxide (FTO) conductive glass support bearing a nanoparticulate TiO_2 semiconducting layer to which is adsorbed a trisbipyridylruthenium(II) ($Ru(bpy)_3^{2+}$)–hydrated iridium oxide ($IrO_x{\cdot}nH_2O$) complex.[53] A photoelectrochemical cell (PEC) consisting of this electrode in combination with a platinum cathode in aqueous solution demonstrated overall photolytic water splitting to oxygen and hydrogen, with the application of a small bias.

This system resembles a triad-type reaction center with a $Ru(bpy)_3^{2+}$ light absorber and primary electron donor, a TiO_2 primary acceptor, and an $IrO_x{\cdot}nH_2O$ secondary electron donor. Ideally, four sequential photocycle turnovers consisting of excitation of the $Ru(bpy)_3^{2+}$, electron transfer to the TiO_2 resulting in current flow to the platinum counter electrode, and hole transport to the $IrO_x{\cdot}nH_2O$, results in the conversion of water to oxygen at the $IrO_x{\cdot}nH_2O$ surface and production of hydrogen at the platinum cathode. While overall water splitting was observed, spectroscopic study of the system revealed that the charge recombination from the TiO_2 to the oxidized dye occurred nearly an order of magnitude faster than the forward electron transfer from the $IrO_x{\cdot}nH_2O$ to regenerate the ground state dye. This charge recombination imposes a major limitation on the performance of the system and represents a critical area for improvement.

In PSII, Tyr_Z serves the function of charge transfer mediator between P_{680} and the OEC and limits the occurrence of charge recombination. An effort to address the analogous recombination in this artificial system centered on the use of the benzimidazolephenol of the BiP–P_{F10}–TiO_2 triad (Figure 7) as a redox mediator in the photoelectrochemical system. Chemically modifying the BiP with a dicarboxylate functionality enabled the production of colloidal $IrO_x{\cdot}nH_2O$ particles decorated with both the BiP mediator and 2-dicarboxyethylphosphonic acid (CEPA).[119] Study of a PEC similar to that of the earlier work but using an FTO–TiO_2 photoanode bearing co-immobilized $Ru(bpy)_3^{2+}$ dye and BiP/CEPA–$IrO_x{\cdot}nH_2O$ shows that the BiP mediator improves the performance of the system. As compared to a cell without the mediator (using only CEPA capped $IrO_x{\cdot}nH_2O$), higher photocurrents and greater overall efficiency (about a factor of three) are observed. Transient bleaching recovery traces

showed that the improved performance results from faster regeneration of the ground state dye from the first oxidized state with the presence of BiP in the system.[119] Thus, BiP serves a similar role to that of Tyr_Z in PSII by preventing recombination losses after light induced charge separation.

In a second effort to improve the system, and in particular address the susceptibility of the $Ru(bpy)_3^{2+}$ chromophore to bleaching in aqueous media, I have worked on the development of photoanodes with comparable architectures but ones that incorporate porphyrin dyes. In preparing the photoanodic surface I have pursued two general procedures, either forming and then adsorbing the dye–catalyst construct to the metal oxide electrode surface or co-immobilizing the dye and catalyst on the surface. Both of these procedures for preparing the photoanode have proven effective using ruthenium(II) tris(bipyridyl) dyes.[53, 119]

Synthesis of the dye–catalyst construct can be carried out using two methods. The first method, as outlined in Chapter 2, begins from the Ir(IV) salt in presence of the capping dye molecule. The second method, developed by Dr. Yixin Zhao during a postdoctoral study at Pennsylvania State University in the lab of Dr. Tom Mallouk (unpublished), consists of forming $IrO_x{\cdot}nH_2O$ in the absence of stabilizing groups (other than OH^-) near neutral pH, purifying the colloid, and then refluxing the sample in the presence of a suitable capping group. Briefly, preparing this form of $IrO_x{\cdot}nH_2O$ comprises forming the colloid from K_2IrCl_6 in water with dilute NaOH sufficient to maintain neutral to slightly alkaline pH (between 7 to 8). Careful monitoring and maintenance of solution pH between 7–8 while heating the solution at 70 °C for 1–2 hr results in a deep blue, stable colloidal solution of $IrO_x{\cdot}nH_2O$. Purification of the colloid

(by removal of Ir(IV) complexes in solution)[119, 120] follows by addition of isopropanol (1:1 ration by volume), centrifugation of the sample to precipitate $IrO_x \cdot nH_2O$ nanoparticles, removal of supernatant, and resuspension of the $IrO_x \cdot nH_2O$ in neutral water. The addition of a suitable capping group to the $IrO_x \cdot nH_2O$ solution, followed by treatment at 70 °C under condensation for 1–3 hr, and purification by centrifugation results in the attachment of the capping group to the $IrO_x \cdot nH_2O$ as verified by UV-Vis spectroscopy. Such complexes have been formed using porphyrins **1** and **2**. Rigorous structural characterization of the complex has not been carried out. Soaking FTO–SnO_2 and FTO–TiO_2 electrodes in solutions of the porphyrin–$IrO_x \cdot nH_2O$ yield lightly tinted films, indicating poor loading of the complex. Phototesting of the anodes in a photoelectrochemical system produces low photocurrents.

Alternatively, co-immobilizing the porphyrin and catalyst on the metal oxide surface can result in high loading of the dye and catalyst. In general, electrodes prepared in this manner perform slightly better than those soaked in solutions of the dye–$IrO_x \cdot nH_2O$ complex yet the photocurrents produced still remain quite low. Both sequential soaking of the dye, then catalyst; catalyst, then dye; and soaking in a solution containing both catalyst and dye has been explored. It should be noted that the use of a water insoluble porphyrin precludes the latter as all $IrO_x \cdot nH_2O$ colloidal solutions used are, by synthetic necessity, aqueous. Recent work by Murray *et al.*[121] has presented $IrO_x \cdot nH_2O$ colloidal solutions stabilized in organic solvent and pursuing this manner of preparation could prove valuable in forming the photoanode. Of the porphyrin dyes used here, water insoluble dyes in organic solvents adsorb much more readily and result in better loading than water soluble dyes in aqueous solution regardless of the anchoring

group. Forming the dye, catalyst layer in organic solvent may prove a favorable strategy, given good stability of the dye and catalyst on the surface when exposed to aqueous media and that the catalytic activity of the $IrO_x \cdot nH_2O$ is not compromised in the process of stabilizing in organic solvent.

Photoanodes prepared by adsorption of a porphyrin–$IrO_x \cdot nH_2O$ complex or by co-immobilization of porphyrin and $IrO_x \cdot nH_2O$ have produced modest photocurrents of several microamps per square centimeter. Efforts have been made to correlate this activity to the net production of oxygen and hydrogen, however, direct proof of water oxidation and hydrogen formation remains elusive. This could be a result of limitations in the experimental setup, and efforts are underway to address this. Catalytic water oxidation by a porphyrin–$IrO_x \cdot nH_2O$ complex has been shown electrochemically and the production of O_2 photoelectrochemically verified in the $Ru(bpy)_3^{2+}$–$IrO_x \cdot nH_2O$ system and these lines of evidence suggest the sustenance of photocurrent in the porphyrin–$IrO_x \cdot nH_2O$ system via water oxidation.

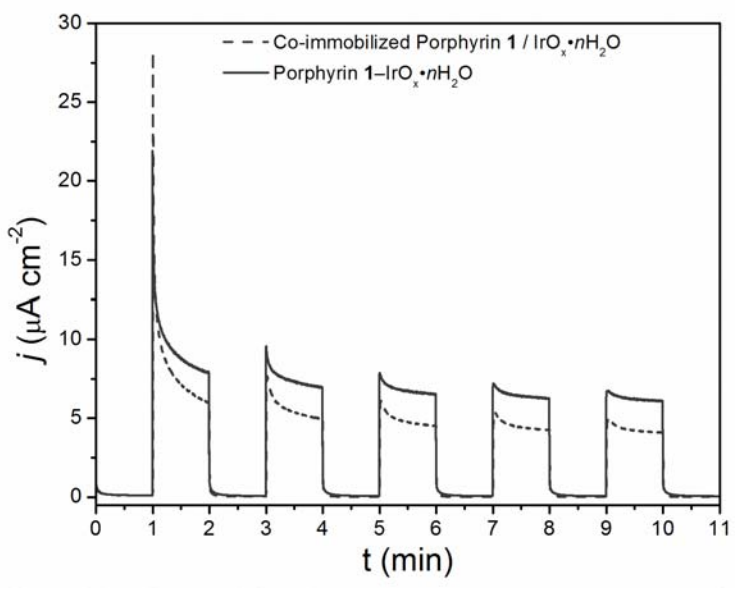

Figure 31. Comparison of the photocurrents produced by FTO–TiO_2 photoanodes prepared by either co-immobilization of porphyrin **1** and $IrO_x{\cdot}nH_2O$ or the adsorption of the porphyrin **1**–$IrO_x{\cdot}nH_2O$ complex. Experiments carried out in a three electrode photoelectrochemical cell with an FTO–TiO_2 working, an SCE reference, and a Pt counter electrode. A constant voltage of 0.2 V vs. SCE was applied during the entire experiment. Illumination by a Xe lamp (100 mW cm^{-2}, AM 1.5 filter) was alternated in 1 min increments with the current trace beginning in the dark.

Red Absorbing Junction

The second junction comprising the tandem cell consists of a dye sensitized photovoltaic solar cell containing a chromophore that absorbs redder of that used in the photoanode of the water oxidizing cell. Non-peripheral octabutoxy phthalocyanines have particular merit for the role in the red absorbing junction due to absorption in the near-IR coupled with a low potential excited state.[122] Phototesting of DSSCs composed of the phthalocyanines **7** and **8**, shown in Figure 32, yielded surprising results regarding the activity of the axial versus periphery immobilized dyes. Relatively high photocurrents were obtained with the axial functionalized phthalocyanine **8** as compared to the periphery carboxylic phthalocyanine **7** despite higher loading of the latter over the former

on TiO_2. The spectrum of the phthalocyanine **7** on TiO_2 does present a much broader Q band as compared to the phthalocyanine **8** indicating the possibility of aggregation on the surface. This is one possible reason for the relatively poor performance of the phthalocyanine **7** and the use of co-adsorbate, such as chenodeoxycholic acid,[123] could be useful in clarifying this issue.

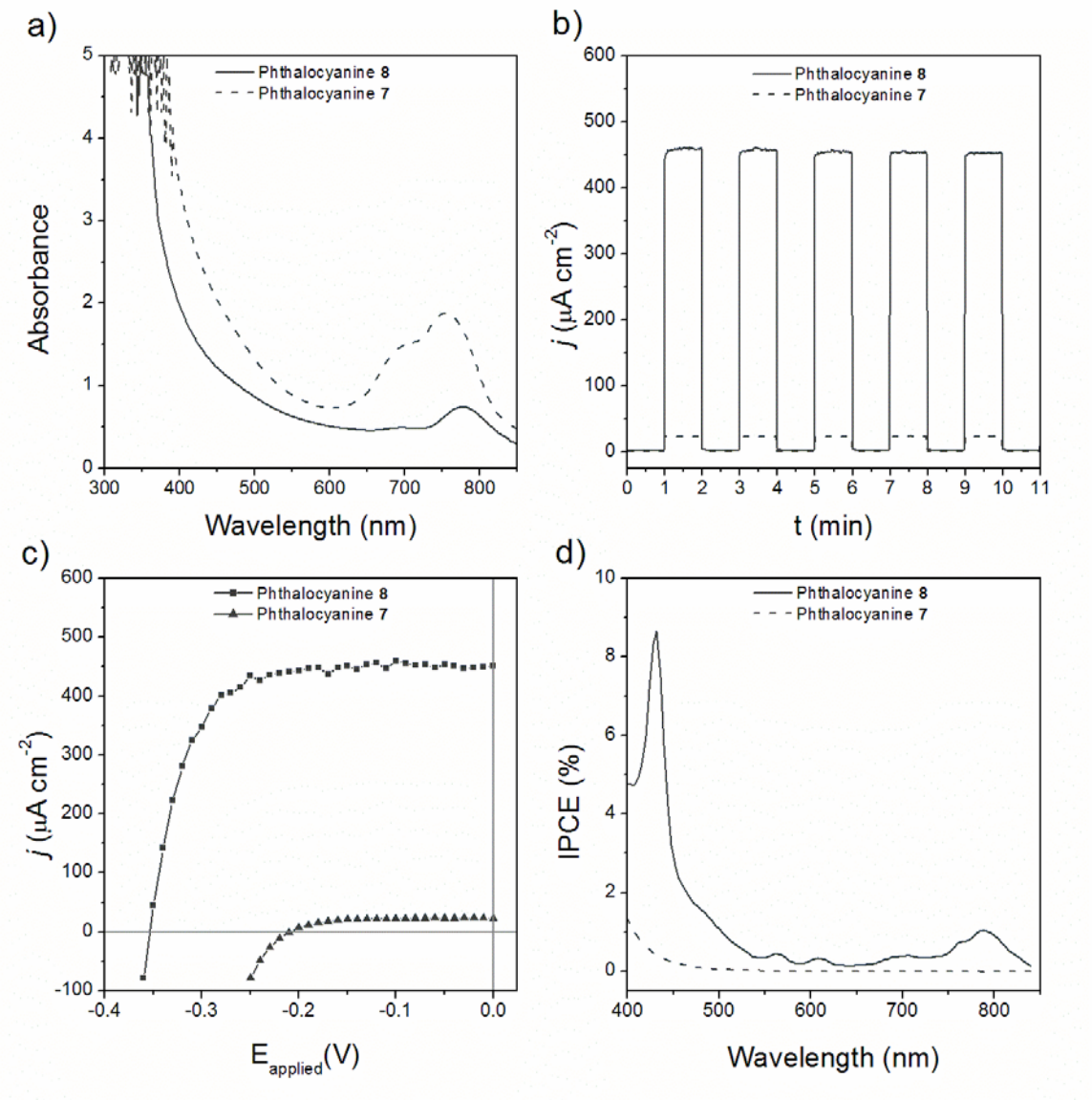

Figure 32. Comparative performance of photocells prepared with phthalocyanines **7** and **8**: a) absorbance of FTO–TiO_2 electrodes with adsorbed layers of the indicated phthalocyanine; b) photocurrent traces measured at no applied voltage with illumination by Xe lamp (100 mW cm^{-2}, AM 1.5 filter, 400 nm longpass filter) with 1 min dark–light cycles; c) current vs. voltage plots under illumination; d) incident photon to current efficiency plots. The electrolyte of the cells consisted of 1:1 by volume of acetonitrile:valeronitrile, 0.2 M lithium iodide, 0.05 M I_2, 0.2 M tetrabutylammonium iodide, and 0.5 M 4-t-butylpyridine.

Tandem Cell with Use of a Sacrificial Donor

In order to asses the feasibility of the design as shown in Figure 28, I assembled and studied a tandem cell consisting of a PEC cell with a SnO_2–porphyrin **5** photoanode and a DSSC cell containing a TiO_2–porphyrin **5** photoanode. Such a cell, of course, lacks any spectral division between the photo-active electrodes and, also absent any catalyst, cannot carry out light driven water oxidation. Such a diagnostic cell is useful, however, in demonstrating the feasibility of the design to facilitate current flow through the system and show the production of H_2 at the PEC cathode (electrode 4, Figure 28) with use of a sacrificial donor at the PEC anode (electrode 1, Figure 28) such as reduced nicotinamide adenine dinucleotide (NADH) or hydroquinone (QH_2). Figure 33 shows comparative current vs. time and current vs. applied potential traces of the SnO_2–**5** // TiO_2–**5** tandem cell (PEC electrolyte containing NADH) with traces of the individual SnO_2–**5** PEC cell (electrolyte containing NADH) and TiO_2–**5** PV cells for comparison. The current vs. time traces were taken without applied voltage, and comparison of the photocurrent of the isolated PEC as compared to the tandem configuration shows a marked improvement in current. The open circuit voltage of the tandem cell is greater that that of either component cell alone. Moreover, the open circuit voltage produced by the tandem cell approaches the sum of the component cell voltages as expected for two cells linked in series.

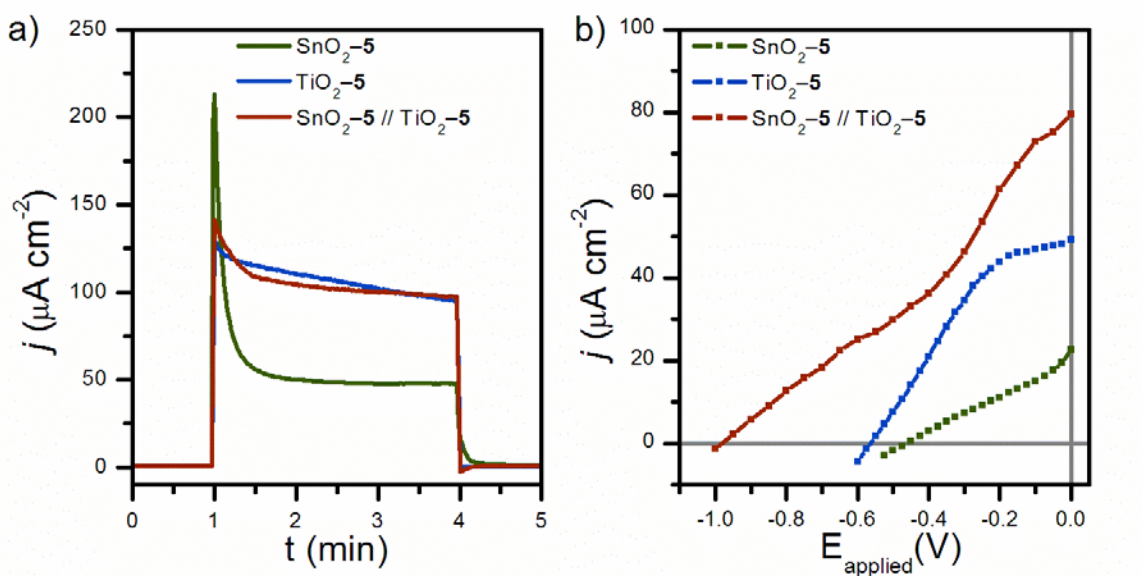

Figure 33. a) Current vs. time and b) current vs. applied potential for a tandem photoelectrochemical cell and both component cells measured in isolation. The electrolyte in contact with the SnO_2–**5** photoanode contained the sacrificial donor NADH, the oxidation of which sustains the observed photocurrent. Currents shown in a) and voltages shown in b) were measured with a Kiethly 2400 source meter wired as follows: green line – between electrode 1 and 4, 2 and 3 not connected; blue line – between electrode 2 and 3, 1 and 4 not connected; red line – between electrode 1 and 2, 3 and 4 connected as shown in Figure 28.

The production of H_2 at the dark Pt cathode (electrode 4 in Figure 28) was not measured in the above tandem cell though a comparable experiment did demonstrate the production of H_2 by the system with the use of QH_2 as sacrificial electron donor. A tandem cell consisting of FTO–TiO_2–**5** | PO_4–$IrO_x{\cdot}nH_2O$ and FTO–TiO_2–**5** as electrode 1 and electrode 3 (as shown in Figure 28), respectively, qualitatively demonstrated the production of H_2 as measured by gas chromatography (GC). In this instance the electrolyte of the PEC cell consisted of 0.025 M Na_2SiF_6 (pH 5.8, adjusted with $NaHCO_3$), 0.1 M Na_2SO_4, and 10 mM QH_2. After 30 min of illumination, a gas sample collected over the Pt cathode (electrode 4), as analyzed by GC, showed the presence of H_2, with the corresponding H_2 peak absent in a gas sample analyzed immediately before

illumination of the cell. Figure 34 shows the photocurrent trace and observed H_2 signal by GC. An earlier experiment with a similar tandem cell configuration failed to produce any H_2 by similar analysis; it is important to note that in this case, 0.1 M KNO_3 was used as supporting electrolyte and in the above mentioned cell, 0.1 M Na_2SO4 was used. Though the reduction of residual dissolved O_2 at the cathode (electrolyte purged with Ar before experimental runs in either case) might explain the lack of H_2 formation in the earlier experiment, it is possible that the reduction of NO_3^- at the cathode occurs over the production of H_2, with the comparable reduction of SO_4^{2-} energetically less likely to compete with the reduction of H^+. In either case, the result shown in Figure 34 verifies that the tandem cell design as explored herein can in principle drive the formation of H_2.

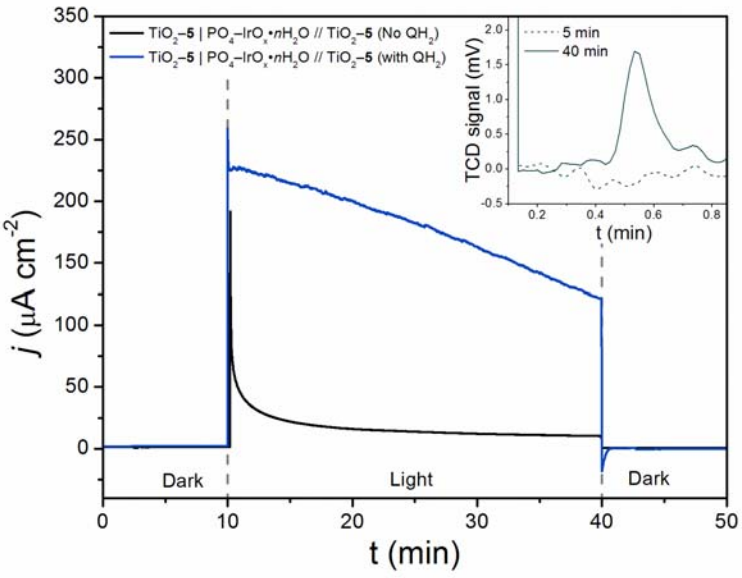

Figure 34. Photocurrent trace of a tandem photoelectrochemical cell incorporating both a TiO_2–**5** | PO_4–IrO_x•*n*H_2O photoanode (electrode 1 as shown in Figure 28) and a TiO_2–**5** photoanode (electrode 3 as shown in Figure 28). The blue trace shows the photocurrent in the presence of QH_2 and the black trace in the absence of QH_2. The inset plot shows gross data as measured by GC of gas samples taken at 5 min and 40 min of the photocurrent trace. The signal peak at ~0.55 min corresponds to the presence of H_2.

Tandem Cell for Water Splitting

I have made several attempts at constructing a tandem water splitting cell, composed of photoelectrodes as described above, though no trials have unequivocally demonstrated the net production of oxygen and hydrogen with light by the system. Using SnO_2 based photoanodes at the intended water oxidizing junction in concert with TiO_2 photoanodes at the second junction to drive hydrogen production manifests the intent outlined earlier of employing different metal oxide semiconductors with coordinated band energetics for driving the separate half reactions of overall water splitting. In addition, the use of $Ru(bpy)_3^{2+}$ and porphyrin, $Ru(bpy)_3^{2+}$ and phthalocyanine, or porphyrin and phthalocyanine dye combinations have been explored. Each combination allows for splitting of the spectrum between the two junctions though neither duo achieves the ideal separation as mentioned earlier.

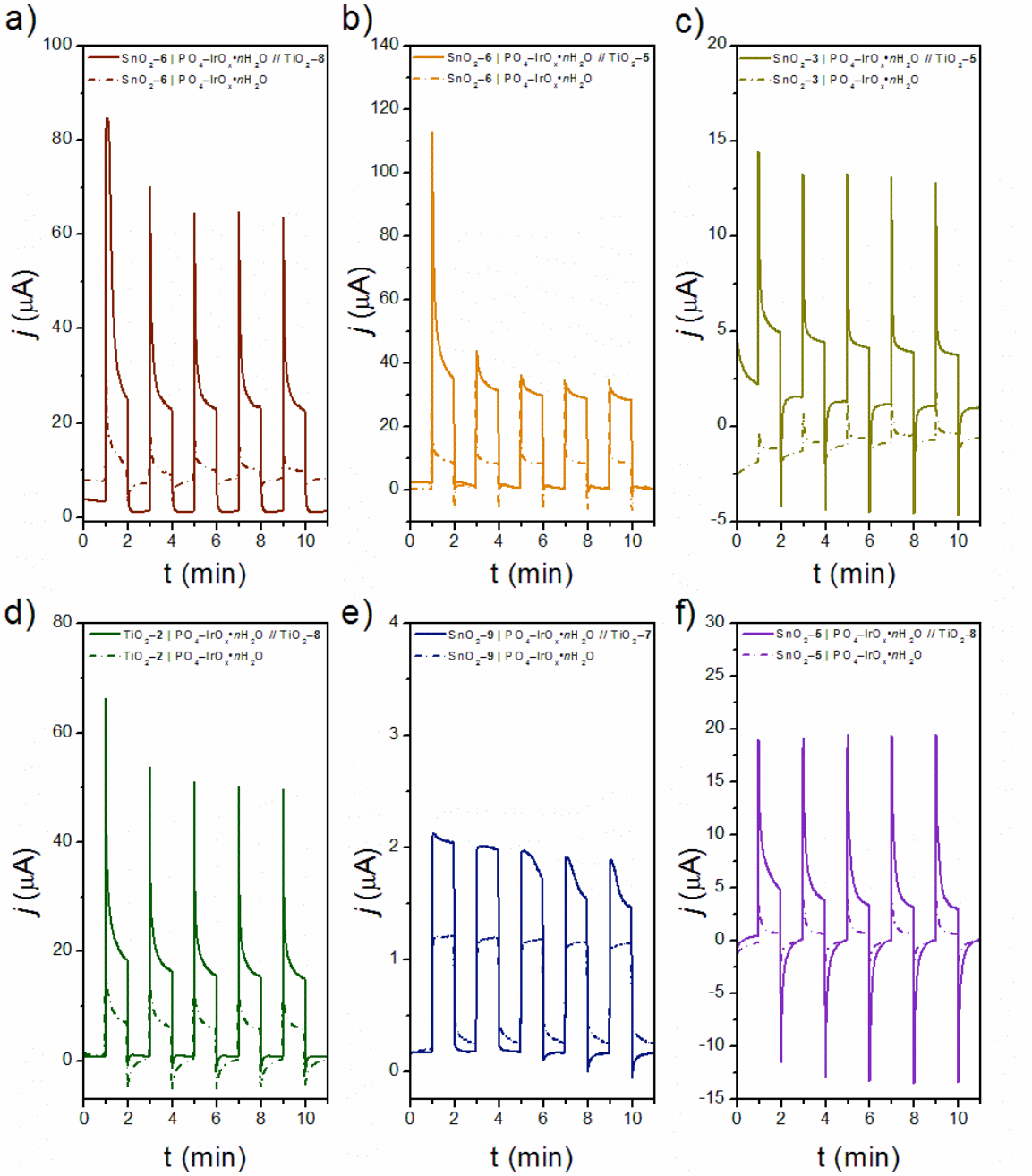

Figure 35. Photocurrent traces for several tandem cells representing different combinations of bluer and redder absorbing dyes: a) electrode 1: SnO_2–**6**, electrode 3: TiO_2-**8**; b) electrode 1: SnO_2–**6**, electrode 3: TiO_2–**5**; c) electrode 1: SnO_2–**3**, electrode 3: TiO_2–**5**; d) electrode 1: TiO_2–**2**, electrode 3: TiO_2–**8**; e) electrode 1: SnO_2–**9**, electrode 3: TiO_2–**7**; f) electrode 1: SnO_2–**5**, electrode 3: TiO_2–**8**. Electrode # assignment corresponds to numbering shown in Figure 28. For each current vs. time trace shown, solid line

indicates results from the tandem cell configuration and punctuated line that of just the PEC alone. For each cell, electrode 1 was prepared by co-immobilizing the indicated dye with PO_4–$IrO_x{\cdot}nH_2O$ catalyst and the aqueous electrolyte consisted of 0.025 M Na_2SiF_6 (pH 5.8, adjusted with $NaHCO_3$) and 0.1 M KNO_3 or 0.1 M Na_2SO_4. Illumination was supplied by Xe lamp, 100 mW cm^{-2}, with AM 1.5 and 400 nm long pass filters, and dark and light regimes were cycled at 1 min intervals to generate the trace.

Figure 35 shows photocurrent traces for six different tandem photoelectrochemical cells containing different combinations of chromophores as well as the photocurrent trace of a PEC consisting of only the bluer absorbing photoanode (the DSSC not connected in tandem). The figure caption gives the details of the experimental setup, but as a whole these traces illustrate the performance trends observed with the tandem systems. On the whole, the tandem configuration supports a higher photocurrent than the single junction PEC. In a sense, the tandem configuration is akin to running the single junction cell with an applied bias; applying a bias equal to the photovoltage achieved by the DSSC to the PEC should in theory give the same photocurrent as achieved by the tandem cell. Most the molecular dye based photoelectrochemical systems studied to date require an applied bias to achieve overall water splitting[53, 119, 124, 125] but an important distinction of system design here rests in the fact that the applied bias comes from light rather than an external electrical circuit.

Upon initial illumination, some the of the tandem cells achieve photocurrents in excess of 100 μA though such current levels to not sustain and quickly decay to much lower values. Ensuing dark–light–dark cycles (1 min intervals) show similar form, highest currents immediately following the dark–light transition with the traces leveling off to steady currents of several microamps. The decay in photocurrent, likely caused by

polarization of the surface, has been observed in similar systems.[53, 119, 124] The charging of the surface might indicate that initial charge transfer occurs readily though successive charge separation events become stagnated by accumulated charges on the surface due to slow kinetics of catalytic turnover, poor coupling between the dye and catalyst, or lowering of the local pH which would encumber water oxidation. The light to dark transition also reveals some indication of the performance of the system; shuttering of the light source coincides with inversion of the current from anodic to cathodic, with the cathodic transient gradually decaying over the course of the dark cycle. This cathodic dark current must arise from charge flow back to accumulated holes on the electrode surface. This would then indicate poor catalytic turnover on the surface resulting in the accumulation of charge (without adequate dissipation via the catalytic turnover) as well as substantial loss in photocurrent to recombination during the light regime. From this, I infer poor electronic communication between the dye and catalyst, low turnover with the catalyst, and/or poor insulation of the catalyst from the semiconductor surface. Earlier spectroscopic work on the $Ru(bpy)_3^{2+}$–$IrO_x{\cdot}nH_2O$ system showed faster recombination from the metal oxide semiconductor to the oxidized $Ru(bpy)_3^{3+}$ than the forward charge transfer from the $IrO_x{\cdot}nH_2O$ to regenerate the ground state dye.[53] The motivation for using high potential porphyrin dyes centered on improving the rate of charge transfer from the $IrO_x{\cdot}nH_2O$ to the oxidized dye by increased driving force supplied by the higher potential oxidized porphyrin as compared to Ru(III) dye. Unfortunately, tests to this point have not demonstrated greater efficacy of the porphyrin systems over that with $Ru(bpy)_3^{2+}$. In depth spectroscopic investigation of the persistence of the light generated oxidized porphyrin, rate of recombination from the sensitized SnO_2 to the oxidized dye,

and rate of charge transfer from the $IrO_x \cdot nH_2O$ to the oxidized dye has not been conducted. Such investigation could elucidate limits in the system and allow for comparison to the previously studied $Ru(bpy)_3^{2+}$ system. A recent study of an analogous photoanode, one employing a Ru(II) bipyridyl complex as light absorber and ruthenium based molecular water oxidation catalyst, demonstrated remarkably high photocurrents.[124] One distinguishing feature of this system is the use of a trioxy silane anchor bearing an aliphatic linker to the catalyst. It is possible this helps insulate the catalyst from the semiconductor surface while maintaining good interaction with the dye. Adapting a similar strategy with linking the $IrO_x \cdot nH_2O$ and in combination with the use of the BiP charge transfer mediator presents an attractive route to possibly improving the performance of this system.

Conclusion

The tandem photoelectrochemical cell, as depicted in Figure 28, consisting of dye sensitized metal oxide semiconductor based photoanodes shows improved photocurrent generation over the analogous single junction photoelectrochemical cell, whether run in the presence of a sacrificial donor (NADH or QH_2 used here) or, in solution containing only buffer and supporting electrolyte, conceivably by the oxidation of water. Overall water splitting to O_2 and H_2, with the use of $IrO_x \cdot nH_2O$ based catalyst at the water oxidizing anode, has not yet unambiguously been demonstrated. Such cells do sustain photocurrent, likely indicative of water oxidation and proton reduction, and ongoing efforts aim to demonstrate this point.

REFERENCES

1. Rockstrom, J.; Steffen, W.; Noone, K.; Persson, A.; Chapin, F. S.; Lambin, E. F.; Lenton, T. M.; Scheffer, M.; Folke, C.; Schellnhuber, H. J.; Nykvist, B.; de Wit, C. A.; Hughes, T.; van der Leeuw, S.; Rodhe, H.; Sorlin, S.; Snyder, P. K.; Costanza, R.; Svedin, U.; Falkenmark, M.; Karlberg, L.; Corell, R. W.; Fabry, V. J.; Hansen, J.; Walker, B.; Liverman, D.; Richardson, K.; Crutzen, P.; Foley, J. A., A Safe Operating Space for Humanity. *Nature* **2009**, 461, (7263), 472-475.

2. Armaroli, N.; Balzani, V., The Future of Energy Supply: Challenges and Opportunities. *Angewandte Chemie International Edition* **2007**, 46, (1-2), 52-66.

3. Bard, A. J.; Fox, M. A., Artificial Photosynthesis: Solar Splitting of Water to Hydrogen and Oxygen. *Accounts of Chemical Research* **1995**, 28, (3), 141-145.

4. Gust, D.; Moore, T. A.; Moore, A. L., Solar Fuels via Artificial Photosynthesis. *Accounts of Chemical Research* **2009**, 42, (12), 1890-1898.

5. Sorensen, B., *Renewable Energy: Its Physics, Engineering, Use, Environmental Impacts, Economy and Planning Aspects* 3ed.; Elsevier Science: Amsterdam, **2004**.

6. Ito, A., A Historical Meta-analysis of Global Terrestrial Net Primary Productivity: Are Estimates Converging? *Global Change Biology* **2011**, 17, (10), 3161-3175.

7. Archer, M. D.; Barber, J., *Molecular to Global Photosynthesis*. Imperial College Press: London, **2004**.

8. Cramer, W.; Kicklighter, D. W.; Bondeau, A.; Moore, B. I.; Churkina, G.; Nemry, B.; Ruimy, A.; Schloss, A. L.; The Participants of the Potsdam NPP Model Intercomparison, Comparing Global Models of Terrestrial Net Primary Productivity (NPP): Overview and Key Results. *Global Change Biology* **1999**, 5, 1-15.

9. Field, C. B.; Behrenfeld, M. J.; Randerson, J. T.; Falkowski, P., Primary Production of the Biosphere: Integrating Terrestrial and Oceanic Components. *Science* **1998**, 281, (5374), 237-240.

10. Haberl, H.; Erb, K. H.; Krausmann, F.; Gaube, V.; Bondeau, A.; Plutzar, C.; Gingrich, S.; Lucht, W.; Fischer-Kowalski, M., Quantifying and Mapping the Human Appropriation of Net Primary Production in Earth's Terrestrial Ecosystems. *Proceedings of the National Academy of Sciences* **2007**, 104, (31), 12942-12947.

11. Barnosky, A. D.; Hadly, E. A.; Bascompte, J.; Berlow, E. L.; Brown, J. H.; Fortelius, M.; Getz, W. M.; Harte, J.; Hastings, A.; Marquet, P. A.; Martinez, N. D.; Mooers, A.; Roopnarine, P.; Vermeij, G.; Williams, J. W.; Gillespie, R.; Kitzes, J.; Marshall, C.;

Matzke, N.; Mindell, D. P.; Revilla, E.; Smith, A. B., Approaching a State Shift in Earth's Biosphere. *Nature* **2012**, 486, (7401), 52-58.

12. IPPC, Special Report on Renewable Energy Sources and Climate Change Mitigation. **2011**, 1-1088.

13. Gust, D.; Moore, T. A., Mimicking Photosynthesis. *Science* **1989**, 244, (4900), 35-41.

14. Moore, T. A.; Gust, D.; Mathis, P.; Mialocq, J.-C.; Chachaty, C.; Bensasson, R. V.; Land, E. J.; Doizi, D.; Liddell, P. A.; Lehman, W. R.; Nemeth, G. A.; Moore, A. L., Photodriven Charge Separation in a Carotenoporphyrin-Quinone Triad. *Nature* **1984**, 307, (5952), 630-632.

15. Gust, D.; Moore, T. A.; Liddell, P. A.; Nemeth, G. A.; Makings, L. R.; Moore, A. L.; Barrett, D.; Pessiki, P. J.; Bensasson, R. V., Charge Separation in Carotenoporphyrin-Quinone Triads: Synthetic, Conformational, and Fluorescence Lifetime Studies. *Journal of the American Chemical Society* **1987**, 109, (3), 846-856.

16. Gust, D.; Moore, T. A.; Moore, A. L., Molecular Mimicry of Photosynthetic Energy and Electron Transfer. *Accounts of Chemical Research* **1993**, 26, (4), 198-205.

17. Kuciauskas, D.; Liddell, P. A.; Lin, S.; Stone, S. G.; Moore, A. L.; Moore, T. A.; Gust, D., Photoinduced Electron Transfer in Carotenoporphyrin-Fullerene Triads: Temperature and Solvent Effects. *The Journal of Physical Chemistry B* **2000**, 104, (18), 4307-4321.

18. Kodis, G.; Liddell, P. A.; Moore, A. L.; Moore, T. A.; Gust, D., Synthesis and Photochemistry of a Carotene–Porphyrin–Fullerene Model Photosynthetic Reaction Center. *Journal of Physical Organic Chemistry* **2004**, 17, (9), 724-734.

19. Gust, D.; Moore, T. A.; Moore, A. L.; Gao, F.; Luttrull, D.; DeGraziano, J. M.; Ma, X. C.; Makings, L. R.; Lee, S. J., Long-lived Photoinitiated Charge Separation in Carotene-Diporphyrin Triad Molecules. *Journal of the American Chemical Society* **1991**, 113, (10), 3638-3649.

20. Liddell, P. A.; Kuciauskas, D.; Sumida, J. P.; Nash, B.; Nguyen, D.; Moore, A. L.; Moore, T. A.; Gust, D., Photoinduced Charge Separation and Charge Recombination to a Triplet State in a Carotene–Porphyrin–Fullerene Triad. *Journal of the American Chemical Society* **1997**, 119, (6), 1400-1405.

21. Gust, D.; Moore, T. A.; Moore, A. L.; Macpherson, A. N.; Lopez, A.; DeGraziano, J. M.; Gouni, I.; Bittersmann, E.; Seely, G. R., Photoinduced Electron and Energy Transfer in Molecular Pentads. *Journal of the American Chemical Society* **1993**, 115, (24), 11141-11152.

22. Gust, D.; Moore, T. A.; Moore, A. L.; Lee, S.-J.; Bittersmann, E.; Luttrull, D. K.; Rehms, A. A.; DeGraziano, J. M.; Ma, X. C.; Gao, F.; Belford, R. E.; Trier, T. T., Efficient Multistep Photoinitiated Electron Transfer in a Molecular Pentad. *Science* **1990**, 248, (4952), 199-201.

23. Gust, D.; Moore, T. A.; Moore, A. L.; Barrett, D.; Harding, L. O.; Makings, L. R.; Liddell, P. A.; De Schryver, F. C.; Van der Auweraer, M.; et al., Photoinitiated Charge Separation in a Carotenoid-Porphyrin-Diquinone Tetrad: Enhanced Quantum Yields via Multistep Electron Transfers. *Journal of the American Chemical Society* **1988**, 110, (1), 321-323.

24. Gust, D.; Moore, T. A.; Moore, A. L.; Makings, L. R.; Seely, G. R.; Ma, X.; Trier, T. T.; Gao, F., A Carotenoid-Diporphyrin-Quinone Model for Photosynthetic Multistep Electron and Energy Transfer. *Journal of the American Chemical Society* **1988**, 110, (22), 7567-7569.

25. Imahori, H.; Hagiwara, K.; Aoki, M.; Akiyama, T.; Taniguchi, S.; Okada, T.; Shirakawa, M.; Sakata, Y., Linkage and Solvent Dependence of Photoinduced Electron Transfer in Zincporphyrin-C_{60} Dyads. *Journal of the American Chemical Society* **1996**, 118, (47), 11771-11782.

26. Liddell, P. A.; Sumida, J. P.; Macpherson, A. N.; Noss, L.; Seely, G. R.; Clark, K. N.; Moore, A. L.; Moore, T. A.; Gust, D., Preparation and Photophysical Studies of Porphyrin-C_{60} Dyads. *Photochemistry and Photobiology* **1994**, 60, (6), 537-541.

27. Kodis, G.; Liddell, P. A.; de la Garza, L.; Clausen, P. C.; Lindsey, J. S.; Moore, A. L.; Moore, T. A.; Gust, D., Efficient Energy Transfer and Electron Transfer in an Artificial Photosynthetic Antenna–Reaction Center Complex. *The Journal of Physical Chemistry A* **2002**, 106, (10), 2036-2048.

28. Bahr, J. L.; Kuciauskas, D.; Liddell, P. A.; Moore, A. L.; Moore, T. A.; Gust, D., Driving Force and Electronic Coupling Effects on Photoinduced Electron Transfer in a Fullerene-based Molecular Triad¶. *Photochemistry and Photobiology* **2000**, 72, (5), 598-611.

29. Steinberg-Yfrach, G.; Liddell, P. A.; Hung, S.-C.; Moore, A. L.; Gust, D.; Moore, T. A., Conversion of Light Energy to Proton Potential in Liposomes by Artificial Photosynthetic Reaction Centers. *Nature* **1997**, 385, (6613), 239-241.

30. Steinberg-Yfrach, G.; Rigaud, J.-L.; Durantini, E. N.; Moore, A. L.; Gust, D.; Moore, T. A., Light-driven Production of ATP Catalysed by F_0F_1-ATP synthase in an Artificial Photosynthetic Membrane. *Nature* **1998**, 392, (6675), 479-482.

31. Blankenship, R. E., *Molecular Mechanisms of Photosynthesis*. Wiley-Blackwell: Oxford, **2002**.

32. Kuciauskas, D.; Liddell, P. A.; Lin, S.; Johnson, T. E.; Weghorn, S. J.; Lindsey, J. S.; Moore, A. L.; Moore, T. A.; Gust, D., An Artificial Photosynthetic Antenna-Reaction Center Complex. *Journal of the American Chemical Society* **1999**, 121, (37), 8604-8614.

33. Kodis, G.; Terazono, Y.; Liddell, P. A.; Andreasson, J.; Garg, V.; Hambourger, M.; Moore, T. A.; Moore, A. L.; Gust, D., Energy and Photoinduced Electron Transfer in a Wheel-Shaped Artificial Photosynthetic Antenna-Reaction Center Complex. *Journal of the American Chemical Society* **2006**, 128, (6), 1818-1827.

34. Terazono, Y.; Kodis, G.; Liddell, P. A.; Garg, V.; Moore, T. A.; Moore, A. L.; Gust, D., Multiantenna Artificial Photosynthetic Reaction Center Complex. *The Journal of Physical Chemistry B* **2009**, 113, (20), 7147-7155.

35. Horton, P.; Ruban, A. V.; Walters, R. G., Regulation of Light Harvesting in Green Plants. *Annual Review of Plant Physiology and Plant Molecular Biology* **1996**, 47, (1), 655-684.

36. Muller, P.; Li, X.-P.; Niyogi, K. K., Non-Photochemical Quenching. A Response to Excess Light Energy. *Plant Physiology* **2001**, 125, (4), 1558-1566.

37. Straight, S. D.; Kodis, G.; Terazono, Y.; Hambourger, M.; Moore, T. A.; Moore, A. L.; Gust, D., Self-regulation of Photoinduced Electron Transfer by a Molecular Nonlinear Transducer. *Nature Nanotechnology* **2008**, 3, (5), 280-283.

38. Seta, P.; Bienvenue, E.; Moore, A. L.; Mathis, P.; Bensasson, R. V.; Liddell, P.; Pessiki, P. J.; Joy, A.; Moore, T. A.; Gust, D., Photodriven Transmembrane Charge Separation and Electron Transfer by a Carotenoporphyrin-Quinone triad. *Nature* **1985**, 316, (6029), 653-655.

39. Bennett, I. M.; Farfano, H. M. V.; Bogani, F.; Primak, A.; Liddell, P. A.; Otero, L.; Sereno, L.; Silber, J. J.; Moore, A. L.; Moore, T. A.; Gust, D., Active Transport of Ca^{2+} by an Artificial Photosynthetic Membrane. *Nature* **2002**, 420, (6914), 398-401.

40. Faller, P.; Goussias, C.; Rutherford, A. W.; Un, S., Resolving Intermediates in Biological Proton-Coupled Electron Transfer: A Tyrosyl Radical Prior to Proton Movement. *Proceedings of the National Academy of Sciences* **2003**, 100, (15), 8732-8735.

41. Rappaport, F.; Diner, B. A., Primary Photochemistry and Energetics Leading to the Oxidation of the $(Mn)_4Ca$ Cluster and to the Evolution of Molecular Oxygen in Photosystem II. *Coordination Chemistry Reviews* **2008**, 252, 259-272.

42. Moore, G. F.; Hambourger, M.; Gervaldo, M.; Poluektov, O. G.; Rajh, T.; Gust, D.; Moore, T. A.; Moore, A. L., A Bioinspired Construct That Mimics the Proton Coupled

Electron Transfer between $P680^{\bullet+}$ and the Tyr_Z-His190 Pair of Photosystem II. *Journal of the American Chemical Society* **2008**, 130, (32), 10466-10467.

43. Moore, G. F.; Hambourger, M.; Kodis, G.; Michl, W.; Gust, D.; Moore, T. A.; Moore, A. L., Effects of Protonation State on a Tyrosine-Histidine Bioinspired Redox Mediator. *The Journal of Physical Chemistry B* **2010**, 114, (45), 14450-14457.

44. Megiatto, J. D.; Antoniuk-Pablant, A.; Sherman, B. D.; Kodis, G.; Gervaldo, M.; Moore, T. A.; Moore, A. L.; Gust, D., Mimicking the Electron Transfer Chain in Photosystem II with a Molecular Triad Thermodynamically Capable of Water Oxidation. *Proceedings of the National Academy of Sciences* **2012**, 109, (39), 15578-15583.

45. Harriman, A.; Pickering, I. J.; Thomas, J. M.; Christensen, P. A., Metal-Oxides as Heterogeneous Catalysts for Oxygen Evolution under Photochemical Conditions. *Journal of the Chemical Society-Faraday Transactions I* **1988**, 84, 2795-2806.

46. Harriman, A.; Thomas, J. M.; Millward, G. R., Catalytic and Structural-Properties of Iridium-Iridium Dioxide Colloids. *New Journal of Chemistry* **1987**, 11, (11-12), 757-762.

47. Nahor, G. S.; Neta, P.; Hambright, P.; Thompson, A. N.; Harriman, A., Metalloporphyrin-Sensitized Photooxidation of Water to Oxygen on the Surface of Colloidal Iridium Oxides - Photochemical and Pulse Radiolytic Studies. *Journal of Physical Chemistry* **1989**, 93, (16), 6181-6187.

48. Petit, M. A.; Plichon, V., Anodic Electrodeposition of Iridium Oxide Films. *Journal of Electroanalytical Chemistry* **1998**, 444, (2), 247-252.

49. Yagi, M.; Tomita, E.; Sakita, S.; Kuwabara, T.; Nagai, K., Self-assembly of Active IrO_2 Colloid Catalyst on an ITO Electrode for Efficient Electrochemical Water Oxidation. *Journal of Physical Chemistry B* **2005**, 109, (46), 21489-21491.

50. Kuwabara, T.; Tomita, E.; Sakita, S.; Hasegawa, D.; Sone, K.; Yagi, M., Characterization and Analysis of Self-assembly of a Highly Active Colloidal Catalyst for Water Oxidation onto Transparent Conducting Oxide Substrates. *Journal of Physical Chemistry C* **2008**, 112, (10), 3774-3779.

51. Nakagawa, T.; Beasley, C. A.; Murray, R. W., Efficient Electro-Oxidation of Water near Its Reversible Potential by a Mesoporous IrO_x Nanoparticle Film. *Journal of Physical Chemistry C* **2009**, 113, (30), 12958-12961.

52. Nakagawa, T.; Bjorge, N. S.; Murray, R. W., Electrogenerated IrO_x Nanoparticles as Dissolved Redox Catalysts for Water Oxidation. *Journal of the American Chemical Society* **2009**, 131, (43), 15578-15579.

53. Youngblood, W. J.; Lee, S. H. A.; Kobayashi, Y.; Hernandez-Pagan, E. A.; Hoertz, P. G.; Moore, T. A.; Moore, A. L.; Gust, D.; Mallouk, T. E., Photoassisted Overall Water Splitting in a Visible Light-Absorbing Dye-Sensitized Photoelectrochemical Cell. *Journal of the American Chemical Society* **2009**, 131, (3), 926-927.

54. Hoertz, P. G.; Kim, Y. I.; Youngblood, W. J.; Mallouk, T. E., Bidentate Dicarboxylate Capping Groups and Photosensitizers Control the Size of IrO_2 Nanoparticle Catalysts for Water Oxidation. *Journal of Physical Chemistry B* **2007**, 111, (24), 6845-6856.

55. Wen, L.; Li, M.; Schlenoff, J. B., Polyporphyrin Thin Films from the Interfacial Polymerization of Mercaptoporphyrins. *Journal of the American Chemical Society* **1997**, 119, (33), 7726-7733.

56. Yokomatsu, T.; Minowa, T.; Murano, T.; Shibuya, S., Enzymatic Desymmetrization of Prochiral 2-benzyl-1,3-propanediol Derivatives: A Practical Chemoenzymatic Synthesis of Novel Phosphorylated Tyrosine Analogues. *Tetrahedron* **1998**, 54, (32), 9341-9356.

57. Scalise, I.; Durantini, E. N., Photodynamic Effect of Metallo 5-(4-carboxyphenyl)-10,15,20-tris(4-methylphenyl) Porphyrins in Biomimetic AOT Reverse Micelles Containing Urease. *Journal of Photochemistry and Photobiology A: Chemistry* **2004**, 162, (1), 105-113.

58. Guldi, D. M.; Zilbermann, I.; Anderson, G.; Li, A.; Balbinot, D.; Jux, N.; Hatzimarinaki, M.; Hirsch, A.; Prato, M., Multicomponent Redox Gradients on Photoactive Electrode Surfaces. *Chemical Communications* **2004**, 0, (6), 726-727.

59. Brimblecombe, R.; Koo, A.; Dismukes, G. C.; Swiegers, G. F.; Spiccia, L., Solar Driven Water Oxidation by a Bioinspired Manganese Molecular Catalyst. *Journal of the American Chemical Society* **2010**, 132, (9), 2892-2894.

60. Kiwi, J.; Gratzel, M., Hydrogen Evolution From Water Induced by Visible Light Mediated by Redox Catalysis. *Nature* **1979**, 281, (5733), 657-658.

61. Jiao, F.; Frei, H., Nanostructured Cobalt Oxide Clusters in Mesoporous Silica as Efficient Oxygen-Evolving Catalysts. *Angewandte Chemie International Edition* **2009**, 48, (10), 1841-1844.

62. Kanan, M. W.; Nocera, D. G., In Situ Formation of an Oxygen-Evolving Catalyst in Neutral Water Containing Phosphate and Co^{2+}. *Science* **2008**, 321, (5892), 1072-1075.

63. Shevchenko, D.; Anderlund, M. F.; Thapper, A.; Styring, S., Photochemical Water Oxidation with Visible Light Using a Cobalt Containing Catalyst. *Energy & Environmental Science* **2011**, 4, (4), 1284-1287.

64. Stamplecoskie, K. G.; Scaiano, J. C., Light Emitting Diode Irradiation Can Control the Morphology and Optical Properties of Silver Nanoparticles. *Journal of the American Chemical Society* **2010**, 132, (6), 1825-1827.

65. Maretti, L.; Billone, P. S.; Liu, Y.; Scaiano, J. C., Facile Photochemical Synthesis and Characterization of Highly Fluorescent Silver Nanoparticles. *Journal of the American Chemical Society* **2009**, 131, (39), 13972-13980.

66. McGilvray, K. L.; Decan, M. R.; Wang, D.; Scaiano, J. C., Facile Photochemical Synthesis of Unprotected Aqueous Gold Nanoparticles. *Journal of the American Chemical Society* **2006**, 128, (50), 15980-15981.

67. Pacioni, N. L.; Pardoe, A.; McGilvray, K. L.; Chretien, M. N.; Scaiano, J. C., Synthesis of Copper Nanoparticles Mediated by Photogenerated Free Radicals: Catalytic Role of Chloride Anions. *Photochemical & Photobiological Sciences* **2010**, 9, (6), 766-774.

68. Marin, M. L.; McGilvray, K. L.; Scaiano, J. C., Photochemical Strategies for the Synthesis of Gold Nanoparticles from Au(III) and Au(I) Using Photoinduced Free Radical Generation. *Journal of the American Chemical Society* **2008**, 130, (49), 16572-16584.

69. Jockusch, S.; Landis, M. S.; Freiermuth, B.; Turro, N. J., Photochemistry and Photophysics of α-Hydroxy Ketones. *Macromolecules* **2001**, 34, (6), 1619-1626.

70. Scaiano, J. C., Photochemical and Free-Radical Processes in Benzyl-Amine Systems - Electron-Donor Properties of Alpha-Aminoalkyl Radicals. *Journal of Physical Chemistry* **1981**, 85, (19), 2851-2855.

71. Scaiano, J. C.; Netto-Ferreira, J. C.; Alarcon, E.; Billone, P.; Bueno Alejo, C. J.; Crites, C. L.; Decan, M.; Fasciani, C.; González-Béjar, M.; Hallett-Tapley, G.; Grenier, M.; McGilvray, K. L.; Pacio, N. L.; Pardoe, A.; René-Boisneuf, L.; Schwartz-Narbonne, R.; Silvero, M. J.; Stamplecoskie, K. G.; Wee, T. L., Tuning Plasmon Transitions and their Applications in Organic Photochemistry. *Pure and Applied Chemistry* **2011**, 83, (4), 913-930.

72. Krueger, A., New Carbon Materials: Biological Applications of Functionalized Nanodiamond Materials. *Chemistry-a European Journal* **2008**, 14, (5), 1382-1390.

73. Liu, K. K.; Zheng, W. W.; Wang, C. C.; Chiu, Y. C.; Cheng, C. L.; Lo, Y. S.; Chen, C. P.; Chao, J. I., Covalent Linkage of Nanodiamond-Paclitaxel for Drug Delivery and Cancer Therapy. *Nanotechnology* **2010**, 21, (31), 315106.

74. Liu, Y.; Gu, Z. N.; Margrave, J. L.; Khabashesku, V. N., Functionalization of Nanoscale Diamond Powder: Fluoro-, Alkyl-, Amino-, and Amino Acid-Nanodiamond Derivatives. *Chemistry of Materials* **2004**, 16, (20), 3924-3930.

75. Kim, K. J.; Park, M.-S.; Kim, J. Y.; Kim, Y.-J., A Study on the Effect of Surface Modifications of the Carbon Felt Electrode on the Performance of Vanadium Redox Flow Battery. *ECS Meeting Abstracts* **2010**, 1002, (6), 405.

76. King, S.; Hyunh, K.; Tannenbaum, R., Kinetics of Nucleation, Growth, and Stabilization of Cobalt Oxide Nanoclusters. *Journal of Physical Chemistry B* **2003**, 107, (44), 12097-12104.

77. Hambourger, M.; Moore, T. A., Nailing Down Nickel for Electrocatalysis. *Science* **2009**, 326, (5958), 1355-1356.

78. Hambourger, M.; Moore, G. F.; Kramer, D. M.; Gust, D.; Moore, A. L.; Moore, T. A., Biology and Technology for Photochemical Fuel Production. *Chemical Society Reviews* **2009**, 38, (1), 25-35.

79. Khaselev, O.; Turner, J. A., A Monolithic Photovoltaic-Photoelectrochemical Device for Hydrogen Production via Water Splitting. *Science* **1998**, 280, (5362), 425-427.

80. Walter, M. G.; Rudine, A. B.; Wamser, C. C., Porphyrins and Phthalocyanines in Solar Photovoltaic Cells. *Journal of Porphyrins and Phthalocyanines* **2010**, 14, (9), 759-792.

81. Muthukumaran, K.; Loewe, R. S.; Ambroise, A.; Tamaru, S. I.; Li, Q. L.; Mathur, G.; Bocian, D. F.; Misra, V.; Lindsey, J. S., Porphyrins Bearing Arylphosphonic Acid Tethers for Attachment to Oxide Surfaces. *Journal of Organic Chemistry* **2004**, 69, (5), 1444-1452.

82. Loewe, R. S.; Ambroise, A.; Muthukumaran, K.; Padmaja, K.; Lysenko, A. B.; Mathur, G.; Li, Q. L.; Bocian, D. F.; Misra, V.; Lindsey, J. S., Porphyrins Bearing Mono or Tripodal Benzylphosphonic Acid Tethers for Attachment to Oxide Surfaces. *Journal of Organic Chemistry* **2004**, 69, (5), 1453-1460.

83. Martinez-Diaz, M. V.; de la Torrea, G.; Torres, T., Lighting Porphyrins and Phthalocyanines for Molecular Photovoltaics. *Chemical Communications* **2010**, 46, (38), 7090-7108.

84. Hanna, M. C.; Nozik, A. J., Solar Conversion Efficiency of Photovoltaic and Photoelectrolysis Cells with Carrier Multiplication Absorbers. *Journal of Applied Physics* **2006**, 100, (7).

85. Blankenship, R. E.; Tiede, D. M.; Barber, J.; Brudvig, G. W.; Fleming, G.; Ghirardi, M.; Gunner, M. R.; Junge, W.; Kramer, D. M.; Melis, A.; Moore, T. A.; Moser, C. C.; Nocera, D. G.; Nozik, A. J.; Ort, D. R.; Parson, W. W.; Prince, R. C.; Sayre, R. T., Comparing Photosynthetic and Photovoltaic Efficiencies and Recognizing the Potential for Improvement. *Science* **2011**, 332, (6031), 805-809.

86. Cosut, B.; Yesilot, S.; Durmus, M.; Kilic, A.; Ahsen, V., Synthesis and Properties of Axially-phenoxycyclotriphosphazenyl Substituted Silicon Phthalocyanine. *Polyhedron* **2010**, 29, (2), 675-682.

87. O'Regan, B. C.; Lopez-Duarte, I.; Martinez-Diaz, M. V.; Forneli, A.; Albero, J.; Morandeira, A.; Palomares, E.; Torres, T.; Durrant, J. R., Catalysis of Recombination and its Limitation on Open Circuit Voltage for Dye Sensitized Photovoltaic Cells Using Phthalocyanine Dyes. *Journal of the American Chemical Society* **2008**, 130, (10), 2906-2907.

88. Cook, M. J.; Dunn, A. J.; Daniel, M. F.; Hart, R. C. O.; Richardson, R. M.; Roser, S. J., Fabrication of Ordered Langmuir-Blodgett Multilayers of Octa-N-Alkoxy Phthalocyanines. *Thin Solid Films* **1988**, 159, 395-404.

89. Ke, M. R.; Huang, J. D.; Weng, S. M., Comparison Between Non-peripherally and Peripherally Tetra-substituted Zinc (II) Phthalocyanines as Photosensitizers: Synthesis, Spectroscopic, Photochemical and Photobiological Properties. *Journal of Photochemistry and Photobiology a-Chemistry* **2009**, 201, (1), 23-31.

90. Ermilov, E. A.; Tannert, S.; Werncke, T.; Choi, M. T. M.; Ng, D. K. P.; Roder, B., Photoinduced Electron and Energy Transfer in a New Porphyrin-Phthalocyanine Triad. *Chemical Physics* **2006**, 328, (1-3), 428-437.

91. Joyner, R. D.; Cekada, J.; Linck, R. G.; Kenney, M. E., Diphenoxysilicon Phthalocyanine. *Journal of Inorganic & Nuclear Chemistry* **1960**, 15, (3-4), 387-388.

92. Belabassi, Y.; Alzghari, S.; Montchamp, J. L., Revisiting the Hirao Cross-coupling: Improved Synthesis of Aryl and Heteroaryl Phosphonates. *Journal of Organometallic Chemistry* **2008**, 693, (19), 3171-3178.

93. Li, Z. Y.; Lieberman, M., Axial Reactivity of Soluble Silicon(IV) Phthalocyanines. *Inorganic Chemistry* **2001**, 40, (5), 932-939.

94. Huang, J. D.; Jiang, X. J.; Shen, X. M.; Tang, Q. Q., Synthesis and Photobiological Properties of Novel Silicon(IV) Phthalocyanines Axially Modified by Paracetamol and 4-Hydroxyphenylacetamide. *Journal of Porphyrins and Phthalocyanines* **2009**, 13, (12), 1227-1232.

95. Koyama, T.; Suzuki, T.; Hanabusa, K.; Shirai, H.; Kobayashi, N., A Comparison of the Loop-Current Effect of Silicon Phthalocyanine and Silicon Naphthalocyanine Rings on Their Axial Ligands. *Inorganica Chimica Acta* **1994**, 218, (1-2), 41-45.

96. Janson, T. R.; Kane, A. R.; Sullivan, J. F.; Knox, K.; Kenney, M. E., Ring-Current Effect of Phthalocyanine Ring. *Journal of the American Chemical Society* **1969**, 91, (19), 5210-5214.

97. Maree, M. D.; Nyokong, T., Synthesis, Spectroscopy and Electrochemistry of Octaphenoxyphthalocyaninato Silicon Complexes. *Journal of Porphyrins and Phthalocyanines* **2001**, 5, (7), 555-563.

98. Leng, X. B.; Ng, D. K. P., Axial Coordination of Porphyrinatocobalt(II) Complexes with Bis(pyridinolato)silicon(IV) Phthalocyanines. *European Journal of Inorganic Chemistry* **2007**, (29), 4615-4620.

99. Davison, J. B.; Wynne, K. J., Silicon Phthalocyanine-Siloxane Polymers - Synthesis and H-1 Nuclear Magnetic-Resonance Study. *Macromolecules* **1978**, 11, (1), 186-191.

100. Palacios, R. E.; Kodis, G.; Herrero, C.; Ochoa, E. M.; Gervaldo, M.; Gould, S. L.; Kennis, J. T. M.; Gust, D.; Moore, T. A.; Moore, A. L., Tetrapyrrole Singlet Excited State Quenching by Carotenoids in an Artificial Photosynthetic Antenna. *Journal of Physical Chemistry B* **2006**, 110, (50), 25411-25420.

101. Zhao, Z. X.; Cammidge, A. N.; Hughes, D. L.; Cook, M. J., Modular Face-to-Face Assembly of Multichromophore Arrays That Absorb Across the Complete UV-Visible Spectrum and into the Near-IR. *Organic Letters* **2010**, 12, (22), 5138-5141.

102. Durr, M.; Rosselli, S.; Yasuda, A.; Nelles, G., Band-gap Engineering of Metal Oxides for Dye-Sensitized Solar Cells. *Journal of Physical Chemistry B* **2006**, 110, (43), 21899-21902.

103. Bolton, J. R.; Strickler, S. J.; Connolly, J. S., Limiting and Realizable Efficiencies of Solar Photolysis of Water. *Nature* **1985**, 316, (6028), 495-500.

104. Bae, E.; Choi, W., Effect of the Anchoring Group (Carboxylate vs. Phosphonate) in Ru-Complex-Sensitized TiO_2 on Hydrogen Production Under Visible Light. *Journal of Physical Chemistry B* **2006**, 110, (30), 14792-14799.

105. Hambourger, M.; Brune, A.; Gust, D.; Moore, A. L.; Moore, T. A., Enzyme-assisted Reforming of Glucose to Hydrogen in a Photoelectrochemical Cell. *Photochemistry and Photobiology* **2005**, 81, (4), 1015-1020.

106. Hagfeldt, A.; Gratzel, M., Light-Induced Redox Reactions in Nanocrystalline Systems. *Chemical Reviews* **1995**, 95, (1), 49-68.

107. Chappel, S.; Zaban, A., Nanoporous SnO_2 Electrodes for Dye-Sensitized Solar Cells: Improved Cell Performance by the Synthesis of 18 nm SnO_2 Colloids. *Solar Energy Materials and Solar Cells* **2002**, 71, (2), 141-152.

108. Srivastava, D. N.; Chappel, S.; Palchik, O.; Zaban, A.; Gadanken, A., Sonochemical Synthesis of Mesoporous Tin Oxide. *Langmuir* **2002**, 18, (10), 4160-4164.

109. Bedja, I.; Hotchandani, S.; Kamat, P. V., Preparation and Photoelectrochemical Characterization of Thin SnO_2 Nanocrystalline Semiconductor-Films and Their Sensitization with Bis(2,2'-Bipyridine)(2,2'-Bipyridine-4,4'-Dicarboxylic Acid)-Ruthenium(II) Complex. *Journal of Physical Chemistry* **1994**, 98, (15), 4133-4140.

110. Asbury, J. B.; Hao, E.; Wang, Y. Q.; Ghosh, H. N.; Lian, T. Q., Ultrafast Electron Transfer Dynamics from Molecular Adsorbates to Semiconductor Nanocrystalline Thin Films. *Journal of Physical Chemistry B* **2001**, 105, (20), 4545-4557.

111. Green, A. N. M.; Palomares, E.; Haque, S. A.; Kroon, J. M.; Durrant, J. R., Charge Transport Versus Recombination in Dye-Sensitized Solar Cells Employing Nanocrystalline TiO_2 and SnO_2 Films. *Journal of Physical Chemistry B* **2005**, 109, (25), 12525-12533.

112. Kay, A.; Gratzel, M., Dye-Sensitized Core-Shell Nanocrystals: Improved Efficiency of Mesoporous Tin Oxide Electrodes Coated with a Thin Layer of an Insulating Oxide. *Chemistry of Materials* **2002**, 14, (7), 2930-2935.

113. Senevirathna, M. K. I.; Pitigala, P.; Premalal, E. V. A.; Tennakone, K.; Kumara, G. R. A.; Konno, A., Stability of the SnO_2/MgO Dye-Sensitized Photoelectrochemical Solar Cell. *Solar Energy Materials and Solar Cells* **2007**, 91, (6), 544-547.

114. Kim, M. H.; Kwon, Y. U., Semiconducting Divalent Metal Oxides as Blocking Layer Material for SnO_2-Based Dye-Sensitized Solar Cells. *Journal of Physical Chemistry C* **2011**, 115, (46), 23120-23125.

115. Snaith, H. J.; Ducati, C., SnO_2-Based Dye-Sensitized Hybrid Solar Cells Exhibiting Near Unity Absorbed Photon-to-Electron Conversion Efficiency. *Nano Letters* **2010**, 10, (4), 1259-1265.

116. Ito, S.; Murakami, T. N.; Comte, P.; Liska, P.; Gratzel, C.; Nazeeruddin, M. K.; Gratzel, M., Fabrication of Thin Film Dye Sensitized Solar Cells with Solar to Electric Power Conversion Efficiency over 10%. *Thin Solid Films* **2008**, 516, (14), 4613-4619.

117. Kavan, L.; Gratzel, M., Highly Efficient Semiconducting TiO_2 Photoelectrodes Prepared by Aerosol Pyrolysis. *Electrochimica Acta* **1995**, 40, (5), 643-652.

118. Kang, M. G.; Park, N. G.; Park, Y. J.; Ryu, K. S.; Chang, S. H., Manufacturing Method for Transparent Electric Windows Using Dye-Sensitized TiO_2 Solar Cells. *Solar Energy Materials and Solar Cells* **2003**, 75, (3-4), 475-479.

119. Zhao, Y. X.; Swierk, J. R.; Megiatto, J. D.; Sherman, B.; Youngblood, W. J.; Qin, D. D.; Lentz, D. M.; Moore, A. L.; Moore, T. A.; Gust, D.; Mallouk, T. E., Improving the Efficiency of Water Splitting in Dye-Sensitized Solar Cells by Using a Biomimetic Electron Transfer Mediator. *Proceedings of the National Academy of Sciences of the United States of America* **2012**, 109, (39), 15612-15616.

120. Zhao, Y. X.; Hernandez-Pagan, E. A.; Vargas-Barbosa, N. M.; Dysart, J. L.; Mallouk, T. E., A High Yield Synthesis of Ligand-Free Iridium Oxide Nanoparticles with High Electrocatalytic Activity. *Journal of Physical Chemistry Letters* **2011**, 2, (5), 402-406.

121. Gambardella, A. A.; Bjorge, N. S.; Alspaugh, V. K.; Murray, R. W., Voltammetry of Diffusing 2 nm Iridium Oxide Nanoparticles. *Journal of Physical Chemistry C* **2011**, 115, (44), 21659-21665.

122. Bergkamp, J. J.; Sherman, B. D.; Marino-Ochoa, E.; Palacios, R. E.; Cosa, G.; Moore, T. A.; Gust, D.; Moore, A. L., Synthesis and Characterization of Silicon Phthalocyanines Bearing Axial Phenoxyl Groups for Attachment to Semiconducting Metal Oxides. *Journal of Porphyrins and Phthalocyanines* **2011**, 15, (9-10), 943-950.

123. Kalyanasundaram, K.; Gratzel, M., Applications of Functionalized Transition Metal Complexes in Photonic and Optoelectronic Devices. *Coordination Chemistry Reviews* **1998**, 177, 347-414.

124. Gao, Y.; Ding, X.; Liu, J. H.; Wang, L.; Lu, Z. K.; Li, L.; Sun, L. C., Visible Light Driven Water Splitting in a Molecular Device with Unprecedentedly High Photocurrent Density. *Journal of the American Chemical Society* **2013**, 135, (11), 4219-4222.

125. Moore, G. F.; Blakemore, J. D.; Milot, R. L.; Hull, J. F.; Song, H. E.; Cai, L.; Schmuttenmaer, C. A.; Crabtree, R. H.; Brudvig, G. W., A Visible Light Water-Splitting Cell with a Photoanode Formed by Codeposition of a High-potential Porphyrin and an Iridium Water-Oxidation Catalyst. *Energy & Environmental Science* **2011**, 4, (7), 2389-2392.

APPENDIX I

DETAILS OF COPYRIGHT PERMISSION FOR REPRODUCTION

Chapter 1 has been reproduced with kind permission from Springer Science and Business Media from Sherman, B.D., Vaughn, M.D., Bergkamp, J.J., Gust, D., Moore, A.L., and Moore, T.A. Evolution of reaction center mimics to systems capable of generating solar fuel. *Photosynthesis Research*, **2013**, doi: 10.1007/s11120-013-9795-4.

Copyright Clearance Center License Number: 3156800632969

License Date: May 26, 2013

Chapter 2 has been reproduced with permission of Canadian Science Publishing or its licensors from Sherman, B.D., Pillai, S., Kodis, G., Bergkamp, J., Mallouk, T.E., Gust, D., Moore, T.A., Moore, A.L. A porphyrin–stabilized iridium oxide water oxidation catalyst. *Canadian Journal of Chemistry*, **2011**, 89: 152. © 2008 Canadian Science Publishing or it licensors. Reproduction with permission.

Copyright Clearance Center License Number: 3157350202602

License Date: May 27, 2013

Chapter 3 has been reproduced with permission from Wee, T-L., Sherman, B.D., Gust, D., Moore, A.L., Moore, T.A., Liu, Y., Scaiano, J.C. Photochemical synthesis of a water oxidation catalyst based on cobalt nanostructures. *Journal of the American Chemical Society*, **2011**, 133: 16742. © 2011 American Chemical Society.

Chapter 4 has been reproduced from Bergkamp, J.J., Sherman, B.D., Marino-Ochoa, E., Palacios, R.E., Cosa, G., Moore, T.A., Gust, D., Moore, A.L. Synthesis and characterization of silicon phthalocyanines bearing axial phenoxyl groups for attachment to semiconducting metal oxides. *Journal of Porphyrins and Phthalocyanines*, **2011**, 15: 943. © 2011 World Scientific Publishing Company.